UNIVERSITÀ DELLA CALABRIA

Università della Calabria

Dottorato di ricerca in scienze e tecnologie fisiche, chimiche e dei materiali

XXXVI CICLO

Tesi di Dottorato

Advanced Finite Element and Isogeometric modeling for homogeneous and composite shells involving plasticity, large deformations, and warping

S.S.D. Scienza delle Costruzioni ICAR/08

Supervisore
Prof. Giovanni Garcea

GIOVANNI GARCEA
25.03.2024 09:05:07
GMT+01:00

Coordinatore
Prof.ssa Gabriella Cipparrone

Cipparrone
Gabriella
25.03.2024
13:01:44
GMT+01:00

Dottoranda
Ing. Antonella Corrado

Firma oscurata in base alle linee guida del Garante della privacy

---

Novembre 2023

"Ma quante braccia ti hanno stretto, tu lo sai,
per diventar quel che sei"
Battisti, Mogol

To my Mother and the women of my life.

Acknowledgments

I would like to express my sincere gratitude to my supervisor, Prof. Giovanni Garcea for giving me the opportunity to work in his research group and for his useful guidance during my Ph.D Programme.

A special recognition is due to Dr. Domenico Magisano for his invaluable help.

Also, I would like to thank all the components of the research group: Prof. Antonio Madeo, Prof. Antonio Bilotta, Prof. Leonardo Leonetti, and Dr. Francesco Salvatore Liguori, for their collaboration and precious advice.

Special thanks are due to Prof. Josef Kiendl, for welcoming me at Bundeswehr University, in Munich. It has been a treasured occasion for growth, both for the interesting collaboration pursued and the opportunity to interact with his research group.

Abstract

The aim of this work is to fill in some *gaps* in the non-linear Finite Element (FE) analysis of shell structures, both on the modeling and the numerical computation sides. Apart from the classic FE approach, also the Isogeometric analysis is brought into play, exploiting its high continuity properties.

After introducing the numerical methods for the solution of the structural problem in Chapter one, attention is focused on the main topic. Shell FEs are usually adopted for modeling slender structures that are naturally prone to large displacement/rotation and buckling phenomena, owing to the ratios between their geometrical dimensions. Nevertheless, the versatility of these FEs makes it possible to use them for modeling other kinds of structures where material non-linearity takes on equal if not even greater importance. It is the case of reinforced concrete structures, that guide the discussion in the second Chapter of this thesis. The use of a mixed four-noded FE, known as MISS-4, is extended to a plasticity-based material behavior, with an elastic perfectly plastic model based on the confinement-sensitive plasticity yield surface for modeling the concrete behavior and a uni axial elastic perfectly plastic behavior for the reinforcement bars.

Geometric non-linearity is addressed in Chapter three, where the models for laminated composites are the heart of the discussion, with particular focus on those made of alternating stiff/soft stacking sequences. The peculiar behavior of this kind of structures during the deformation process is represented by warping. The cross section is no longer planar and assumes a piece-wise linear final configuration (*zig-zag* shape). Starting from the phenomenological observation that the shear strains tend to concentrate in the soft layers, while the stiff ones assume a classic Kirchhoff-Love-like behavior, a Total Lagrangian hierarchical approach is proposed to enrich the Isogeometric Kirchhoff-Love shell model with warping functions arbitrary chosen by the user.

The final discussion, in Chapter four, concerns the numerical solution of the non-linear equilibrium equation in case of both material and geometric non-linearities. When modeling geometrically non-linear problems with displacement-based FEs, the iterative cost grows considerably with axial-membrane/flexural stiffness ratio. What makes the difference in the iterative process is the nature of the iteration itself, more than the interpolation/approximation choices in the formulation of the FE. New mixed iteration schemes (i.e. where stress and/or strains are assumed as primary variables along with displacements at local level) are proposed for both displacement-based and mixed FE, identifying for each case the best approach when elasto-plasticity is coupled to geometric non-linearity.

Sommario

Questo lavoro di tesi si pone l'obiettivo di affrontare alcuni aspetti dell'analisi non-lineare di strutture di tipo shell riguardanti sia la modellazione che gli algoritmi di risoluzione numerica step-by-step per la ricostruzione della curva di equilibrio. Accanto al classico approccio agli Elementi finiti (EF), anche il metodo dell'analisi Isogeometrica sarà impiegato.
Dopo aver richiamato nel Capitolo uno i metodi numerici per la ricostruzione della curva di equilibrio di un sistema strutturale, ci si concentrerà sulla modellazione degli EF di tipo shell. L'ambito principale di applicazione riguarda le strutture snelle che, per le loro caratteristiche geometriche, sono soggette a grandi spostamenti e suscettibili di fenomeni di instabilità. Ma accanto a queste, anche altre applicazioni possono avvalersi di EF di tipo shell, ambiti in cui i fenomeni di non-linearità meccanica sono altrettanto importanti, se non predominanti. Un valido esempio è rappresentato dalle strutture in Calcestruzzo Armato (CA) che, per la natura del materiale, sperimentano l'escursione in campo plastico nella loro vita utile. Partendo da questa riflessione, il secondo Capitolo propone l'estensione di un elemento finito misto di tipo shell, denominato MISS-4, all'analisi plastica. Si tratta di un elemento quadrangolare a quattro nodi, in cui l'interpolazione delle tensioni è scelta in modo da soddisfare *a priori* le condizioni di equilibrio per carichi distribuiti nulli. Per quanto concerne la modellazione delle caratteristiche meccaniche dei materiali, per il CA viene adottato un modello con superficie di snervamento dipendente dal livello di confinamento mentre per le barre di armatura ci si è avvalsi di un modello uni-assiale di plasticità perfetta.
Il problema della non-linearità geometrica viene affrontato nel terzo Capitolo, ponendo l'accento sulla modellazione dei compositi laminati ed in particolare quelli in cui si riscontra l'alternanza fra strati con marcata differenza di rigidezza (*duri/soffici*). Tale tipologia di compositi, infatti, presenta una peculiarità nel suo comportamento deformativo, che chiameremo *warping*, ovvero la perdita di planarità della sezione trasversale in seguito alla deformazione. Il profilo trasversale della sezione si atteggia secondo una spezzata, la cosiddetta forma *zig-zag*. Allo scopo di riuscire a cogliere questo particolare meccanismo deformativo, si è proposto un modello gerarchico basato sull'elemento finito isogeometrico di piastra alla Kirchhoff-Love, arricchito da funzioni di warping la cui scelta è ad arbitrio dell'operatore.
Il Capitolo quattro, infine, è dedicato al tema generale della risoluzione numerica delle equazioni non-lineari di equilibrio attraverso i metodi *path-following*, considerando la contemporanea presenza di non-linearità geometriche e meccaniche. Nell'ambio di problemi geometricamente non lineari, l'adozione di EF nelle sole variabili spostamento determina un aggravio dei costi computazionali al crescere del rapporto tra la rigidezza assiale/membranale e quella flessionale degli elementi considerati. Il fattore determinante nell'ottenimento di un metodo risolutivo efficiente non risiede tanto nella tipologia di elemento finito (cioè nella natura dell'interpolazione dei campi incogniti), quanto nel formato dell'iterazione. Uno schema con iterazione mista, dove cioè accanto agli spostamenti altre variabili appaiono come incognite primarie (a livello locale), consente di superare questa *impasse*. L'analisi verrà estesa ad elementi finiti di tipo misto, oltre che a quelli in spostamento, valutandone le performance in caso di contemporaneità fra grandi spostamenti/rotazioni ed elsto-plsticità. Nuovi schemi di iterazione mista sono proposti e testati, individuando quello più performante nelle diverse circostanze.

Contents

Introduction

Since Finite Element (FE) method first appeared, in the forties and fifties of the last century [49, 22], the scientific and technical communities have never lost interest in it. Rather, they are still pushing for further improvement and posing new modeling challenges, encouraged by the contemporary exponential development of the available computational capabilities. The formulation of a high-performing analysis procedure requires to combine two (apparently) antithetical features: the accuracy of the structural behavior and the efficiency of the computations. In order to succeed in this ambitious purpose, two aspects have to be taken into account: i) the structural model has to fit the physical problem to be analyzed with the least possible number of unknowns; ii) the numerical methods adopted to solve the equilibrium problem have to prove efficiency also in case of non-linearities. Willing to introduce a loose categorization, we can generally distinguish between linear and non-linear models, and draw a further distinction between material and geometric non-linearities. About efficiency, basically two aspects must be highlighted: i) the total number of discrete degrees of freedom; ii) the iterative burden needed to obtain the equilibrium points of the system, which is strongly influenced by the non-linear effects. It is evident, at this point, that accuracy and efficiency work in a sort of antagonistic movement. For instance, the rough application of a 3D model shows to be extremely accurate practically in any circumstance. But the total number of unknowns grows considerably with the size of the problem until a point where the procedure becomes *de facto* unusable. To overcome this issue, two possible strategies are available: on the one end, it would be desirable to formulate a nimbler structural model, so that to reduce the number of unknowns to the minimum necessary; alternatively it is possible to operate on the numerical solution strategies in order to make the computation swifter. Of course, the ideal approach is to take action on both sides at the same time.

Shell FE models have proven to be a valid competitor to the three-dimensional simulation in many fields, and their popularity has grown also thanks to fact that the primary structural elements in a wide variety of applications are actually constituted by plates or shells, i.e. thin components with the in-plane dimensions prevailing over the third one. Despite the shallow thickness of the load-bearing elements, these structural components are capable of withstanding quite high external actions and to deform their shape considerably without losing their integrity. In order to bring these precious capacities from theory to practice, efficient computational methods are crucial to make the final structural behavior safe and optimized. Inspired by these considerations, this thesis sets itself the goal of facing some challenging aspects of shell FE modeling. Following the strategy introduced before, the double purpose of improving the structural model and increasing the computational efficiency will be taken into account.

After an introduction concerning the numerical methods for the solution of the structural problem in Chapter one, the discussion about material non-linearity is addressed in Chapter two. As stated before, slender shell structures are characterized by large displacements/rotation and they generally behave within the elastic rage, for what concerns material properties. But there are also other applications where the plastic excursion must be considered. In the context of reinforced concrete structures, for instance, we can find many practical examples of shell-like elements: plates, walls, pre-stressed membrane elements. Therefore, it would be useful to have a dedicated shell FE including the non-linear integration procedure of the constitutive relation. The problem is addressed exploiting a mixed approach and a dual decomposition procedure for the integration of the non-linear constitutive relation.

In Chapter three, the modeling of laminated composite shells is addressed. In this case, attention is focused on the geometric non-linearity, as typical issue affecting this kind of structures. The phenomenological behavior of layered composites is characterized by the loss of planarity of the cross section during the deformation. In general, the cross section assumes a *zig-zag* shape, which is a piece-wise linear configuration. In the particular case of laminated composites made of alternating stiff/soft layups, the shear strains tend to concentrate in the soft layers while the stiff ones are all subjected to almost identical rotations with respect to their normal in the initial configuration. Different approaches are available to model laminated composites, but warping still represents a challenging aspect. The classical First Order Shear Deformation Theory (FSDT) fails in reproducing the correct solution, while a layer-wise approach becomes computationally expansive when the number of layers grows. The so-called Zig-zag theories are based on the superposition of a linear zig-zag contribution to the in-plane displacements given by a first (or higher) order shear deformation theory model. But they have the limitation that a single zig-zag shape is considered, and it could not be the best approximation of the real behavior (as in the case of unsymmetrical stacking sequences where disparities between the soft layers occur in geometry or mechanical properties). This modeling problem is faced proposing a hierarchic enrichment of the large displacements isogeometric Kirchhoff-Love shell with warping functions of arbitrary shape, defined for the two in-plane reference directions. Each warping function carries an additional unknown, representing the amplitude of the warping mode. Two different approaches are tested, with a set of independent warping functions, one for each layer, or with a unique function defined over the whole thickness of the laminate. The accuracy of the model will be discussed for different layups of the stacking sequence and compared to FSDT and 3D approaches.

In Chapter four, the solution strategy for the equilibrium equation in presence of both material and geometrical non-linearity is addressed. The problem of slow convergence for displacement based FE in case of geometric non-linearity was highlighted for the first time in [37], where it was shown that the iterative burden increases with the axial/flexural stiffness ratio in large rotations problems. This is blamed on the fact that the stress used to evaluate the iteration matrix can be affected by a large error when computed from the predicted displacements during the iterations. The use of mixed FEs proves to be a good alternative to eliminate this issue but, interestingly, it's the mixed format of the iteration which prevents the computational burden to increase, not the nature of the FE interpolation/approximation. This was demonstrated in [83], where, for linear elastic materials, the mixed iterative scheme for large deformations problems was extended to DFEs without introducing a FE approximation for the stress. This is the starting point of the discussion in Chapter four, where the geometric non-linearity is coupled to elasto-plasticity. Both displacement based and mixed FEs for beam and shell structures are analyzed and new mixed iterative procedures are proposed, finding the most efficient approach to solve the global equilibrium system for each case. Finally, the main results achieved in this discussion are summarized in the concluding Chapter.

Chapter 1

Incremental-iterative solution of nonlinear structural problems

The FE method is henceforth a well-established procedure for approaching a wide variety of computational modeling problems based on two key aspects: i) the whole system, however complicated, is divided into subdomains of a given shape, called *Finite Elements*; ii) the differential equations underling the problem are approximately solved over each element introducing a suitable interpolation of the unknown fields. The behavior of the whole structure is obtained assembling the contribution of each FE.

The structural problem is generally represented by a set of partial differential equations over a continuous domain identified with the volume of the whole system, in what we call the strong form. The application of the variational principles brings to an alternative formulation in an integral form, also called the weak form, which allows to relieve the continuity requirements on the solution fields [4].

At this point, the approximation relation is introduced for the unknown fields, assuming as parameters the discrete values of the unknowns at the element nodes. Depending on the choice of the unknowns, we distinguish between displacement based FEs, where the kinematic parameters only are assumed as independent variables, and mixed FEs, which provide for further variables (stress and/or strains) along with displacements. Both these approaches will be extensively addressed later on.

In the most part of practical applications, non-linearities of different nature occur. We can generally distinguish between geometric and material non-linearities, affecting the kinematic compatibility and the constitutive relations respectively. When dealing with non-linear problems via numerical methods, efficiency becomes a main issue. Different modeling aspects come into play, involving not only the total number of unknowns but also the format of the approximation and the FE approach. With the purpose to address thoroughly the question later, in this chapter the most popular continuation method used for drawing the equilibrium path of a mechanical system in non-linear structural problems, the *Arc-Length* method, is introduced.

1.1 Numerical solution of the non-linear structural problem

Let us consider a discrete formulation with N degrees of freedom (DOFs) obtained through a FE discretization of the structure. The discrete counterpart of the equilibrium equation under conservative loads is given by:

$$\mathbf{r}[\mathbf{q},\lambda] \equiv \mathbf{s}[\mathbf{q}] - \lambda \mathbf{p} = 0, \tag{1.1}$$

where $\mathbf{r} : \mathbb{R}^{N+1} \to \mathbb{R}^N$ is a non-linear vectorial function of the vector $\mathbf{z} \equiv (\mathbf{q},\lambda) \in \mathbb{R}^{N+1}$, collecting the configuration $\mathbf{q} \in \mathbb{R}^N$ and the load multiplier $\lambda \in \mathbb{R}$, $\mathbf{s}[\mathbf{q}]$ is the internal force vector and $\mathbf{p}$ is the reference load vector. The type of variables stored in vector $\mathbf{q}$ depends on the nature of the FE formulation: displacement parameters in the case of displacement-based FE formulations; displacements and stress/strain variables for the mixed formulations. For the sake of simplicity and with the intent of introducing the incremental-iterative solution schemes in general, the symbol $\mathbf{q}$ will be here assumed as representative of the independent variables of the considered problem. In the following, the variables will be explicitly designated for each formulation by turn.

Equation 1.1 represents a N-equation system in $N+1$ unknowns whose solutions draw the equilibrium paths as curves in $\mathbb{R}^{N+1}$, starting from a known initial configuration $\mathbf{q}_0$, corresponding to $\lambda = 0$. The tangent stiffness matrix is defined as:

$$\mathbf{K}[\mathbf{q}] = \frac{\partial \mathbf{s}}{\partial \mathbf{q}} \tag{1.2}$$

1.1.1 Path-following strategy: the Arch-Lenght method

In path-following methods, the equilibrium path of the structure can be drawn step-by-step by numerically solving the system of the equilibrium equation. Starting from a known equilibrium state, the next point of the curve is determined by an iterative process. The simplest scheme is the so called load-controlled method. For a defined increment assigned to the load multiplier, the set of variables that satisfy the equilibrium within a certain tolerance is determined. Despite being appreciable for its simplicity, this method suffers from lack of robustness, In fact, when a limit point occurs in the equilibrium path, the convergence is lost. The arc-Length strategy proposed by Riks [115] allows to overcome this issue. It consists in a generalization of the Newton's method in which the load multiplier is not pre-determined within each step and the equilibrium equations are completed with an additional condition.

The Arc-Lenght method

As introduced before, the equilibrium system 1.1 is completed adding a constraint of the shape $g[\mathbf{q}, \lambda] - \xi = 0$, which defines a surface in $\mathbb{R}^{N+1}$. The sequence of the points (steps) $\mathbf{z} \equiv (\mathbf{q}_{(k)}, \lambda_{(k)})$ belonging to the equilibrium path are obtained solving the non-linear system

$$\mathbf{R}[\xi] \equiv \begin{bmatrix} \mathbf{r}[\mathbf{q}, \lambda] \\ g[\mathbf{q}, \lambda] - \xi \end{bmatrix} = \mathbf{0} \tag{1.3}$$

for successive values assigned to the control parameter $\xi = \xi_{(k)}$ at each step. The non-linear system 1.3 is solved by means of the Newton iterative method. Starting from a known equilibrium point $\mathbf{z}^0 \equiv \mathbf{z}_{(k)}$, the new one $\mathbf{z}_{(k+1)}$ is evaluated correcting a first extrapolation $\mathbf{z}^1 = \{\mathbf{q}^1, \lambda^1\}$ by a sequence of estimates $\mathbf{z}^j$ (loops):

$$\begin{cases} \bar{\mathbf{J}}\dot{\mathbf{z}} = -\mathbf{R}^j \\ \mathbf{z}^{j+1} = \mathbf{z}^j + \dot{\mathbf{z}} \end{cases} \tag{1.4a}$$

where $\mathbf{R}^j \equiv \mathbf{R}[\mathbf{z}^j]$ and $\bar{\mathbf{J}}$ is the Jacobian of the non-linear system (1.3) at $\mathbf{z}^j$ or a suitable estimate. The simplest choice for $g[\mathbf{q}, \lambda]$ is the linear constraint corresponding to the orthogonal hyperplane

$$\mathbf{n}_q^T(\mathbf{q} - \mathbf{q}^j) + n_\lambda\,(\lambda - \lambda^j) = \Delta\xi \quad \text{where} \quad \begin{cases} \mathbf{n}_q \equiv \mathbf{M}\,(\mathbf{q}^j - \mathbf{q}_{(k)}) \\ \mathbf{n}_\lambda \equiv \mu\,(\lambda^j - \lambda_{(k)}) \end{cases} \tag{1.4b}$$

where j denotes the estimate at the current Newton's iteration, $\mathbf{M}$ and μ being some suitable metric factors [37, 36], $\Delta\xi$ an assigned increment of ξ, that is the step-size, and

$$\bar{\mathbf{J}} \approx \left[\frac{\partial \mathbf{R}[\mathbf{z}]}{\partial \mathbf{z}}\right]_{\mathbf{z}^j} = \begin{bmatrix} \bar{\mathbf{K}} & -\mathbf{p} \\ \mathbf{n}_q^T & n_\lambda \end{bmatrix}. \tag{1.4c}$$

The load-controlled scheme can be seen as a particular case of the arch-length method obtained assuming as the constrain $g[\mathbf{q}, \lambda] = \lambda$ (see [37] for further details). Instead, keeping

$\bar{\mathbf{K}} = \mathbf{K}[\mathbf{q}^1]$ we obtain the modified Newton scheme. The solution of Eq.(1.4) is conveniently performed as follows

$$\begin{cases} \dot{\lambda} = \dfrac{\mathbf{n}_q^T \bar{\mathbf{K}} \mathbf{r}^j}{n_\lambda + \mathbf{n}_q^T \bar{\mathbf{K}} \mathbf{p}} \\ \bar{\mathbf{K}} \dot{\mathbf{q}} = \dot{\lambda} \mathbf{f} - \mathbf{r}^j. \end{cases} \tag{1.5}$$

Convergence of the arc-length scheme.

The convergence of the iterative process (1.4) can be expressed by the condition [37]:

$$\mathbf{R}_{j+1} = \left(\mathbf{I} - \mathbf{J}_s \bar{\mathbf{J}}^{-1} \right) \mathbf{R}_j \tag{1.6}$$

where $\mathbf{I}$ is the identity matrix, $\tilde{\mathbf{J}}$ is the iteration matrix and

$$\mathbf{J}_s \equiv \int_0^1 \mathbf{J}[\mathbf{z}_j + t(\mathbf{z}_{j+1} - \mathbf{z}_j)] \, dt$$

the secant Jacobian matrix. The iteration converges is:

$$\left\| \mathbf{I} - \mathbf{J}_s \bar{\mathbf{J}}^{-1} \right\| < 1$$

where $\| \cdot \|$ indicates a suitable norm definition. The closer to $\bar{\mathbf{J}}$ is $\mathbf{J}_s$, the faster will be the convergence. For the sake of completeness, note that the convergence condition for a load controlled scheme is obtained by replacing $\bar{\mathbf{J}}$ and $\mathbf{J}_s$ with $\bar{\mathbf{K}}$ and $\mathbf{K}_s$ respectively. For the displacement format in the case of positive definite $\bar{\mathbf{K}}$ the convergence condition can be simplified as:

$$0 < \mathbf{q}^T \mathbf{K}_s \mathbf{q} < 2\mathbf{q}^T \bar{\mathbf{K}} \mathbf{q}, \quad \forall \mathbf{q}. \tag{1.7}$$

A convergence condition similar to Eq.(1.7), but limited to the subspace of non-singular values of $\bar{\mathbf{K}}$, holds also for the arc-lenght scheme [37] that, like for the load controlled case, is as faster as:

$$\mathbf{q}^T \mathbf{K}_s \mathbf{q} \approx \mathbf{q}^T \bar{\mathbf{K}} \mathbf{q}, \quad \forall \mathbf{q} \tag{1.8}$$

and it converges in a single iteration when $\mathbf{K}_s = \bar{\mathbf{K}}$ because of the linearity of Eq.(1.4b).

Since $\bar{\mathbf{J}}$ is not singular even when $\bar{\mathbf{K}}$ is singular, the arc-length scheme provides a simple way to overcome limit points. However, the choice of the variables in the problem description plays a crucial role in the overall quality and speed of convergence, in terms of step size and total number of iterations. In general, when dealing with geometric non-linearities in slender structures where the membrane/axial stiffness prevails over the flexural one , displacement based models show poor convergence quality, due to a locking-like phenomenon [37]. Since the stresses used to evaluate the tangent matrix are forced to satisfy the constitutive equations at each iteration, their estimate can be quite far from the real value, due to a bad estimate of the displacement within the iteration. The application of a mixed approach overcomes this issue, because the stresses are directly extrapolated and corrected in the iterative process, allowing faster convergence of the Newton method and very large steps, regardless of the slenderness of the structure. This issue will be widely addressed in the following, extending the discussion to the case of coupled geometric and material non-linearities.

Remarks on the computational cost

Two main aspects affect the computational burden of the path-following iterative procedure: the number of DOFs and the total amount of iterations. We can distinguish between the Full Newton and the Modified Newton schemes: the former one requires the iteration matrix to be updated at each step, which in general brings to a higher operational cost. When the number of DOFs increases, the cost of an entire step of the modified version tends to the cost of a single iteration of the full method. Regarding the number of iterations, the computational cost of the iterative method is directly proportional to the number of iterations for the full versions and almost directly proportional to the number of steps for the modified version.

1.1.2 Implementation details

The details concerning the parameters introduced in 1.1.1 adopted in the following for the implementation of the arch-length method are here reported:

- Predictor
  Starting from a known equilibrium point $\mathbf{z}_{(k)} = \big(\mathbf{q}_{(k)}, \lambda_{(k)}\big)$, with $\mathbf{q}$ collecting the independent problem variables (e.g. displacements only or displacements together with stress/strain variables), the first predictor $\mathbf{z}^1$ of the new equilibrium point $\mathbf{z}_{(k+1)}$ is evaluated as
  $$\mathbf{z}^1 = \mathbf{z}_{(k)} + \alpha(\mathbf{z}_{(k)} - \mathbf{z}_{(k-1)}),$$
  where α defines the step size. For the first equilibrium point, it is particularized as
  $$\mathbf{z}_1 = \Delta\lambda_0 \begin{bmatrix} 1 \\ \hat{\mathbf{q}} \end{bmatrix}$$
  being $\hat{\mathbf{q}}$ the linear elastic solution for the reference load $\hat{\mathbf{p}}$.

- Arc-length parameters
  The arc-length constraint in Eq. (1.4b) is defined by the metric factors $\mathbf{M}$ and μ. The metric matrix $\mathbf{M}$ is assumed to be a diagonal matrix with $M_{ii} = 1$ if the ith variable is a displacement, $M_{ii} = \ell^2$ if the ith variable is a rotation, ℓ being a characteristic length of the structures. The factor μ is selected as
  $$\mu = 10^{-3}\hat{\mathbf{q}}^T\mathbf{M}\hat{\mathbf{q}}.$$

- Adaptive step size
  The factor α which defines the step size is evaluated in an adaptive way in terms of the iterations required in the last step N_k and the desired number of iterations per step N_d, chosen as equal to 4, as
  $$\alpha = 1 - \frac{0.7(N_k - N_d)}{N_k + N_d}.$$
  The values of α are constrained by the condition $\alpha \in [0.5, 1.5]$.

- Convergence criteria
  Convergence is accepted if
  $$(\dot{\mathbf{q}}^j)^T\mathbf{M}\dot{\mathbf{q}}^j < \mathrm{Toll}^2(\Delta\lambda_0^2\hat{\mathbf{q}}^T\mathbf{M}\hat{\mathbf{q}}),$$
  that is if the norm of the correction to the displacement solution is smaller than a desired tolerance Toll $= 10^{-4}$ compared to the initial solution increment. If the convergence condition is not satisfied after 15 iterations or if the error fails to decrease after two consecutive iterations, the iterations are abandoned and α is halved.

Chapter 2

A layer-wise plasticity-based approach for mixed shell finite elements with application to reinforced concrete structures

As a first stage for the discussion, material non-linearity in the context of a layer-wise shell model will be addressed in the following chapter. The general description of the model will be placed in the framework of reinforced concrete structures. Reinforced concrete, universally recognized as the most popular material in civil engineering applications, is characterized by a strongly non-linear behavior since the lowest load levels. This is a practical context where material non-linearity must be taken into account, but the generality of the approach makes it applicable also in analogous circumstances. The structural response is numerically evaluated using a mixed four-noded quadrilateral shell finite element based on self-equilibrated assumed stresses. The kinematic fields are interpolated only along the element boundary by polynomials up to the third order. The generalized shell stresses are evaluated through layer-wise integration of the Cauchy point wise stresses. This allows appropriated three-dimensional elasto-plastic constitutive equation to be employed and to include multiple reinforcing layers. The integration of the constitutive laws is performed using a dual decomposition method which preserves the assumed stress interpolation. The aim of this discussion is the development of an accurate and efficient approach for the non-linear static analysis, compared to the available commercial tools. The achievement of this goal is demonstrated by reporting benchmark examples including civil engineering applications.

2.1 Introduction

Contrary to what one might think judging by its massive appearance, reinforced concrete (RC) is quite a versatile material. For instance, long span roofs constituted by RC shells with complex geometries and optimized shapes are widespread [95]. Apart from the shape, the mechanical properties of RC elements, if properly tuned, may represent a crucial resource in challenging load scenarios. Indeed in seismic hazard zones, RC is often employed to design structures with high ductility properties following the capacity design rules [94]. It is worth noting, however, that a considerable part of the building heritage in Europe is constituted by RC structures for which it's necessary to take into account a program of monitoring and retrofitting interventions. The analysis procedures available to support the widespread range of applications for RC structures are characterized by a high degree of complexity arising from the non-linear material and structural behavior [57, 7]. The challenge to guarantee reliable results and computational efficiency is not trivial and it's worth

of attention.
Inspired by the previous consideration, this work aims at developing efficient numerical tools for the layer-wise analysis of shell structures accounting for material non-linearity. Moreover it represents a perfect starting point for dealing with the non-linear analysis of shells structures, in the spirit of the *road map* traced in the general introduction to this thesis. To begin with, the main focus is given to material non-linearity, implementing the analysis in the framework of an existing high-performance mixed finite element and referring to a layer-wise modeling approach.
The FE method is successfully employed in modeling general shaped structures [6, 50, 60] among which the RC structures are certainly included. This approach has the double benefit of precisely describing the geometry and allowing an accurate description of the mechanical behavior by adopting constitutive laws expressed in terms of 3D stresses [129]. An interesting example is the model of slab-column connections in flat concrete slabs [39] using a 8-noded hexahedral FE with a concrete damaged plasticity material behavior. Interestingly, solid FEs are also applied to numerically test the effect of innovative technologies in this field, as those employed for retrofitting purposes. For example, the effectiveness in using Fiber Reinforced Polymer (FRP) wraps to confine RC columns is proven in [111] where solid FE and a plasticity-based approach are used. However, the accuracy of a 3D model is counterbalanced by the considerable computational burden, which may become prohibitive in case of large, complex structures. With the aim of reducing the cost of the simulations and allowing full-scale structures to be analyzed efficiently, different types of approaches have been proposed, based on beams, membrane, plate, shell and solid-shell FEs [6, 50, 60]. Restricting the field of observation to the 2D plate and shell models, many interesting modeling strategies for RC structures are available, characterized by various FE formulations and material descriptions. Many works focus on the membrane response which is relevant in the analysis of in-plane loaded structures, as in shear walls. A non-linear quadrilateral layered membrane FE with drilling rotations and smeared cracked orthotropic concrete is proposed by Rojas et al. [117]. In [105] the proposed model is an Isoparametric FE coupled with layered sections and a plane-stress plastic-damage concrete material for the simulation of the in-plane non-linear hysteretic behavior of RC shear walls. In parallel, the out-of-plane behaviour is also considered in many works that aim at describing the behavior of slabs or shells. In particular, a plasticity based approach is used to formulate a layer-based FE limit analysis of slabs [55] implemented using conic programming with a reformulation of the modified Coulomb yield criteria for a 3D stress state. The approach proposed in [28] is suitable for the analysis of plates with generic geometries being based on Kirchhoff triangular plate element implementing a laminated shell element able to reproduce the damage due to bending stresses. Among the many FEs available in literature, mixed formulations offer a valid and robust approach [123, 108]. Compared to the more widespread displacement-based FEs, in mixed formulations stresses or strains are also assumed as independent variables allowing the elimination of many kinds of locking effects [23, 17, 119, 62], the achievement of high levels of accuracy, i.e. low error on coarse mesh grids and elevated rate of convergence for all the unknown fields [20, 18]. These properties, that allow a great amount of computational time to be saved, are observed in linear [19, 77] but also in non-linear applications [10, 131, 136, 91]. Despite the good performance shown in various contexts, mixed FEs are not commonly adopted in the analysis of shell structures where, as in the case of RC applications, the material non-linearity takes part. Examples of non-linear mixed FE are limited to beams [88, 11], where they have shown advantages in terms of efficiency and accuracy in evaluating the non-linear response of frame structures also in conditions of fire [87], where the non-linear mechanical behavior is further exacerbate by the decay of the material properties due to high temperatures.
In this chapter, an efficient mixed plasticity-based FE for the layer-wise analysis of shell structures is presented and tested. It is based on a novel use of a previously proposed mixed FE [78], named MISS-4 (Mixed Isostatic Self Equilibrated Stresses).It is a four noded Mindlin-Reissner FE with 24 degrees of freedom (DOFs) for describing the displacement field. The mixed formulation is based on assumed stresses that a-priori satisfy equilibrium equations for zero bulk loads. This aspect is of great importance since it allows the accu-

racy of the FE to be enhanced without increasing the computational cost. Additionally, the number of stress parameters is 18 which represents the minimum required for the element stability. This choice has been shown to be optimal in terms of the advantages provided by the mixed approach [10, 78, 76]. The element has been previously tested in elasticity problems [78], showing good performance, characterized by accurate solutions for coarse meshes, low sensitivity to mesh distortion, quadratic rate of converge for both displacement and stress fields. These features are preserved in large-deformation problems [5] even for constant and variable-stiffness composite materials [143]. Despite the fact of using generalized stress and strain fields, a solid-like behavior is recovered by adopting a layer-wise approach [117, 55]. It is based on a decomposition of the generalized stresses at the level of the material point. The layer-wise approach allows material models expressed in terms of Cauchy stresses to be used and, additionally, to include multiple layers of reinforcement. The non-linear material response is obtained using a plasticity based approach for both concrete and reinforcement. The plastic admissibility is controlled in a discrete number of Integration Points (IPs) located over the shell mid-surface. Additionally, on the basis of the layer-wise description, further IPs are also considered along the thickness direction. Assuming RC as reference material, the use of plasticity-based models to describe its non-linear behavior is widespread and provides good results within a robust and theoretically established framework [130, 75, 121, 55]. When mixed formulations are used in plasticity problems, the return mapping scheme must impose the constitutive law at the element level in order to preserve the assumed stress interpolation [89, 90, 126, 100]. Otherwise, while plasticity evolves, the accuracy deteriorates thereby loosing all the advantages that mixed formulations provide. In this work, the problem is solved by adopting a dual decomposition technique [128, 132, 97, 98]. The return mapping scheme is divided into two sub problems [80]. The first one is a series of return mapping formulated at the level of the IPs which coincide with the problem solved in usual displacement-based formulations. The second one is an element state determination described by a system of non-linear equations that recovers the assumed stress interpolation and can be solved with a Newton method [80]. Interestingly, the proposed approach can be readily implemented in existing FE codes and does not require the use of any *ad hoc* algorithm. Additionally, it has no limitation about the material response and can be adopted for analyzing problems with damage and non-associate plasticity. The coupling between the mixed FE and the layer-wise approach solved with a dual decomposition technique constitutes another novelty of the work. The non-linear response of concrete is modeled through an elastic perfectly plastic model based on the confinement-sensitive plasticity yield surface proposed by Papanikolaou and Kappos [103] for accurately describing the compressive non-linear response of concrete. The yield surface, depending on all the stress invariants, is capable of describing the dependence of the deviatoric sections, changing from triangular to almost circular shape, from the confinement level. Moreover, all the required parameters are expressed in terms of only the uni axial compressive concrete strength, leading to a single-parameter model which turns out very easy to use. Steel reinforcements layers contribute through a Von Mises elastic perfectly plastic response. The proposed mixed FE approach is tested in incremental elasto-plastic analyses. This kind of analysis is widely used in structural engineering applications such as in static non-linear analyses for assessing the seismic capacity of civil constructions [29]. A series of numerical results are presented and discussed for validating and showing the performance of the proposed approach. Some tests also have a clear practical application in the field of civil engineering, regarding a shear wall and a prestressed long span girder for bridges. The chapter is organized as follows. In Section 2.2 the main outline of MISS-4 in linear elasticity are given. The incremental elastoplastic analysis and the layer wise approach for RC shells are presented in Section 2.3. The mechanical response for concrete and steel reinforcement are presented and discussed in Section 2.4. In Section 2.5 the numerical tests are presented. Finally, a summary is given in Section 2.6

2.2 Linear-elastic formulation of MISS-4

The shell model and its discrete formulation based on MISS-4 element are herein briefly introduced. Further insights can be found in [78, 72].

2.2.1 The shell model

The adopted shell model used is obtained from the Cauchy continuum by assuming both stress and displacement fields. In particular, the assumed stress field is ruled by the generalised stress components of the shell, while the assumed displacement field depends on the kinematic description of the mid-surface, see [35] for further details.

Let us consider a local Cartesian frame $(\mathcal{O}, x, y, z)$ with unit vectors $\mathbf{i}_1, \mathbf{i}_2, \mathbf{i}_3$ with $\mathbf{i}_3$ orthogonal to the shell mid-surface. The position of a generic point is evaluated as $\mathbf{X} = \mathbf{x} + z\mathbf{i}_3$, where $\mathbf{x} = x\mathbf{i}_1 + y\mathbf{i}_2$ is the projection over the shell mid-surface. Adopting the Mindlin-Reissner model, the kinematics is defined as

$$\mathbf{u}_G[\mathbf{X}] = \mathbf{u}[\mathbf{x}] + z\boldsymbol{\varphi}[\mathbf{x}] \times \mathbf{i}_3 \tag{2.1}$$

where the mid-surface translations, on the local reference system, are $\mathbf{u}[\mathbf{x}] = \{u[\mathbf{x}], v[\mathbf{x}], w[\mathbf{x}]\}$ while $\boldsymbol{\varphi} = \{\varphi_1[\mathbf{x}], \varphi_2[\mathbf{x}], \varphi_3[\mathbf{x}]\}$ is the rotation vector.

The linear strain measure becomes

$$\boldsymbol{\epsilon} = \frac{1}{2}(\nabla\mathbf{u} + \nabla\mathbf{u}^T) \tag{2.2}$$

where

$$\nabla\mathbf{u} = \begin{bmatrix} u_{,1} + \varphi_{2,1}z & u_{,2} + \varphi_{2,2}z & \varphi_2 \\ v_{,1} - \varphi_{1,1}z & v_{,2} - \varphi_{1,2}z & -\varphi_1 \\ w_{,1} & w_{,2} & 0 \end{bmatrix} \tag{2.3}$$

in which a comma stands for partial derivative and the dependence on $\mathbf{x}$ and z is omitted. Using a Voigt notation and letting $\mathbf{E}[\mathbf{x}, z] = \{E_{11}, E_{22}, 2E_{12}, 2E_{13}, 2E_{23}\}$ the vector which collects the non zero strain components, the assumed kinematics in Eq.(2.1) gives

$$\begin{cases} E_{11} = e_{11} - z\chi_{11} \\ E_{22} = e_{22} - z\chi_{22} \\ 2E_{12} = e_{12} - z\chi_{12} \\ 2E_{13} = \gamma_{13} \\ 2E_{23} = \gamma_{23} \end{cases} \Rightarrow \quad \mathbf{E}[\mathbf{x}, z] = \begin{bmatrix} \mathbf{Y}_m[z] & \mathbf{Y}_\chi[z] & \mathbf{Y}_\gamma[z] \end{bmatrix} \begin{bmatrix} \mathbf{e}[\mathbf{x}] \\ \boldsymbol{\chi}[\mathbf{x}] \\ \boldsymbol{\gamma}[\mathbf{x}] \end{bmatrix} = \mathbf{Y}[z]\boldsymbol{\varepsilon}[\mathbf{x}]. \tag{2.4}$$

The generalised strain vectors $\mathbf{e}$, $\boldsymbol{\chi}$ and $\boldsymbol{\gamma}$ are defined as:

$$\begin{aligned} \mathbf{e}[\mathbf{x}] &= \begin{bmatrix} e_{11} \\ e_{22} \\ 2e_{12} \end{bmatrix} = \begin{bmatrix} u_{,1} \\ v_{,2} \\ u_{,2} + v_{,1} \end{bmatrix} \\ \boldsymbol{\chi}[\mathbf{x}] &= \begin{bmatrix} \chi_{11} \\ \chi_{22} \\ \chi_{12} \end{bmatrix} = \begin{bmatrix} -\varphi_{2,1} \\ \varphi_{1,2} \\ \varphi_{1,1} - \varphi_{2,2} \end{bmatrix} \\ \boldsymbol{\gamma}[\mathbf{x}] &= \begin{bmatrix} \gamma_{13} \\ \gamma_{23} \end{bmatrix} = \begin{bmatrix} w_{,1} + \varphi_2 \\ w_{,2} - \varphi_1 \end{bmatrix}, \end{aligned} \tag{2.5}$$

where the 5×3 matrices $\mathbf{Y}_m$ and $\mathbf{Y}_\chi$ and the 5×2 matrix $\mathbf{Y}_\gamma$ are:

$$\mathbf{Y}_m = \begin{bmatrix} \mathbf{I}_3 \\ \mathbf{0}_{2\times3} \end{bmatrix} \qquad \mathbf{Y}_\chi[z] = \begin{bmatrix} -z\mathbf{I}_3 \\ \mathbf{0}_{2\times3} \end{bmatrix} \qquad \mathbf{Y}_\gamma[z] = \begin{bmatrix} \mathbf{0}_{3\times2} \\ \mathbf{I}_2 \end{bmatrix}, \tag{2.6}$$

being $\mathbf{I}_k$ the identity matrix of dimension k and $\mathbf{0}_{i\times j}$ a zero $i \times j$ matrix.

The vector collecting the components of the Cauchy stress is defined as $\mathbf{S}[\mathbf{x},z] = \{S_{11}, S_{22}, S_{12}, S_{13}, S_{23}\}$, where we have assumed that $S_{33} = 0$. The generalised stresses $\boldsymbol{\sigma}[\mathbf{x}] = \{\boldsymbol{\sigma}_m[\mathbf{x}], \boldsymbol{\sigma}_\chi[\mathbf{x}], \boldsymbol{\sigma}_\gamma[\mathbf{x}]\}$ dual to $\boldsymbol{\varepsilon}[\mathbf{x}]$ are obtained through the virtual work equation as

$$\begin{aligned}\mathbf{W} &= \int_V \mathbf{S}^T[\mathbf{x},z]\mathbf{E}[\mathbf{x},z]dV = \int_B \left(\boldsymbol{\sigma}_m^T[\mathbf{x}]\mathbf{e}[\mathbf{x}] + \boldsymbol{\sigma}_\chi^T[\mathbf{x}]\boldsymbol{\chi}[\mathbf{x}] + \boldsymbol{\sigma}_\gamma^T[\mathbf{x}]\boldsymbol{\gamma}[\mathbf{x}]\right) dA \\ &= \int_B \left(\boldsymbol{\sigma}^T[\mathbf{x}]\boldsymbol{\varepsilon}[\mathbf{x}]\right) dA,\end{aligned} \tag{2.7}$$

where

$$\begin{aligned}\boldsymbol{\sigma}_m[\mathbf{x}] &= \int_{-h/2}^{h/2} \mathbf{Y}_m[z]^T\mathbf{S}[\mathbf{x},z]\,dz \\ \boldsymbol{\sigma}_\chi[\mathbf{x}] &= \int_{-h/2}^{h/2} \mathbf{Y}_\chi[z]^T\mathbf{S}[\mathbf{x},z]\,dz \\ \boldsymbol{\sigma}_\gamma[\mathbf{x}] &= \int_{-h/2}^{h/2} \mathbf{Y}_\gamma[z]^T\mathbf{S}[\mathbf{x},z]\,dz \\ \boldsymbol{\sigma}[\mathbf{x}] &= \int_{-h/2}^{h/2} \mathbf{Y}[z]^T\mathbf{S}[\mathbf{x},z]\,dz.\end{aligned} \tag{2.8}$$

In components, we have that

$$\boldsymbol{\sigma}_m[\mathbf{x}] = \begin{bmatrix} N_{11} \\ N_{22} \\ N_{12} \end{bmatrix} \qquad \boldsymbol{\sigma}_\chi[\mathbf{x}] = \begin{bmatrix} M_{11} \\ M_{22} \\ M_{12} \end{bmatrix} \qquad \boldsymbol{\sigma}_\gamma[\mathbf{x}] = \begin{bmatrix} T_{13} \\ T_{23} \end{bmatrix} \tag{2.9}$$

where N_{ij}, M_{ij} and T_{iz} are the membrane forces, resultant moments and out-of-plane shear forces, respectively, with $i,j = 1,2$. Finally, the elastic constitutive laws $\mathbf{S}[\mathbf{x},z] = \mathbf{C}\mathbf{E}[\mathbf{x},z]$ can be expressed in terms of generalised quantities as

$$\boldsymbol{\sigma}[\mathbf{x}] = \mathbf{D}\boldsymbol{\varepsilon}[\mathbf{x}] \qquad \text{with} \qquad \mathbf{D} \equiv \int_{-h/2}^{h/2} \mathbf{Y}[z]^T\mathbf{C}\mathbf{Y}[z]dz. \tag{2.10}$$

To simplify the notation, the dependence of the quantities on $\mathbf{x}$ will be omitted from now on.

2.2.2 Assumed stresses

For the sake of simplicity, from now on the curvature and shear generalized stress components are collectively denoted as the flexural components, by introducing the vector:

$$\boldsymbol{\sigma}_f = \begin{bmatrix} \boldsymbol{\sigma}_\chi \\ \boldsymbol{\sigma}_\gamma \end{bmatrix} \tag{2.11}$$

The stresses are assumed to be self-equilibrated and isostatic, leading to a minimum set of parameters which are the 18 components of the vector $\boldsymbol{\beta}_e$. In this manner, the stress resultants are interpolated as

$$\boldsymbol{\sigma} = \mathbf{N}_t\boldsymbol{\beta}_e = \begin{bmatrix} \mathbf{N}_{tm} & \mathbf{0} \\ \mathbf{0} & \mathbf{N}_{tf} \end{bmatrix} \begin{bmatrix} \boldsymbol{\beta}_m \\ \boldsymbol{\beta}_f \end{bmatrix}, \tag{2.12a}$$

where $\mathbf{N}_{tm}$ and $\mathbf{N}_{tf}$ are the matrices representing the assumed stress modes for the membrane and flexural generalised stresses, respectively, while $\boldsymbol{\beta}_m$ and $\boldsymbol{\beta}_f$ are 9-component vectors representing membrane and flexural moments, respectively. For the membrane stresses, it is assumed that

$$\mathbf{N}_{tm} = \begin{bmatrix} 1 & 0 & 0 & y & 0 & x & 0 & y^2 & -2\bar{a}\,x\,y \\ 0 & 1 & 0 & 0 & x & 0 & y & -x^2 & 2\,\bar{b}\,x\,y \\ 0 & 0 & 1 & 0 & 0 & -y & -x & 0 & \bar{a}y^2 - \bar{b}\,x^2 \end{bmatrix} \tag{2.12b}$$

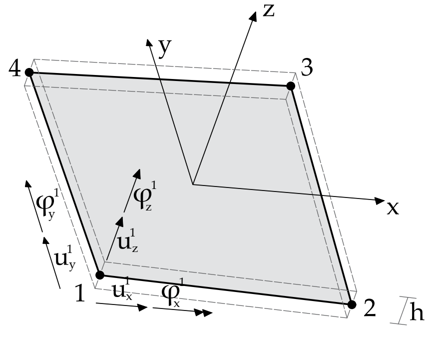

Figure 2.1: Elemental geometry and degrees of freedom for node 1.

with $\bar{a} = a^2/(a^2+b^2)$ and $\bar{b} = b^2/(a^2+b^2)$, being a and b two scalar coefficients taking account of the element distortion (see Ref. [78, 72] for details). For the flexural stresses, it is assumed that

$$\mathbf{N}_{tf} = \begin{bmatrix} 1 & 0 & 0 & x & 0 & y & 0 & x\,y & 0 \\ 0 & 1 & 0 & 0 & x & 0 & y & 0 & x\,y \\ 0 & 0 & 1 & 0 & y\,\bar{c} & x/\bar{c} & 0 & 0 & 0 \\ 0 & 0 & 0 & -1 & -\bar{c} & 0 & 0 & -y & 0 \\ 0 & 0 & 0 & 0 & 0 & -1/\bar{c} & -1 & 0 & -x \end{bmatrix} \tag{2.12c}$$

with $\bar{c} = a^2/b^2$. Body forces can be treated by including ad-hoc solutions as presented in [76].

2.2.3 Assumed displacements

The interpolation of the displacement field $\mathbf{u}$ is controlled by the 24 components vector $\mathbf{d}_e = [\mathbf{u}^1, \ldots, \mathbf{u}^4, \boldsymbol{\varphi}^1, \ldots, \boldsymbol{\varphi}^4]$, where $\mathbf{u}^i \equiv \mathbf{u}[\mathbf{x}^i]$ and $\boldsymbol{\varphi}^i \equiv \boldsymbol{\varphi}[\mathbf{x}^i]$ denote displacements and rotation at node position $\mathbf{x}^i$, with $i = 1 \ldots 4$. Figure 2.1 shows the element geometry and the displacement degrees of freedom. As the stress assumption is inherently equilibrated, the internal work can be obtained by integrating on the element contour. The displacement interpolation $\mathbf{u}_k$ along element edge k is defined as the sum of three contributions

$$\mathbf{u}_k[\zeta] = \mathbf{u}_{kl}[\zeta] + \mathbf{u}_{kq}[\zeta] + \mathbf{u}_{kc}[\zeta] \tag{2.13a}$$

where $-1 \leq \zeta \leq 1$ is a one-dimensional coordinate along element edge k. The first term is a linear expansion

$$\mathbf{u}_{kl}[\zeta] = \frac{1}{2}[(1-\zeta)\mathbf{u}^i + (1+\zeta)\mathbf{u}^j], \tag{2.13b}$$

where superscripts i, j denote the nodes of element edge k. By using modular arithmetic and according to the local node numbering in Fig. 2.1, one has that $i = k$ and $j = k \pmod 4 + 1$. Letting $\boldsymbol{\varphi}^i = [\boldsymbol{\varphi}_f^i, \varphi_3^i]$, with $\boldsymbol{\varphi}_f^i = [\varphi_1^i, \varphi_2^i]$, the second and third terms correspond to quadratic and cubic expansions of the normal component of the element edge displacements

$$\mathbf{u}_{kq}[\zeta] = \frac{1}{8}\,L_k(\zeta^2-1)\begin{bmatrix} (\varphi_3^i - \varphi_3^j)\,\mathbf{n}_k \\ -(\boldsymbol{\varphi}_f^i - \boldsymbol{\varphi}_f^j)^T\mathbf{n}_k \end{bmatrix}, \quad \mathbf{u}_{kc}[\zeta] = \frac{1}{4}\,L_k(\zeta-\zeta^3)\begin{bmatrix} \mathbf{n}_k \\ 0 \end{bmatrix}\theta \tag{2.13c}$$

where $\mathbf{n}_k = [n_{kx}, n_{ky}]^T$ is the normal to the element edge, L_k is the edge length, and θ is the average in-plane distortional rotation defined as

$$\theta = \frac{1}{4}\sum_{i=1}^{4}\varphi_3^i - \bar{\varphi}_3 \tag{2.13d}$$

with $\bar{\varphi}_3$ the average in-plane rigid rotation of the element, whose expression can be found elsewhere [78].

The linear part $\mathbf{d}_{kl}$ and the quadratic contribution $\mathbf{d}_{kq}$ are continuous at the inter-element boundaries. Conversely, the cubic part $\mathbf{d}_{kc}$ corresponds to an incompatible mode, which is added to avoid rank defectiveness [77]. Finally, a simple linear interpolation for bending rotations is assumed along the edge

$$\boldsymbol{\varphi}_{fk}[\zeta] = \frac{1}{2}[(1-\zeta)\boldsymbol{\varphi}_{fi} + (1+\zeta)\boldsymbol{\varphi}_{fj}]. \tag{2.13e}$$

Compliance and compatibility finite element matrices

For the linear elastic problem, using a Hellinger-Reissner approach and the assumed displacement and generalised stresses interpolation one obtains

$$\int_{B_e} \boldsymbol{\sigma}^T \boldsymbol{\varepsilon} d\Omega_e - \frac{1}{2}\int_{B_e} \boldsymbol{\sigma}^T \mathbf{D}^{-1} \boldsymbol{\sigma} d\Omega_e - L_{ext} \equiv \boldsymbol{\beta}_e^T \mathbf{Q}_e \mathbf{d}_e - \frac{1}{2}\boldsymbol{\beta}_e^T \mathbf{H}_e \boldsymbol{\beta}_e - \mathbf{d}_e^T \mathbf{p}_e \tag{2.14}$$

where $\mathbf{F} = \mathbf{D}^{-1}$, L_{ext} is the work of the element external loads $\mathbf{p}_e$, and $\mathbf{H}_e$ and $\mathbf{Q}_e$ are the element compliance and the compatibility/equilibrium matrices. In particular

$$\mathbf{H}_e = \int_{B_e} \mathbf{N}_t^T \mathbf{D}^{-1} \mathbf{N}_t d\Omega_e,$$

while, since the compatibility matrix is due to self-equilibrated stress interpolation, it is evaluated through analytical contour integration as

$$\mathbf{Q}_e = \sum_{k=1}^{4} \mathbf{Q}_{ek} \tag{2.15}$$

where the matrix $\mathbf{Q}_{ek}$ is defined as

$$\boldsymbol{\beta}_e^T \mathbf{Q}_{ek} \mathbf{d}_e = \int_{-1}^{1} \left(\boldsymbol{\sigma}_m^T[\zeta] \mathbf{N}_{mk}^T \mathbf{u}_k[\zeta] + \boldsymbol{\sigma}_f^T[\zeta] \mathbf{N}_{fk}^T \boldsymbol{\varphi}_{fk}[\zeta] \right) \mathrm{d}\zeta \tag{2.16}$$

and the matrices $\mathbf{N}_{mk}, \mathbf{N}_{fk}$ split the components of the normal to the element edge and their explicit definition is reported elsewhere [78].

2.2.4 Linear-elastic problem

From the stationary condition of Eq.(2.14) one obtains the equilibrium equations and the constitutive laws of the element in discrete generalised format as

$$\begin{cases} \mathbf{H}_e \boldsymbol{\beta}_e - \mathbf{Q}_e \mathbf{d}_e = \mathbf{0} \quad \forall e \\ \mathbf{Q}_e^T \boldsymbol{\beta}_e - \mathbf{p}_e = \mathbf{0} \end{cases} \tag{2.17}$$

The stresses can be obtained from the first of Eqs. (2.17) at the FE level and then substituted into the equilibrium equation to obtain a pseudo-displacement format

$$\mathbf{K}_0 \mathbf{d} = \mathbf{p}, \tag{2.18}$$

where $\mathbf{K}_0$ and $\mathbf{p}$ are constructed by assembling the elemental contributions $\mathbf{Q}_e^T \mathbf{H}_e^{-1} \mathbf{Q}_e$ and $\mathbf{p}_e$, respectively, while $\mathbf{d}$ collects the nodal displacements of the whole structure. It is worth noting that the equilibrium condition in Eq. 2.18 has the same format than in usual displacement-based formulations and the stress parameters are evaluated only at the element level.

From now on, we will denote with a subscript e the eth element quantities and without any subscript the assembled global value.

2.3 Elasto-plastic analysis

The mixed FE previously presented in the linear-elastic case is herein extended to the elasto-plastic analysis of shell structures. For a structure made of a material with a non-linear constitutive law, the equilibrium condition in Eq. (2.18) becomes

$$\mathbf{s}[\mathbf{d}] - \lambda \mathbf{p} = \mathbf{0} \tag{2.19}$$

where λ is a load multiplier and $\mathbf{s}[\mathbf{d}]$ is the internal force vector of the structure evaluated by assembling the elemental contributions $\mathbf{s}_e[\mathbf{d}_e]$ which are defined in the following.

2.3.1 The incremental elastoplastic analysis

Equation (2.19) is usually solved by means of a continuation method which gives a sequence of equilibrium points, with coordinates $\{\mathbf{d}, \lambda\}$, forming the so-called equilibrium path. Since a deeper discussion has already been given in 1.1, here I just poit out that the following system representing the equilibrium equations plus the arc-length constraint for an assigned value of ξ

$$\begin{cases} \mathbf{r}[\mathbf{d},\, \lambda] \equiv \mathbf{s}[\mathbf{d}] - \lambda \mathbf{p} = \mathbf{0} \\ r_\lambda[\mathbf{d},\, \lambda] \equiv g[\mathbf{d}, \lambda] - \xi \end{cases} \tag{2.20}$$

is solved globally in displacement variables and load proportionality factor only, while the stresses are maintained at the element level exclusively, and evaluated using a return mapping scheme, as described in the next section.

The internal force vector at each iteration, $\mathbf{s}^j$, is evaluated by assembling the contribution of each element as

$$\mathbf{s}_e^j \equiv \mathbf{Q}_e^T \boldsymbol{\beta}_e[\boldsymbol{\beta}^{(n)}, \Delta \mathbf{d}_e^j]. \tag{2.21}$$

2.3.2 A layerwise approach for the evaluation of the shell element response

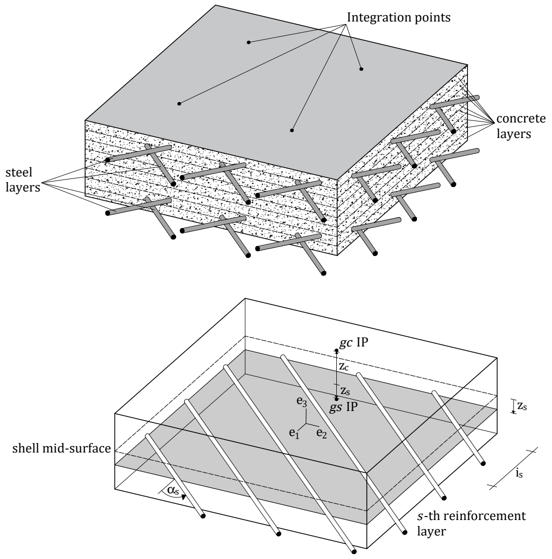

Figure 2.2: Layered reinforced concrete shell with four reinforcing layers (left-hand side) and detail of single steel and concrete IPs (right-hand side).

Figure 2.2 shows the generic material composition of the shell FE. In particular, it is made of concrete and a certain number of reinforcement layers. Each reinforcement layer, identified by the the subscript s, has orientation α_s with respect to the element local Cartesian axis

$\mathbf{e}_1$, rebar area A_s, spacing i_s and depth z_s with respect to the shell mid-surface. A grid of n_g IPs is considered over the shell mid-plane and, for each of them, further IPs along the thickness direction are adopted. As shown in Fig. 2.2, the IPs are located in the position $\mathbf{x}_{gc} = [\mathbf{x}_g, z_c]$, where $\mathbf{x}_g$ is the position over the mid-surface, while z_c indicates the distance along the thickness direction from the mid-surface. The vector of the generalised shell stresses at the g-th mid-surface IP is evaluated using Eq. (2.8) as

$$\boldsymbol{\sigma}_g = \boldsymbol{\sigma}[\mathbf{x}_g] = \int_{-h/2}^{h/2} \mathbf{Y}[z]^T \mathbf{S}[\mathbf{x}_g, z]\, dz = \sum_{c=1}^{n_c} \mathbf{Y}[z_c]^T \mathbf{S}_{gc} w_c + \sum_{s=n_c+1}^{n_c+n_s} \mathbf{Y}[z_s]^T \mathbf{S}_{gs} \frac{A_s}{i_s} \tag{2.22}$$

where n_c is the number of concrete IPs along the thickness, n_s is the number of steel layers, $\boldsymbol{\sigma}_{gc}$ are the concrete stresses at the c-th integration point along the thickness direction, w_c is the corresponding weight and $\boldsymbol{\sigma}_{gs}$ are the stresses of the s-th reinforcement layer.

The stresses in both concrete and steel must satisfy the plastic admissibility in each IP, expressed by

$$f_m[\boldsymbol{\sigma}_{gm}] \leq 0, \quad m = 1, \ldots, n_c + n_s \tag{2.23}$$

where with m we identify the generic IP and f_m is the related yield function. Omitting, from now on, the superscript $(n+1)$, the stresses $\boldsymbol{\sigma}_{gc}$ and $\boldsymbol{\sigma}_{gs}$ are independently evaluated by solving the IP state determination at level of material point

$$\begin{cases} \mathbf{F}(\boldsymbol{\sigma}_{gm} - \boldsymbol{\sigma}_{gm}^{(n)}) + \mu_{gm} \dfrac{\partial f_m[\boldsymbol{\sigma}_{gm}]}{\partial \boldsymbol{\sigma}_{gm}} - \Delta\boldsymbol{\varepsilon}_{gm} = \mathbf{0} \\ \mu_{gm} f_m[\boldsymbol{\sigma}_{gm}] = 0 \quad \mu_{gm} \geq 0 \quad f_m[\boldsymbol{\sigma}_{gm}] \leq 0 \end{cases} \qquad \forall m = 1, \ldots, n_c + n_s. \tag{2.24}$$

where $\mathbf{F} = \mathbf{C}^{-1}$ μ_{gm} are the positive plastic multipliers, $\Delta\boldsymbol{\varepsilon}_{gm} = \mathbf{Y}[z_m]\Delta\boldsymbol{\rho}_g$ represents the strain on the mth IP, while the assigned $\Delta\boldsymbol{\rho}_g$ is constant for each m.

As shown elsewhere [128, 132, 97, 98, 80], the stress parameters $\boldsymbol{\beta}_e = \boldsymbol{\beta}_e[\boldsymbol{\beta}_e^{(n)}, \Delta\mathbf{d}_e]$ for an assigned value of $\Delta\mathbf{d}_e$ are obtained using the element state determination defined by the following additional equations

$$\begin{cases} \mathbf{r}_g \equiv \mathbf{t}_g - \mathbf{N}_{tg}\boldsymbol{\beta}_e = \mathbf{0}, & \forall g \\ \mathbf{r}_e \equiv \mathbf{Q}_e \Delta\mathbf{d}_e - \sum_g \mathbf{N}_{tg}^T \Delta\boldsymbol{\rho}_g w_g = \mathbf{0}. \end{cases} \tag{2.25}$$

The first one imposes that the generalised stresses $\boldsymbol{\sigma}_g$ coming from the solution of the IP state determination in Eq. (2.24) and evaluated using Eq. (2.22), are the same than those furnished by the assumed stress interpolation. The second equation imposes, in a weak form, the strain/displacement relation over the element.

2.3.3 IP state determination

The problem of IP state determination in Eq. (2.24) can be solved using a standard return mapping algorithm commonly used for displacement-based formulations [50], based on a strain driven approach and a backward Euler integration. Such scheme also furnishes the algorithmic tangent stiffness matrix $\mathbf{C}_{gm}$ of the problem at each IP along the thickness direction defined as

$$\mathbf{C}_{gm} \equiv \frac{\partial \mathbf{S}_g}{\partial \mathbf{E}_m}.$$

The algorithmic tangent stiffness in terms of shell stress resultant is then evaluated as

$$\mathbf{D}_g \equiv \frac{\partial \boldsymbol{\sigma}_g}{\partial \boldsymbol{\varepsilon}_g} = \sum_m \mathbf{Y}_m^T \mathbf{C}_{gm} \mathbf{Y}_m w_m \tag{2.26}$$

Element state determination

The solution of Eq.(2.25) is obtained by the Newton method. Since $\Delta\mathbf{d}_e$ is assigned, the problem unknowns $\Delta\boldsymbol{\varepsilon}_g$ and $\boldsymbol{\beta}_e$ are evaluated as a sequences of estimates which correct the current values $\boldsymbol{\beta}_e^j$ and $\Delta\boldsymbol{\rho}_g^j$ as

$$\Delta\boldsymbol{\varepsilon}_g^{j+1} = \Delta\boldsymbol{\varepsilon}_g^{j} + \dot{\boldsymbol{\varepsilon}}_g \qquad \boldsymbol{\beta}_e^{j+1} = \boldsymbol{\beta}_e^{j} + \dot{\boldsymbol{\beta}}_e \tag{2.27}$$

being

$$\begin{cases} \mathbf{D}_g^j \dot{\boldsymbol{\varepsilon}}_g - \mathbf{N}_{tg}\dot{\boldsymbol{\beta}}_e = -\mathbf{r}_g^j & \forall g \\ -\sum_g \mathbf{N}_{tg}^T \dot{\boldsymbol{\varepsilon}}_g w_g = -\mathbf{r}_\epsilon^j \end{cases} \qquad \text{and} \qquad \mathbf{D}_g^j = \left.\frac{\partial \mathbf{t}_g[\Delta\boldsymbol{\rho}_g]}{\partial \boldsymbol{\rho}_g}\right|_{\Delta\boldsymbol{\rho}_g = \Delta\boldsymbol{\rho}_g^j}.$$

The tangent matrix $\mathbf{D}_g^j$ for each IP is evaluated during the IP state determination phase using Eq.(2.26). Solving, one obtains

$$\begin{aligned} \dot{\boldsymbol{\varepsilon}}_g &= (\mathbf{D}_g^j)^{-1}\left(\mathbf{N}_{tg}\dot{\boldsymbol{\beta}}_e - \mathbf{r}_g^j\right) \\ \dot{\boldsymbol{\beta}}_e &= \mathbf{H}_t^{-1}\left(\mathbf{r}_e^j + \sum_g \mathbf{N}_{tg}^T (\mathbf{D}_g^j)^{-1}\mathbf{r}_g^j\right) \end{aligned} \tag{2.28}$$

with

$$\mathbf{H}_t \equiv \left(\sum_g \mathbf{N}_{tg}^T (\mathbf{D}_g^j)^{-1} \mathbf{N}_{tg} w_g\right).$$

The first trial values of $\Delta\boldsymbol{\varepsilon}_g$ and $\Delta\boldsymbol{\beta}_e$ can be chosen using the solution of the previous consolidated step of the incremental analysis. Once convergence is achieved, i.e. when a given norm of the residuals $\mathbf{r}_e$ and $\mathbf{r}_g$ is below a given tolerance, the internal forces $\mathbf{s}_e[\mathbf{d}^{(n)}, \Delta\mathbf{d}_e]$ of the element can be evaluated using Eq.(2.21). Similarly, the element algorithmic tangent matrix is obtained as

$$\mathbf{K}_e[\mathbf{d}^{(n)}, \Delta\mathbf{d}_e] = \mathbf{Q}_e^T \mathbf{H}_t^{-1} \mathbf{Q}_e. \tag{2.29}$$

2.4 Mechanical response of the RC layers

In this Section the non-linear response of the materials composing the shell thickness is described. An elastic perfectly plastic behaviour is assumed, but the proposed approach can be readily extended to more general non-linear constitutive models.

2.4.1 Concrete

The stress response of concrete, $\boldsymbol{\sigma}_{gc}$, relative to the generic IP along the thickness is evaluated by solving problem (2.24) on the basis of an elastic isotropic behaviour defined by the Young modulus, E_c, Poisson ratio, ν_c, of concrete and the yield surface proposed in [103]. This kind of surface, as other surfaces already proposed in literature [57], allows to describe parabolic meridians and a variable shape on the deviatoric plane. Moreover, the formulation proposed in [103] uses only the compressive strength of the concrete, $\overline{\sigma}_c$, to express a loading surface which is usually expressed by three distinct parameters. Assuming, as already stated in the Introduction, a perfectly plastic behaviour, the yield function is formulated as follows

$$f_c \equiv \frac{3}{\overline{\sigma}_c^2} J_2 + \frac{m}{\sqrt{3}\,\overline{\sigma}_c}\sqrt{J_2}\, r(\theta, e) + \frac{m}{3\,\overline{\sigma}_c} I_1 - 1\,. \tag{2.30}$$

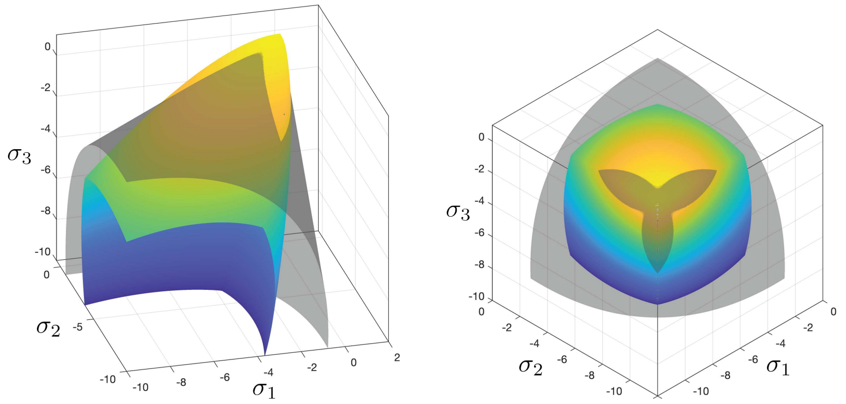

Figure 2.3: Adopted concrete yield function (coloured surface) compared with a Drucker-Prager cone (grey surface).

where the stress invariants, I_1 and J_2, and the Lode angle, θ, have the usual definition, namely

$$\begin{aligned} I_1 =& \sigma_1 + \sigma_2 + \sigma_3 \\ J_2 =& \frac{1}{6}\left((\sigma_1 - \sigma_2)^2 + (\sigma_1 - \sigma_3)^2 + (\sigma_2 - \sigma_3)^2\right) \\ \theta =& \frac{1}{3}\cos^{-1}\left(\frac{3\sqrt{3}}{2}\frac{J_3}{J_3^{3/2}}\right) \\ J_3 =& \left(\sigma_1 - \frac{I_1}{3}\right)\left(\sigma_2 - \frac{I_1}{3}\right)\left(\sigma_3 - \frac{I_1}{3}\right) \end{aligned}$$

where σ_1, σ_2 and σ_3 are the principal stresses. The expression of the material parameters m and e, together with the details about their derivation and how are linked to $\overline{\sigma}_c$, are given in the already cited paper [103]. Figure 2.3 shows, in the space of the principal stresses, the shape of the yield surface (2.30) comparing it with the Drucker-Prager cone defined on the basis of the tensile and biaxial compressive strengths of the concrete.

The Newton-Raphson solution of Eq. (2.24) provides, for the generic concrete IP, the required stress $\boldsymbol{\sigma}_{gc}$ but also the consistent tangent operator $\mathbf{C}_{gc}$ which can be evaluated as

$$\mathbf{C}_{gc} = \mathbf{F}_{tc}^{-1} = \boldsymbol{\Xi} - \frac{\boldsymbol{\Xi}\frac{\partial f_c}{\partial \boldsymbol{\sigma}} \otimes \boldsymbol{\Xi}\frac{\partial f_c}{\partial \boldsymbol{\sigma}}}{\frac{\partial f_c}{\partial \boldsymbol{\sigma}} \cdot \boldsymbol{\Xi}\frac{\partial f_c}{\partial \boldsymbol{\sigma}}}\,, \quad \boldsymbol{\Xi}^{-1} = \mathbf{F}_c + \mu_{gc}\frac{\partial^2 f_c}{\partial \boldsymbol{\sigma}^2}\,, \tag{2.31}$$

and ready to be used in Eq. (2.26).

2.4.2 Steel reinforcement

Equation (2.24) is also solved for the generic steel reinforcement layer whose uniaxial mechanical response is now simply defined by the Young modulus E_s, the yield stress $\overline{\sigma}_s$ and the vector components $c = \cos\alpha_s$ and $s = \sin\alpha_s$ defined by rebar orientation, α_s, with respect to the axes describing the shell mid-surface. In particular, in the elastic phase, the mechanical response is defined by

$$\mathbf{S}_{gs} = \mathbf{S}_{gs}^{(n)} + \mathbf{F}_s^{-1}\,\Delta\mathbf{E}_{gs}\,, \quad \mathbf{F}_s^{-1} = E_s \begin{bmatrix} c^4 & c^2s^2 & c^3s & 0 & 0 \\ c^2s^2 & s^4 & s^3c & 0 & 0 \\ c^3s & s^3c & c^2s^2 & 0 & 0 \\ 0 & 0 & 0 & 0 & 0 \\ 0 & 0 & 0 & 0 & 0 \end{bmatrix}. \tag{2.32}$$

In the plastic phase the mechanical response is given by

$$\boldsymbol{\sigma}_{gs} = \pm\overline{\sigma}_s \begin{bmatrix} c^2 & s^2 & -cs & 0 & 0 \end{bmatrix}^T , \quad \mathbf{F}_{ts}^{-1} = \mathbf{0}_{5\times 5} . \tag{2.33}$$

2.5 Numerical results

Efficiency and accuracy of the proposed FE strategy are now tested in some numerical applications. Results in terms of static non-linear response are compared with those provided by other approaches. In particular, the following models are used

- S4, which is a linear four noded quadrilateral Mindlin-Reissner shell FE implemented in Abaqus [127] with 24 kinematical DOFs; concrete is modelled using an elastic perfectly plastic Concrete Damage Plasticity (CDP) [75] material, while elastic perfectly plastic von Mises is used to describe the steel behaviour. A grid of $n_g = 2 \times 2$ Gauss IPs is used over the shell mid-surface.
- CT6, which is a quadratic, six noded triangular Mindlin-Reissner shell FE with 36 kinematical DOFs; concrete and steel behaviour are described by the same constitutive models presented in Section 2.4. The numerical integration over the mid-plane is performed using 7 IPs.

For MISS-4, a grid of $n_g = 3 \times 3$ Gauss IPs over the FE mid-surface is used. For a fair comparison, for each mid-surface IP, $n_c = 12$ concrete IPs are considered along the thickness direction in all the shell FE models.

In particular, MISS-4 is compared with S4 and CT6 in terms of convergence rate. In addition, results obtained with a fine mesh of S4 is used as a baseline solution for the equilibrium path and the collapse load.

The pointwise convergence rate is evaluated by reporting, in a double-logarithmic scale, the error $\mathcal{E}_\lambda = \| \frac{\lambda - \lambda^{ref}}{\lambda^{ref}} \|$ versus h, where h is the square root of the number of DOFs used. The error $\mathcal{E}_\lambda$ is evaluated with respect to the load multipliers associated to a fixed maximum value of a displacement compontent assumed as the referce DOF for each test. For each model, a reference solution λ_{ref} is evaluated using a very fine discretisation.

In all the tests, only the concrete compressive strength, $\overline{\sigma}_c$, is indicated. All the other parameters are derived following Papanikolaou and Kappos [103]. For steel reinforcement, the yield stress is $\overline{\sigma}_s = 450$ [MPa], the Young modulus $E_s = 2.1 \times 10^5$ [MPa] and the Poisson ratio $\nu_s = 0.3$, if not differently specified.

2.5.1 Accuracy of the constitutive integration algorithm

The accuracy of the constitutive integration algorithm of the generic concrete IP is herein assessed by means of iso-error maps [125]. To this end, four points on the yield surface (uniaxial tension and compression, biaxial compression and pure shear) are considered and the corresponding principal strain components $\bar{\varepsilon}_1$ and $\bar{\varepsilon}_2$ are evaluated. Starting from these points, a sequence of strain increments ($\Delta\varepsilon_1$, $\Delta\varepsilon_2$) along the principal directions is applied [125] and, for each of them, the stress state $\boldsymbol{\sigma}$ is evaluated by solving Eq. (2.24). The iso-error maps represent the error

$$\delta = \frac{\sqrt{(\boldsymbol{\sigma} - \boldsymbol{\sigma}_{ref})^T(\boldsymbol{\sigma} - \boldsymbol{\sigma}_{ref})}}{\sqrt{\boldsymbol{\sigma}_{ref}^T \boldsymbol{\sigma}_{ref}}} \cdot 100 \tag{2.34}$$

as a function of the strain increments. The reference solution $\boldsymbol{\sigma}_{ref}$ is obtained by repeatedly solving Eq. (2.24) with increasing numbers of sub-increments until a converged value is obtained. The obtained iso-error maps are shown in Figure 2.4 where it is possible to observe that in all cases, for strain increments of the same order of magnitude of the yield strain, the error is below the 5% which can be considered as an acceptable value [125].

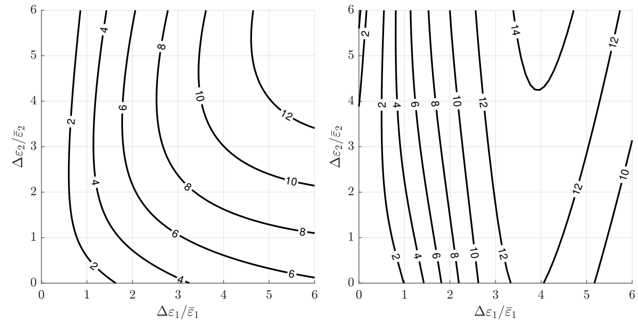

uniaxial tension uniaxial compression

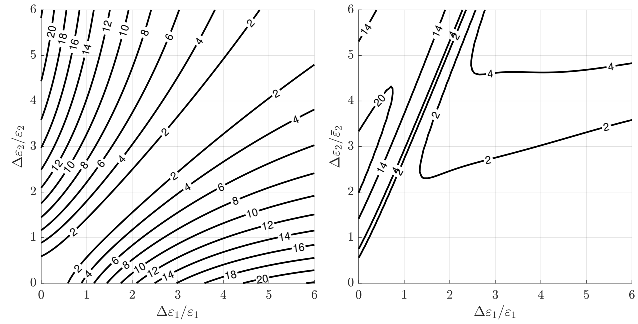

biaxial compression pure shear

Figure 2.4: Iso-error maps for a generic concrete IP obtained starting from four different initial stress states.

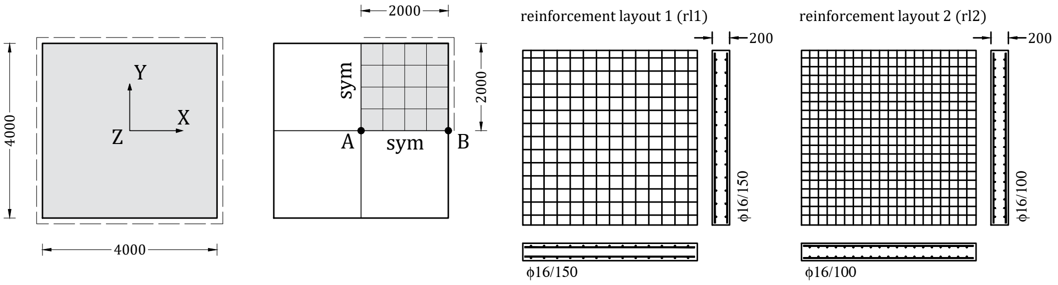

Figure 2.5: Reinforced concrete square plate: geometry, boundary conditions and mesh 4 × 4. All lengths are in mm.

2.5.2 Square plate

The first test regards the reinforced concrete square plate of length $L = 4$ [m] and thickness $s = 0.2$ [m] represented in Fig. 2.5. Two reinforcement layouts are considered, differing for the bar spacing. The compressive strength used for concrete is $\overline{\sigma}_c = 30$ [MPa]. According to the symmetry of the problem, only a quarter of the plate is analysed. Two boundary conditions are taken into consideration, namely simply supported and clamped. The plate is subjected to a uniformly distributed out-of-plane pressure of amplitude $q = \lambda\, M_p/L^2$, where M_p is the plastic bending moment obtained using a uniaxial yield condition and considering only the concrete in compression and the steel in tension, namely $-\overline{\sigma}_c \leq \sigma_{xx}^{(c)} \leq 0$ for concrete and $0 \leq \sigma_{xx}^{(s)} \leq \overline{\sigma}_s$.

Table 2.1 reports the load multipliers obtained for a value of the displacement at the plate centre, $u_z^A = 100$ [mm]. The solutions obtained by several meshes of MISS-4 elements are compared with the result provided by Abaqus with a 16×16 mesh of S4 elements. The same analyses are compared in Figs. 2.6 and 2.7 where the equilibrium curves are reported. The results show a good agreement between the proposed formulation and Abaqus, even in

Table 2.1: Reinforced concrete square plate: ultimate ($u_z^A = 100$ [mm]) load multiplier.

B.C.	reinf. layout	2×2	4×4	8×8	16×16	S4-CDP
supported	rl1	23.2644	23.4824	23.5056	23.5282	23.051
	rl2	22.8898	23.1895	23.2061	23.2100	22.676
clamped	rl1	45.6447	44.3623	42.8930	41.7100	43.401
	rl2	45.4340	43.8796	42.3289	41.0107	43.107

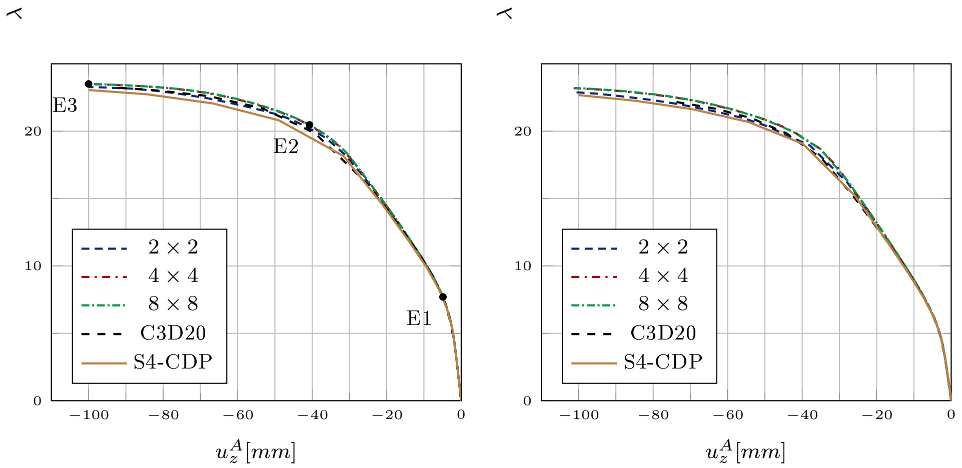

rl1 rl2

Figure 2.6: Reinforced concrete square plate, supported condition: equilibrium curves.

the case of the coarsest mesh. A further comparison, in the supported case, is made with C3D20, which is a quadratic solid FE implemented in Abaqus [127] with 20 nodes where the PK model is implemented using a U-MAT subrutine.

The accuracy of the proposed formulation is also highlighted in Fig. 2.8 where the convergence curves given by MISS-4 are compared to CT6 and S4. The prosed formulation shows lower errors for all values of the numbers of degrees of freedom considered and satisfactory error reduction rates.

Figure 2.9 shows the stress profile of a normal stress for concrete ($\sigma_{xx}^{(c)}$) and steel ($\sigma_{xx}^{(s)}$) along the thickness in the plate centre A, with respect to the equilibrium points E1, E2 and E3 (see Fig. 2.6). Figure 2.10 shows the same output for the clamped boundary condition in points A and B, as indicated in Fig. 2.5.

Finally, Figs. 2.11 and 2.12 plot for the boundary conditions supported and clamped, respectively, the distribution of the norm of the generalised plastic strain vector with respect to equilibrium points E2 and E3. The development of yield lines can be better appreciated for the supported case while the clamped condition highlights the formation of plastic zones along the boundary of the whole plate.

2.5.3 In-plane loaded reinforced concrete wall

A RC wall having dimensions $B = 3$ [m], $H = 6$ [m] and thickness $h = 0.3$ [m] is analysed. Geometry, reinforcement layout, loading and boundary conditions are pictured in Fig. 2.13. For concrete $\overline{\sigma}_c = 30$ [MPa] is assumed. The wall is loaded on the top edge by a constant vertical load q_0 and by a horizontal load λq_x where $q_x = 0.3$ [MPa m]. Nodes at the base are fully restrained.

Two load conditions are considered, one condition with the vertical load equal to zero and the other with the vertical load equal to $0.2\, h\, \overline{\sigma}_c$. Table 2.2 reports, for the three regular meshes used, the values of the load multiplier λ relative to 80 [mm] drift. Results show that

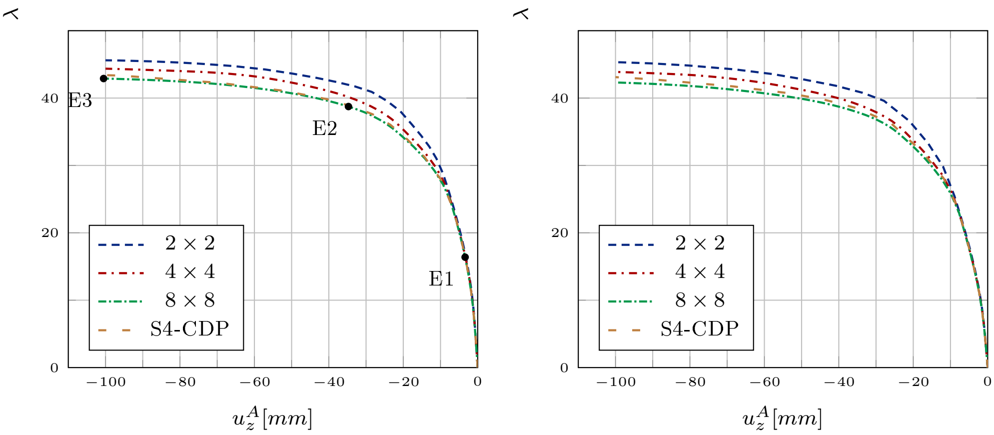

rl1 rl2

Figure 2.7: Reinforced concrete square plate, clamped condition: equilibrium curves.

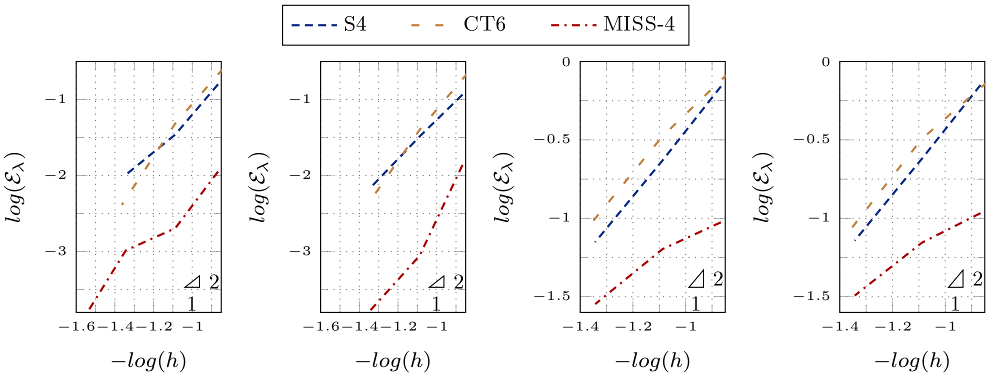

supported - rl1 supported - rl2 clamped - rl1 clamped - rl2

Figure 2.8: Reinforced concrete square plate: convergence curves.

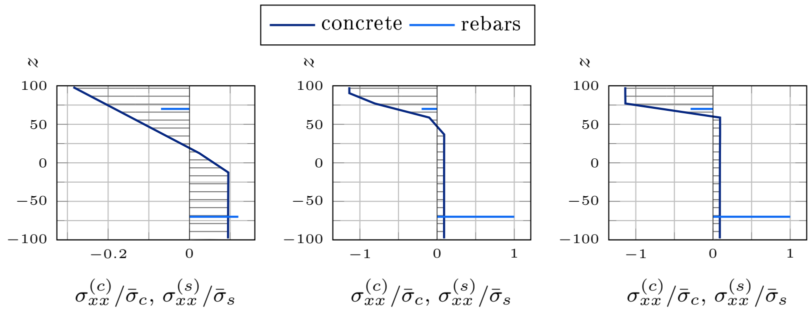

E1 - A E2 - A E3 - A

Figure 2.9: Reinforced concrete square plate, supported condition: through the thickness normal stress profile for rl1 reinforcement layout.

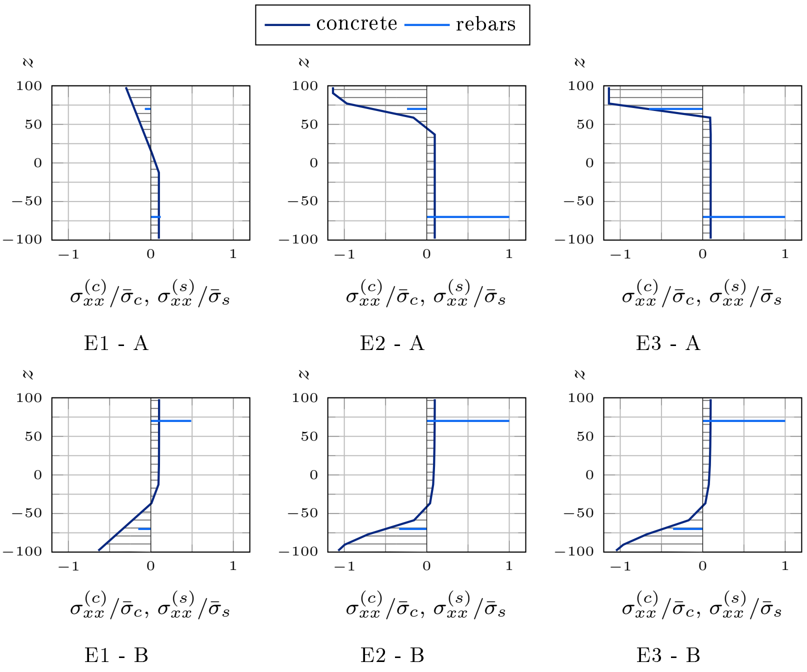

E1 - A
E2 - A
E3 - A
E1 - B
E2 - B
E3 - B

Figure 2.10: Reinforced concrete square plate, clamped condition: through the thickness normal stress profile for rl1 reinforcement layout.

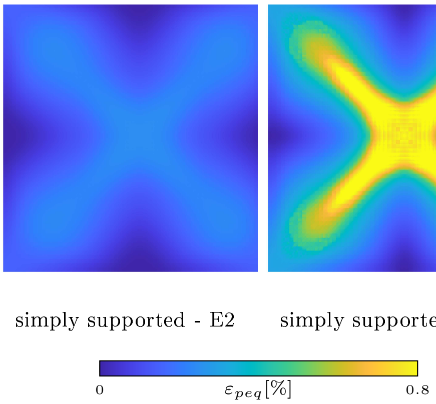

simply supported - E2
simply supported - E3

Figure 2.11: Reinforced concrete square plate, supported condition: evolution of the norm of generalized plastic strain (whole structure).

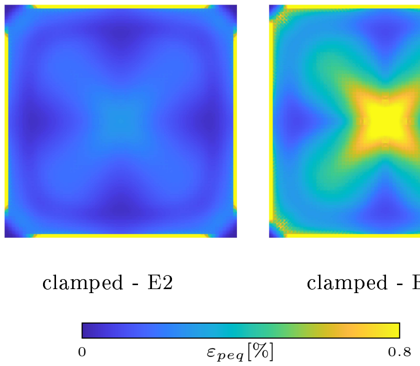

clamped - E2

clamped - E3

Figure 2.12: Reinforced concrete square plate, clamped condition: evolution of the norm of generalized plastic strain (whole structure).

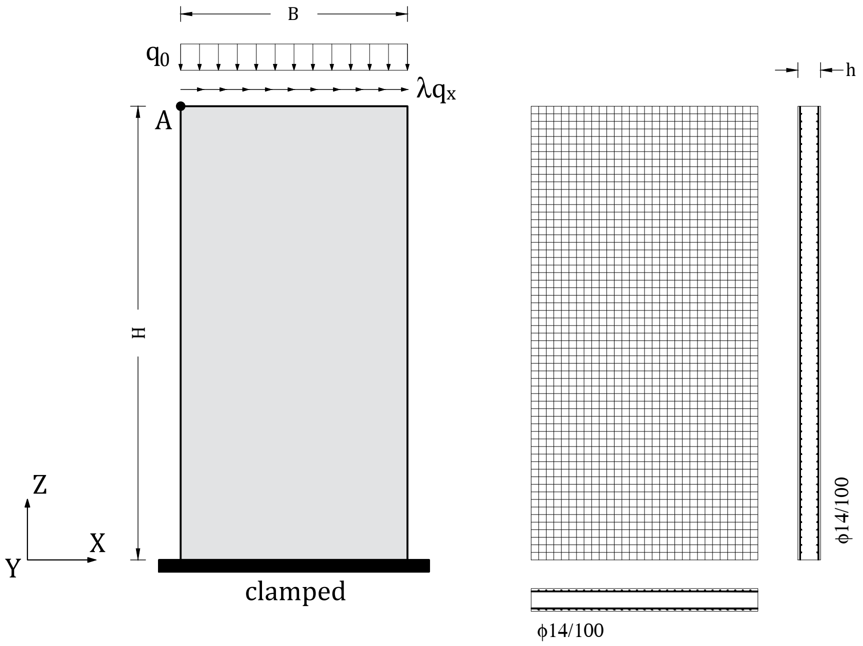

Figure 2.13: Reinforced concrete wall: geometry and boundary conditions. All lengths are in mm.

Table 2.2: Reinforced concrete wall: ultimate ($u_{\max} = 80$ [mm]) load multiplier.

q_0	2×4	4×8	8×16	S4-CDP
0	1.694	1.646	1.613	1.658
$0.2\, s\, \overline{\sigma}_c$	2.579	2.505	2.447	2.491

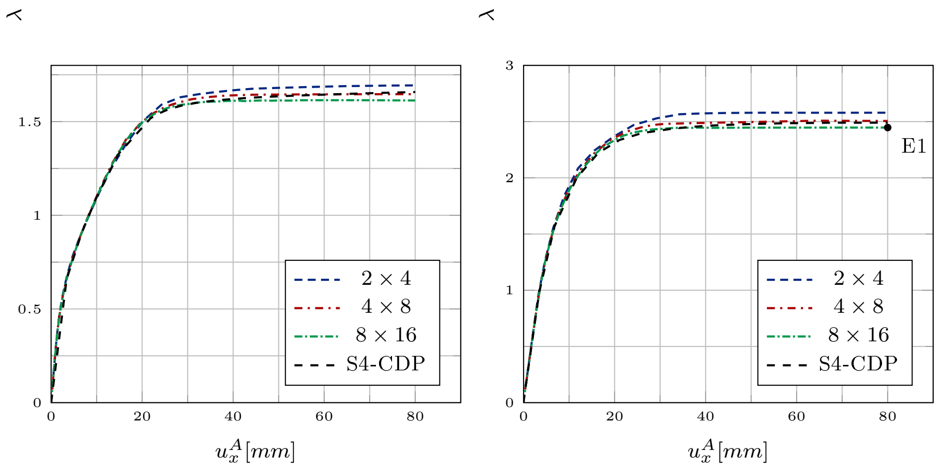

$q_0 = 0$ $\qquad$ $q_0 = 0.2\, s\, f_c$

Figure 2.14: Reinforced concrete wall: equilibrium curves.

also with the coarsest mesh MISS-4 well approximates the solution obtained through the Abaqus S4 element with a mesh 16 × 32. The comparison in terms of equilibrium curves is shown in Fig. 2.14 which highlights that the solution is good in all the equilibrium points even with a very coarse mesh. Figure 2.15 emphasizes the good convergence properties of MISS-4, also in this case characterised by a quadratic convergence rate and a very low error for the coarsest meshes. The norm of the generalised plastic strain of the structure is depicted in Fig. 2.16 with respect to the equilibrium point E1 (see Fig. 2.14), for increasingly finer meshes. It is possible to observe how plastic deformations concentrate in the wall base section. Similarly, Fig. 2.17 shows the stress component N_y at equilibrium point E1 for different meshes.

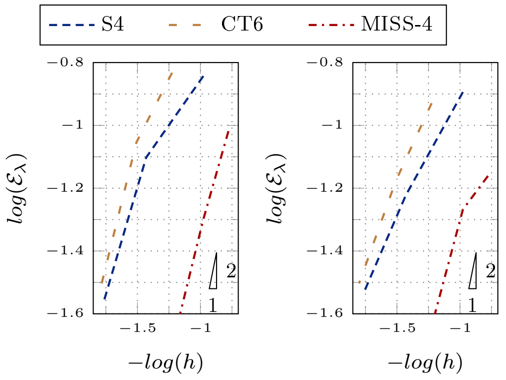

$p_0 = 0$ $\qquad$ $p_0 = 0.2 s f_c$

Figure 2.15: Reinforced concrete wall: convergence curves.

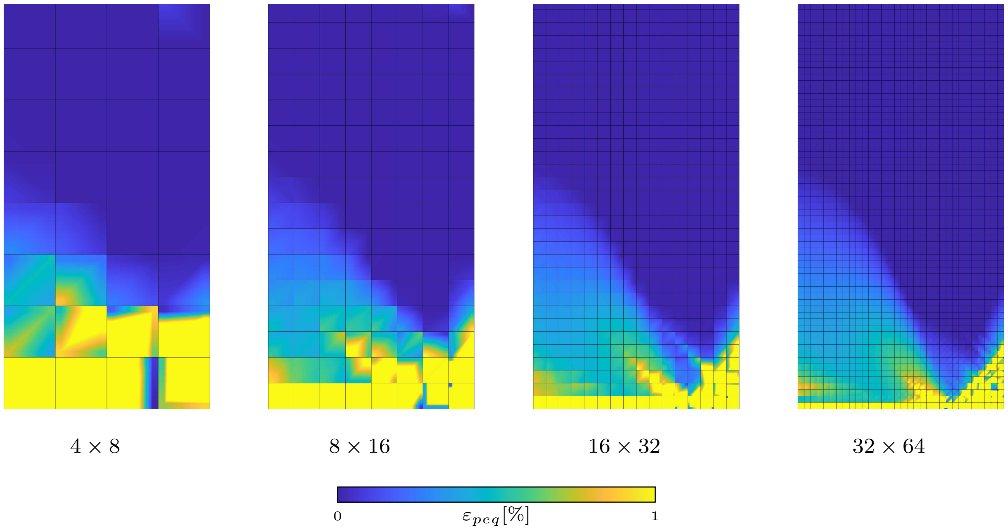

4 × 8 8 × 16 16 × 32 32 × 64

Figure 2.16: Reinforced concrete wall: equivalent plastic strain for different meshes at equilibrium point E1.

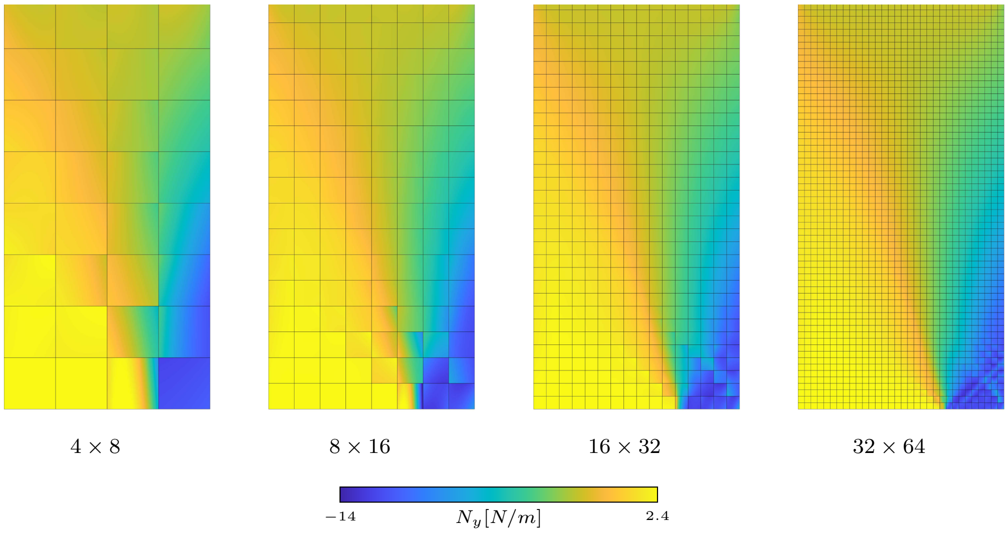

4 × 8 8 × 16 16 × 32 32 × 64

Figure 2.17: Reinforced concrete wall: generalised stress N_y for different meshes at equilibrium point E1.

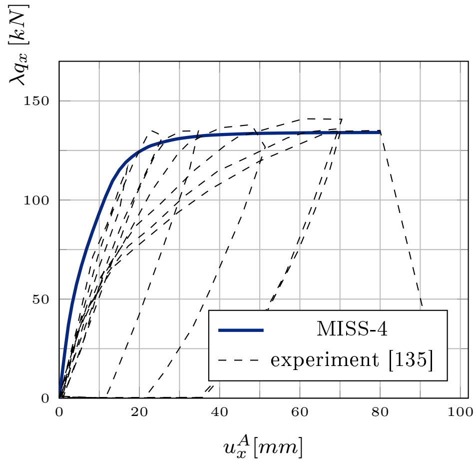

Figure 2.18: Reinforced concrete wall RW1: equilibrium curve with the present model and experimental behaviour.

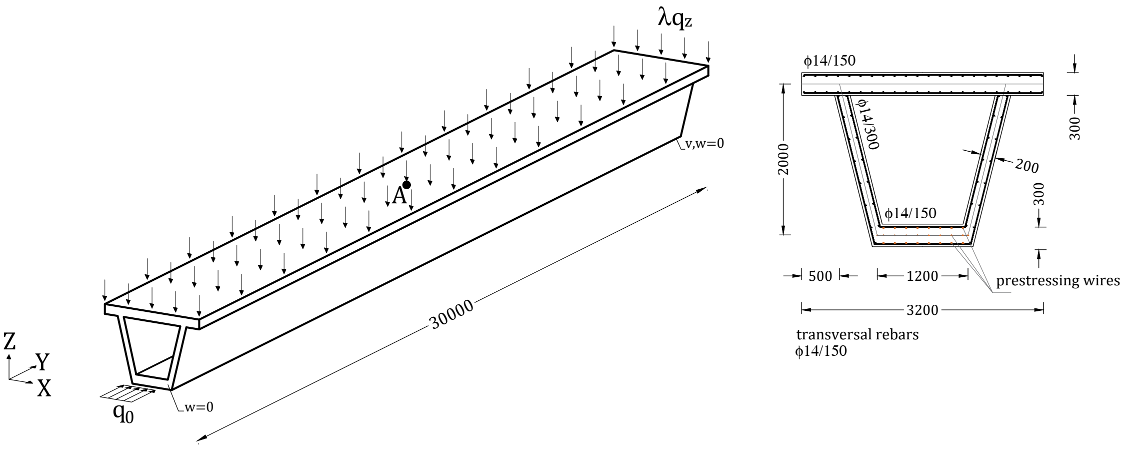

3D view

Cross-section

Figure 2.19: Prestressed girder: geometry, loads and boundary conditions. All lengths are in mm.

Comparison with experimental results

In order to test the capability of the proposed model to capture actual structural behaviour, a comparison with experimental results is performed. In particular, we analyse the shear-wall shown in Fig. 2.13 on the basis of the data adopted for the wall RW1 tested by Thomsen and Wallace [135]. This test belongs to a well-known experimental campaign which is often adopted as a baseline to assess the accuracy of bidimensional RC numerical models [138].

Figure 2.18 compares the experimental results obtained by applying a cyclic loading history with the numerical response evaluated through the proposed FE model subjected to a monotonic load. It is possible to observe good agreement in terms of initial elastic response and maximum shear force sustained by the wall.

2.5.4 Prestressed girder

A prestressed girder of length $L = 30$ [m] is herein considered whose geometry, loads, reinforcement layout and boundary conditions are shown in Fig. 2.19. The beam is simply-supported at the two end sections, while it is free to deform axially. The concrete compressive strength is $\overline{\sigma}_c = 40$ [MPa]. Prestressing tendons are located in the bottom plate and made

Table 2.3: Prestressed girder: number of elements along the girder cross section and longitudinal direction.

Mesh	top/web/bottom	lateral	longitudinal
1	2	1	6
2	4	1	12
3	8	2	24

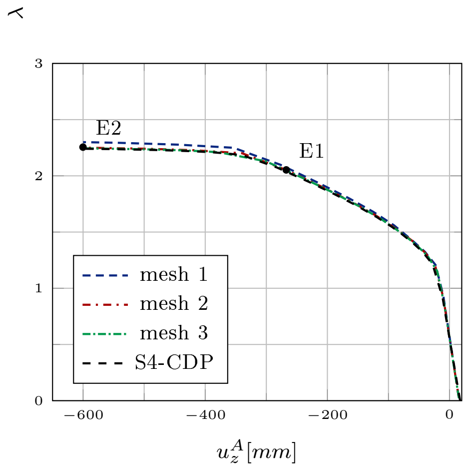

Figure 2.20: Prestressed girder: equilibrium curves.

of harmonic steel characterised by a yield stress $\overline{\sigma}_s = 1500$ [MPa]. Elsewhere, the steel reinforcement has $\overline{\sigma}_s = 450$ [MPa]. The analyses with MISS-4 element are performed using the three meshes specified in Table 2.3.

The load is applied following two phases. In the first phase the girder is subjected to a compressive loading , $q_0 = 4.62$ [MPa m], applied to the bottom slab in order to simulate the prestress load. A uniformly distributed pressure λq_z is subsequently applied to the top slab, where $q_z = 0.04$ [MPa].

Figure 2.20 reports the equilibrium curves of the vertical midpoint displacement. The proposed model, also in this case, is in good agreement with the Abaqus solution, while it is more efficient in improving the accuracy of the solution. Figure 2.21 shows the contour plots of the norm of generalised plastic strain relative to the equilibrium points E1 and E2 indicated in Fig. 2.20. Plastic strains start to accumulate in the bottom plate and collapse is reached when also the web is fully plastic.

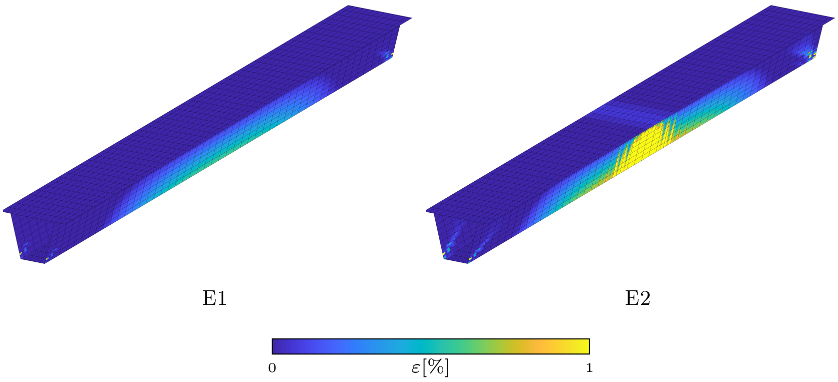

E1

E2

Figure 2.21: Prestressed girder: norm of the generalised plastic strain.

2.6 Summary

A numerical framework for the analysis of Reinforced Concrete (RC) shell structures undergoing material non-linearities was proposed. It is based on a mixed shell Finite Element (FE), named MISS-4, characterized by assumed stresses that a-priori satisfy equilibrium equations. A solid-like behavior was obtained using a layer-wise approach. The non-linear material behavior of the concrete was modeled through a constitutive equation based on a confinement-sensitive plasticity-based yield surface expressed in terms of Cauchy stresses. Conversely, a uni-axial elastic perfectly plastic behavior was adopted for the reinforcement bars. Results showed that the proposed approach is accurate if compared with other FEs in recovering the static non-linear equilibrium path. Additionally, the good performance already shown by MISS-4 in different contexts, namely the linear-elastic and geometrically non-linear analysis of composite structures, was confirmed also in the elasto-plastic analysis of RC structures. In particular, low error on coarse meshes and a quadratic rate of convergence was observed. The proposed approach can be readily extended to even more complex material behaviors that may include hardening, damage or cracking. Additional layers can also be considered in order to efficiently model materials for retrofitting, as fiber reinforced polymers or cementitious matrices. Further enrichment is the extension to the geometrically non-linear behavior, where MISS-4 has already been successfully employed in the analysis of elastic materials. Finally, the proposed approach can be used for the implementation of efficient dynamic non-linear analyses of full scale RC structures.

Chapter 3

Large deformation Kirchhoff-Love shell hierarchically enriched with warping: isogeometric formulation and modeling of alternating stiff/soft layups

This chapter presents a large deformation Kirchhoff-Love shell model hierarchically enhanced with through-the-thickness warping functions, arbitrarily chosen by the user. Two unknowns are introduced for each of them, representing its amplitudes in two directions tangent to the shell surface. NURBS are used to approximate reference surface displacement and warping amplitudes in the weak form. The transverse shear strains are linear functions of the warping parameters only and naturally free from locking. A patch-wise reduced integration avoids membrane locking and improves efficiency. Particular attention is paid to the modeling of composites made up of multiple stiff layers coupled with soft interlayers. The alternating layup with high stiffness ratios induces a significant sectional warping with transverse shear strains concentrated in the soft layers. Two warping models are investigated: WI) all stiff layers maintain the same director orthogonal to the deformed surface with independent transverse shear deformations of the soft layers; WZ) a single zig-zag function linking these deformations. The numerical tests confirm the great accuracy of the hierarchic shell model in reproducing the solid solution with a small number of discrete parameters, provided that the correct warping model is chosen. WI is reliable for all alternating layups. WZ reduces the unknowns to five per surface point, regardless of the number of layers, and is accurate for uniform soft layers.

3.1 Introduction

Laminated composites are obtained by a piling of layers of different materials, or of plies of the same material but with different orientation, as in fiber-reinforced composites. The non-uniform distribution of the material properties over the thickness direction accentuates a certain deformation phenomenology: transverse shear strains become important and the planarity of the deformed section is often lost even for rather slender structures. Each layer may exhibit a different angle of rotation and the final configuration of the deformed cross-section assumes a zig-zag shape, that is a piece-wise linear configuration. Although the application of these materials is now widespread, the development of accurate and affordable analysis and design methods is still an open topic in the scientific community, in particular because the layup configuration influences significantly the modeling rules. The use of a fully 3D model with a finite element discretization through the laminate thickness, despite being the most versatile, requires computational resources usually not affordable in the design stage, especially if non-linear analyses are needed. Often, it is restricted to the analysis of some small portions of interest [63], coupling the analysis with a two-dimensional discretization. Concerning plate/shell models, two main approaches are usually followed: the equivalent single-layer theories (ESL) and the layer-wise theories (LW).

Within the framework of the ESL models, the easiest approach followed in the early studies is the classical Kirchhoff-Love theory of the plates. Based on the assumptions of neglecting the transverse shear effects, this proved to be reliable only for very slender structures. Moreover, it was employed mainly for analytical solutions for simple geometries, due to the C^1 continuity requirement of the weak form, until the spread of spline-based (e.g. [59, 67, 104]) and other novel discretization strategies [118]. Finite elements based on the First Order Shear Deformation Theory (FSDT) are widely used to include the transverse shear deformations and they were the natural progress in modeling composite laminates. However, the hypothesis of cross-sections remaining planar after deformation restricts the capacity of this model, which does not take into account the cross-sectional warping becoming more and more important as the stiffness ratios of the different layers grow. In High Order Shear Deformation Theories (HSDT) the in-plane displacement description is enriched with higher-order terms of the thickness coordinate [112] in order to include warping. However, even in this case, the cross-sectional zig-zag warping affecting some types of laminates is not represented accurately unless many higher-order terms are used, so affecting the computational burden. Halfway between FSDT and HSDT, we can find a recent proposal [43], where the Mindlin-Reissner model is extended with an element-wise displacement fluctuation describing warping and thickness changes, whose associated DOFs can be condensed out to maintain the usual 5 or 6 DOFs per node at the global level. The Zig-zag Theory (ZZT) represents the attempt to take into account the cross-sectional warping keeping the framework of the ESL approaches. In ZZT [21, 15, 24] a piece-wise linear zig-zag-shaped contribution is added to the in-plane displacements employing the first order, or higher order, shear deformation theories *at each layer* and imposing continuity conditions at the interfaces. Compared to the FSDT theory, one unknown for each in-plane direction is added, which represent the amplitude of the zig-zag functions, keeping the number of unknowns independent from the number of layers. Among the ZZTs, the Refined ZZT [41, 27, 52] is one of the most used approaches. Clearly, the accuracy of this approach depends on how well the assigned zig-zag function approximates the actual warping.

The LW theories [113, 31, 134, 44] have a quasi-3D description capability, since the displacement is approximated within each layer. The displacement field is continuous over the thickness but the derivatives with respect to the thickness coordinate are not. This means that the strains are discontinuous at the layer interfaces and there is the possibility for the inter-laminar transverse stresses computed from the constitutive relations to be continuous. Opposite considerations can be made for the in-plane strains and stresses [112]. The main drawback of LW theories is that the number of unknowns depends on the number of layers and can become prohibitive in some applications. Recent advances in LW approaches model each lamina as a Kirchhoff-Love thin shell with a spline-based discretization and a focus on the modeling of damage [8, 109, 2]. In short, the efficiency of a model for composite laminates can be assumed mainly as a function of the number of independent variables. The accuracy, instead, is related to the ability to reproduce the warping over the thickness and, in particular the zig-zag deformation. An important point to take into account is that, although many of the discussed models were developed and validated in the small deformation case, the slenderness of most composite structures is likely to induce large deflections and/or buckling. This means that a geometrically non-linear analysis is usually necessary. There exists a number of large deformation models for composite structures, many of them reusing the small deformation models by means of hierarchic [32] or co-rotational strategies [70]. Besides shell models, it is worth mentioning the solid-shell approach [131, 120, 66], based on a large deformation 3D continuum model with a linear kinematic approximation through-the-thickness and only displacement DOFs. For laminates, homogenized solid-shell models (ESL) equivalent to the first order shear deformation theory are presented in [131]. One element per layer can be also adopted when needed to model the sectional warping (LW). In this last case, the model goes in the direction of the so-called multi-director concept [110, 61]. Multi-layered composite shells made of a number of stiff plies shear-coupled by soft interlayers are a typical case of laminates whose mechanics is dominated by the zig-zag effects. Among many others, typical examples are represented by laminated glass and metal-polymer laminates, i.e. glass or metal plies bonded by polymeric interlayers. Although the soft interlayers have in practice no bending stiffness by themselves, they can restrain the shear-sliding of the stiff plies increasing the overall bending capacity of the laminate [34], which varies [101] between the lower bound of free-sliding stiff plies (layered limit) and the upper-bound of perfectly coupled plies (monolithic limit). The alternating layup induces a specific straining/deformation pattern, which distinguishes them from other composites [70, 53]. In fact, the transverse shear strains tend to concentrate in the soft interlayers, with a nearly constant distribution in the thickness, while they are negligible in the stiff plies. Moreover, although the interlayers are soft, they constrain the relative distance between the surfaces to which they adhere. The consequence is that the stiff layers are all subjected to almost identical rotations with respect with their normals in the initial configuration, while the soft layers undergo independent transverse shear strains. Different plate/shell models have been proposed for alternating layups. A reference paper in the field is [70] where, for the first time, a shell model imposing equal rotation of the stiff layers and independent shear deformations of the soft interlayers was proposed. This is a Mindlin-Reissner model enriched by independent in-plane displacements of the soft layers. The same work implements a locking-free shell finite element with the geometrically non-linear model recovered by the co-rotational approach [30]. The kinematics with independent shear deformations of the soft layers [70] results useful also for including thermal and viscous effects [71] and for modeling more general boundary conditions. Most often, the stiff layers tend to exhibit negligible transverse shear strains. Although limited to small-displacement analyses, the Kirchhoff-Love assumption of neglecting the transverse shear strains in the stiff layers was exploited in [53], with the aim of further reducing the model variables. The C^1 continuity requirement is met with special finite elements. In [32] a hierarchic implementation of the Refined ZZT [41, 27, 52] is proposed, adopting finite elements based on the geometrically exact shell theory of Simo [124], in order to economically describe the behavior of composite laminates undergoing large deformations but small strains by adding only two additional DOFs. A linear finite element approximation of geometry and kinematics is considered in this work. In [102], a non-linear KL model is extended hierarchically with linearized transverse shear components. Two formulations are proposed, using hierarchic rotations or hierarchic displacement to include the transverse shear effects. The basic assumption, confirmed by numerical investigation, is that the transverse shear strains remain small in most simulations involving large deflections. Inspired by this work, a large deformation/small strain Kirchhoff-Love shell model hierarchically enhanced with warping is proposed. The warping displacement is additional with respect to the arbitrarily large displacement of the shell reference surface. Hence, it is purely deformational, i.e. not affected by rigid body motions, and small allowing an additive split of the strain into the non-linear part of the basic Kirchhoff-Love model and a linear part of the additional warping deformation. The resulting model is geometrically exact, in the sense that the overall strain measure is not influenced by arbitrarily large rigid motions. Warping is described as combination of a number of through-the-thickness shape functions, generically selected by the user. Two unknowns are introduced for each warping shape, representing its amplitudes in two directions tangent to the shell surface. The plane stress condition is exploited as usual. In the framework of the isogeometric analysis, NURBS basis functions are used to approximate reference surface displacement and warping amplitudes, in order to meet the continuity requirement of the weak form. The transverse shear strains depend only on the warping amplitudes. They are linear with the corresponding DOFs and naturally free from locking. Membrane locking is avoided by a proper choice of the basis functions degree and the adoption of an efficient patch-wise reduced integration scheme for the strain energy associated to the in-plane strain components, the only integration to be repeated in the non-linear analysis. Particular focus is given to the modeling of composite plates and shells with alternating stiff/soft layups, for which two warping models are investigated. The first one assumes that all stiff layers maintain the same director orthogonal to the deformed surface with independent transverse shear deformations of the soft layers. This can be considered as an exact geometry, Total-Lagrangian, rotation-free, higher order version of the proposal in [70], that exploits the negligible transverse shear deformations of the stiff layers to reduce the number of variables per surface point. A second model uses a single zig-zag function linking the transverse shear deformations of the soft layers to further reduce the variables to five per surface point, regardless of the number of layers. A set of numerical tests is reported to assess the validity of the hierarchic formulation and the coarse-mesh accuracy of the discretization. In addition, a critical evaluation of the reliability of the two warping models compared to the solid solution is carried out, showing in which cases one model is preferable to the other.

The chapter is organized as follows. After a brief introduction to the Kirchhoff-Love shell model, Section 2 formulates the Kirchhoff-Love model hierarchically enhanced with generic warping functions in a large deformation/small strain context. Warping models for laminates with alternating stiff/soft layups are presented in Section 3. Details concerning the isogeometric discretization and the non-linear analysis are reported in Section 4. Section 5 contains a significant set of numerical tests. A concluding summary is given in Section 6.

3.2 Hierarchic Kirchhoff-Love shell model with warping

3.2.1 Standard Kirchhoff-Love shell

A set of convective coordinates ξ^α, with $\alpha = 1, 2$ is considered over a suitable reference shell surface (not necessarily being the middle surface of the shell), while in the thickness direction the coordinate $\xi^3 \in [\xi^3_b, \xi^3_t]$ is assumed with ξ^3_b and ξ^3_t identifying the offset of bottom and top surfaces of the body with respect to the reference one. In order to introduce the notation, from now on the Greek indices α, β will be assumed to take the values $1, 2$, while the Latin indices i, j, k will vary between 1 and 3.
The position of a point in the undeformed configuration is defined by the position vector $\mathbf{X}$

$$\mathbf{X} = \mathbf{R}(\xi^1, \xi^2) + \xi^3 \mathbf{A}_3(\xi^1, \xi^2) \tag{3.1}$$

where $\mathbf{R}(\xi^1, \xi^2)$ represents the position of the corresponding point on the reference surface and $\mathbf{A}_3$ the initial shell normal taken as

$$\mathbf{A}_3 = \frac{\mathbf{A}_1 \times \mathbf{A}_2}{|\mathbf{A}_1 \times \mathbf{A}_2|}. \tag{3.2}$$

with vectors

$$\mathbf{A}_\alpha = \frac{\partial \mathbf{R}}{\partial \xi^\alpha}$$

defining a tangent plane to the shell surface. Covariant base vectors $\mathbf{G}_\alpha$ in the reference configuration can be then evaluated as

$$\begin{aligned} \mathbf{G}_\alpha &= \frac{\partial \mathbf{X}}{\partial \xi^\alpha} = \mathbf{A}_\alpha + \xi^3 \mathbf{A}_{3,\alpha} \\ \mathbf{G}_3 &= \frac{\partial \mathbf{X}}{\partial \xi^3} = \mathbf{A}_3 \end{aligned} \tag{3.3}$$

The current deformed configuration is described as

$$\mathbf{x} = \mathbf{r}(\xi^1, \xi^2) + \xi^3 \mathbf{a}_3(\xi^1, \xi^2) \tag{3.4}$$

where $\mathbf{r} = \mathbf{R} + \mathbf{v}$ is the current position of the reference surface, with $\mathbf{v}$ its displacement. Introducing the reference surface covariant basis vectors in the deformed configuration

$$\mathbf{a}_\alpha = \frac{\partial \mathbf{r}}{\partial \xi_\alpha} = \mathbf{A}_\alpha + \mathbf{v}_{,\alpha}$$

the current normal is defined as

$$\mathbf{a}_3 = \frac{\mathbf{a}_1 \times \mathbf{a}_2}{|\mathbf{a}_1 \times \mathbf{a}_2|}, \tag{3.5}$$

according to the Kirchhoff-Love shell assumption that the director remains straight and normal to the shell surface during deformation. The covariant basis vectors in the deformed configuration can be computed over the body as

$$\begin{aligned} \mathbf{g}_\alpha &= \frac{\partial \mathbf{x}}{\partial \xi^\alpha} = \mathbf{a}_\alpha + \xi^3 \mathbf{a}_{3,\alpha} \qquad \text{with} \\ \mathbf{g}_3 &= \frac{\partial \mathbf{x}}{\partial \xi^3} = \mathbf{a}_3(\xi^1, \xi^2) \end{aligned} \tag{3.6}$$

Denoting the displacement of the body with

$$\mathbf{u}^{KL} = \mathbf{x} - \mathbf{X} = \mathbf{v}(\xi^1, \xi^2) + \xi^3(\mathbf{a}_3(\xi^1, \xi^2) - \mathbf{A}_3(\xi^1, \xi^2)) \tag{3.7}$$

the Green-Lagrange strain tensor can be written as

$$\mathbf{E} = \sum_{i,j=1}^{3} \bar{E}_{ij} \mathbf{G}^i \otimes \mathbf{G}^j \quad \text{with} \quad \bar{E}_{ij} = \frac{1}{2}\left(\mathbf{g}_i \cdot \mathbf{g}_j - \mathbf{G}_i \cdot \mathbf{G}_j\right) = \frac{1}{2}\left(\mathbf{u},_i^{KL} \cdot \mathbf{G}_j + \mathbf{u},_j^{KL} \cdot \mathbf{G}_i + \mathbf{u},_i^{KL} \cdot \mathbf{u},_j^{KL}\right) \tag{3.8}$$

where $\bar{E}_{ij}$ are the covariant strain components. The partial derivatives of the displacement vector are

$$\begin{aligned} \mathbf{u},_\alpha^{KL} &= \mathbf{v},_\alpha + \xi^3(\mathbf{a}_3,_\alpha - \mathbf{A}_3,_\alpha) \qquad \text{with} \\ \mathbf{u},_3^{KL} &= \mathbf{a}_3(\xi^1, \xi^2) - \mathbf{A}_3(\xi^1, \xi^2) \end{aligned} \tag{3.9}$$

The reference surface and body contravariant basis vectors are obtained from the dual basis condition $\mathbf{a}_\alpha \cdot \mathbf{a}^\beta = \mathbf{A}_\alpha \cdot \mathbf{A}^\beta = \delta_\alpha^\beta$ and $\mathbf{g}_\alpha \cdot \mathbf{g}^\beta = \mathbf{G}_\alpha \cdot \mathbf{G}^\beta = \delta_\alpha^\beta$. Due to Eq. (3.2) and (3.5), the transverse shear strains vanish, that is $\bar{E}_{\alpha 3} = 0$. The same holds for the thickness strain, i.e. $\bar{E}_{33} = 0$. Assuming its components to vary linearly through the thickness, it is possible to separate the strain into a constant part due to membrane action and a linear part due to bending. The covariant strain coefficients are:

$$\bar{E}_{\alpha\beta} = \bar{e}_{\alpha\beta} + \xi^3 \bar{\chi}_{\alpha\beta} = \frac{1}{2}(a_{\alpha\beta} - A_{\alpha\beta}) + \xi^3(B_{\alpha\beta} - b_{\alpha\beta}) \tag{3.10}$$

with the metric coefficients $a_{\alpha\beta} = \mathbf{a}_\alpha \cdot \mathbf{a}_\beta$ and $A_{\alpha\beta} = \mathbf{A}_\alpha \cdot \mathbf{A}_\beta$. The curvature tensor coefficients [48] are defined as

$$\begin{aligned} B_{\alpha\beta} &= -\frac{1}{2}(\mathbf{A}_\alpha \cdot \mathbf{A}_{3,j} + \mathbf{A}_\beta \cdot \mathbf{A}_{3,\alpha}) = \mathbf{A}_{\alpha,\beta} \cdot \mathbf{A}_3 \\ b_{\alpha\beta} &= -\frac{1}{2}(\mathbf{a}_\alpha \cdot \mathbf{a}_{3,j} + \mathbf{a}_\beta \cdot \mathbf{a}_{3,\alpha}) = \mathbf{a}_{\alpha,\beta} \cdot \mathbf{a}_3 \end{aligned} \tag{3.11}$$

The curvature components for the Kirchhoff-Love shell can be then computed as

$$\bar{\chi}_{\alpha\beta} = B_{\alpha\beta} - b_{\alpha\beta} = \mathbf{A}_{\alpha,\beta} \cdot \mathbf{A}_3 - \mathbf{a}_{\alpha,\beta} \cdot \mathbf{a}_3 \quad \text{with}$$

The presence of the norm $|\mathbf{a}_1 \times \mathbf{a}_2|$ in the denominator of $\mathbf{a}_3$ leads to a rather complicated expression of the curvature in terms of the displacement field and, then, a computationally expensive evaluation of the discrete operators coming from the strain variations. A simplified formula for the curvature proposed in [67] is here adopted, exploiting the hypothesis of large deformations but small membrane strains. It is based on the following simplification in Eq. (3.5):

$$|\mathbf{a}_1 \times \mathbf{a}_2| \approx |\mathbf{A}_1 \times \mathbf{A}_2|.$$

Consequently, $b_{\alpha\beta}$ is simplified as

$$b_{\alpha\beta} \approx \mathbf{a}_{\alpha,\beta} \cdot \frac{\mathbf{a}_1 \times \mathbf{a}_2}{|\mathbf{A}_1 \times \mathbf{A}_2|}.$$

and the curvature components reduce to

$$\bar{\chi}_{\alpha\beta} = B_{\alpha\beta} - b_{\alpha\beta} \approx \frac{1}{|\mathbf{A}_1 \times \mathbf{A}_2|}(\mathbf{A}_{\alpha,\beta} \cdot (\mathbf{A}_1 \times \mathbf{A}_2) - \mathbf{a}_{\alpha,\beta} \cdot (\mathbf{a}_1 \times \mathbf{a}_2)) \tag{3.12}$$

that is a third order dependence on the displacement. The in-plane strain components of the KL model can be written in Voigt's notation as

$$\bar{\boldsymbol{\varepsilon}}_p = \bar{\mathbf{e}} + \xi^3 \bar{\boldsymbol{\chi}} \quad \text{with} \quad \bar{\boldsymbol{\varepsilon}}_p = \begin{bmatrix} \bar{E}_{11} \\ \bar{E}_{22} \\ 2\bar{E}_{12} \end{bmatrix}, \quad \bar{\mathbf{e}} = \begin{bmatrix} \bar{e}_{11} \\ \bar{e}_{22} \\ 2\bar{e}_{12} \end{bmatrix}, \quad \bar{\boldsymbol{\chi}} = \begin{bmatrix} \bar{\chi}_{11} \\ \bar{\chi}_{22} \\ 2\bar{\chi}_{12} \end{bmatrix}. \tag{3.13}$$

3.2.2 Hierarchic shell model with warping

Multiple warping deformations, assumed to be small, can be hierarchically added to the KL shell kinematics. Let us consider the case of an overall warping profile expressed as a combination of n shapes $w_k(\xi^3)$. The current configuration is defined as:

$$\mathbf{x} = \mathbf{r}(\xi^1, \xi^2) + \xi^3 \mathbf{a}_3(\xi^1, \xi^2) + \sum_{k=1}^{n} \sum_{\beta=1}^{2} \mu_{\beta k}(\xi^1, \xi^2) w_k(\xi^3) \mathbf{a}_\beta(\xi_1, \xi_2) \tag{3.14}$$

where $\mu_{\beta k}(\xi^1, \xi^2)$ represents the amplitude of the kth warping shape directed along the surface tangent vectors $\mathbf{a}_\beta$ with $\beta = 1, 2$ respectively. The profile is assumed to be approximated by the same shapes (with different amplitudes) along the 2 directions, as typical for example for composites made of isotropic layers, also if the generalization to different shapes could be considered for generic composites [32]. The covariant base vectors are defined as:

$$\begin{aligned} \mathbf{g}_\alpha &= \frac{\partial \mathbf{x}}{\partial \xi^\alpha} = \mathbf{a}_\alpha + \xi^3 \mathbf{a}_{3,\alpha} + \sum_{k=1}^{n} \sum_{\beta=1}^{2} \left(\mu_{\beta k}(\xi^1, \xi^2) w_k(\xi^3) \mathbf{a}_{\beta,\alpha} + \mu_{\beta k,\alpha} w_k(\xi^3) \mathbf{a}_\beta \right), \quad \alpha = 1, 2 \\ \mathbf{g}_3 &= \frac{\partial \mathbf{x}}{\partial \xi^3} = \mathbf{a}_3(\xi^1, \xi^2) + \sum_{k=1}^{n} \sum_{\beta=1}^{2} \mu_{\beta k} w_{k,3} \mathbf{a}_\beta(\xi_1, \xi_2) \end{aligned} \tag{3.15}$$

Using (3.14) and (3.1), the displacement field assumes the expression:

$$\mathbf{u} = \mathbf{x} - \mathbf{X} = \underbrace{\mathbf{v}(\xi^1, \xi^2) + \xi^3(\mathbf{a}_3(\xi^1, \xi^2) - \mathbf{A}_3(\xi^1, \xi^2))}_{\mathbf{u}^{KL}} + \underbrace{\sum_{k=1}^{n} \sum_{\beta=1}^{2} \mu_{\beta k} w_k(\xi^3) \mathbf{a}_\beta(\xi_1, \xi_2)}_{\mathbf{u}^Z} \tag{3.16}$$

where $\mathbf{u}^{KL}$ represents the displacement coming from the KL model and $\mathbf{u}^Z$ is the contribution given by warping. Analogously, the derivatives of the displacements can be expressed as the sum of the KL and warping contributions:

$$\begin{aligned} \mathbf{u}_{,\alpha} &= \mathbf{u}_{,\alpha}^{KL} + \mathbf{u}_{,\alpha}^{Z} \quad \text{with} \quad \mathbf{u}_{,\alpha}^{Z} = \sum_{k=1}^{n} \sum_{\beta=1}^{2} (\mu_{\beta k} \mathbf{a}_{\beta,\alpha} + \mu_{\beta k,\alpha} \mathbf{a}_\beta) w_k, \\ \mathbf{u}_{,3} &= \mathbf{u}_{,3}^{KL} + \mathbf{u}_{,3}^{Z} \quad \text{with} \quad \mathbf{u}_{,3}^{Z} = \sum_{k=1}^{n} \sum_{\beta=1}^{2} \mu_{\beta k} \mathbf{a}_\beta w_{k,3} \end{aligned} \tag{3.17}$$

The covariant strain components can be linearized with respect to the warping amplitudes, collected in vector $\boldsymbol{\mu}$, as

$$\bar{E}_{ij} = \underbrace{\left[\bar{E}_{ij}\right]_{\boldsymbol{\mu}=\mathbf{0}}}_{\bar{E}_{ij}^{KL}} + \underbrace{\left[\frac{\partial \bar{E}_{ij}}{\partial \boldsymbol{\mu}}\right]_{\boldsymbol{\mu}=\mathbf{0}} \cdot \boldsymbol{\mu}}_{\bar{E}_{ij}^{Z}}, \tag{3.18}$$

and, neglecting terms more than linear in ξ^3 and w_α, the additional warping contribution to the strain is

$$
\begin{aligned}
\bar{E}_{11}^{Z} &\approx \mathbf{a}_1 \cdot \mathbf{u},_1^{Z} = \sum_{k=1}^{n}\sum_{\beta=1}^{2}(\mu_{\beta k}\mathbf{a}_1 \cdot \mathbf{a}_{\beta},_1 + \mu_{\beta k},_1 \mathbf{a}_1 \cdot \mathbf{a}_\beta)w_k \\
\bar{E}_{22}^{Z} &\approx \mathbf{a}_2 \cdot \mathbf{u},_2^{Z} = \sum_{k=1}^{n}\sum_{\beta=1}^{2}(\mu_{\beta k}\mathbf{a}_2 \cdot \mathbf{a}_{\beta},_2 + \mu_{\beta k},_2 \mathbf{a}_2 \cdot \mathbf{a}_\beta)w_k \\
2\bar{E}_{12}^{Z} &\approx \mathbf{a}_1 \cdot \mathbf{u},_2^{Z} + \mathbf{a}_2 \cdot \mathbf{u},_1^{Z} = \sum_{k=1}^{n}\sum_{\beta=1}^{2}(\mu_{\beta k}(\mathbf{a}_1 \cdot \mathbf{a}_{\beta},_2 + \mathbf{a}_2 \cdot \mathbf{a}_{\beta},_1) + \mu_{\beta k},_2 \mathbf{a}_1 \cdot \mathbf{a}_\beta + \mu_{\beta k},_1 \mathbf{a}_2 \cdot \mathbf{a}_\beta)w_k \\
2\bar{E}_{13}^{Z} &\approx \mathbf{a}_1 \cdot \mathbf{u},_3^{Z} \cancel{+\mathbf{a}_3 \cdot \mathbf{u},_1^{Z}} = \sum_{k=1}^{n}\sum_{\beta=1}^{2}(\mu_{\beta k}\mathbf{a}_1 \cdot \mathbf{a}_\beta)w_k,_3 + \cancel{\sum_{k=1}^{n}\sum_{\beta=1}^{2}(\mu_{\beta k}\mathbf{a}_3 \cdot \mathbf{a}_{\beta},_1)w_k} \\
2\bar{E}_{23}^{Z} &\approx \mathbf{a}_2 \cdot \mathbf{u},_3^{Z} \cancel{+\mathbf{a}_3 \cdot \mathbf{u},_2^{Z}} = \sum_{k=1}^{n}\sum_{\beta=1}^{2}(\mu_{\beta k}\mathbf{a}_2 \cdot \mathbf{a}_\beta)w_k,_3 + \cancel{\sum_{k=1}^{n}\sum_{\beta=1}^{2}(\mu_{\beta k}\mathbf{a}_3 \cdot \mathbf{a}_{\beta},_2)w_k} \\
\bar{E}_{33}^{Z} &\approx 0
\end{aligned}
\tag{3.19}
$$

It is worth noting that the warping displacement produces also transverse shear strains unlike the standard KL kinematics. In such strain components the part coming from $\mathbf{u},_1^{Z}$ and $\mathbf{u},_2^{Z}$ are canceled in order to avoid terms in w_k considered of higher order compared to $w_k,_3$. For example, a w_k that is piece-wise linear through the thickness is associated with piece-wise constant transverse shear strains, while their linear variation is neglected. This is analogous to the Reissner-Mindlin shell, where only constant transverse shear strains are associated to the rigid (linear) section kinematics.

A more compact notation, useful for the subsequent developments, is obtained by collecting the in-plane warping strains as

$$
\begin{aligned}
\bar{\boldsymbol{\varepsilon}}_p^{z} &= \begin{bmatrix} \bar{E}_{11}^{z} \\ \bar{E}_{22}^{z} \\ \bar{E}_{12}^{z} \end{bmatrix} = \sum_{k=1}^{n} \bar{\boldsymbol{\psi}}_k w_k \\
\bar{\boldsymbol{\psi}}_k &= \sum_{\beta=1}^{2} \begin{bmatrix} \mu_{\beta k}\mathbf{a}_1 \cdot \mathbf{a}_{\beta},_1 + \mu_{\beta k},_1 \mathbf{a}_1 \cdot \mathbf{a}_\beta \\ \mu_{\beta k}\mathbf{a}_2 \cdot \mathbf{a}_{\beta},_2 + \mu_{\beta k},_2 \mathbf{a}_2 \cdot \mathbf{a}_\beta \\ \mu_{\beta k}(\mathbf{a}_1 \cdot \mathbf{a}_{\beta},_2 + \mathbf{a}_2 \cdot \mathbf{a}_{\beta},_1) + \mu_{\beta k},_2 \mathbf{a}_1 \cdot \mathbf{a}_\beta + \mu_{\beta k},_1 \mathbf{a}_2 \cdot \mathbf{a}_\beta \end{bmatrix}
\end{aligned}
\tag{3.20}
$$

and the transverse shear ones as

$$
\bar{\boldsymbol{\varepsilon}}_t^{z} = \begin{bmatrix} 2\bar{E}_{13}^{z} \\ 2\bar{E}_{23}^{z} \end{bmatrix} = \sum_{k=1}^{n} \bar{\boldsymbol{\gamma}}_k w_k,_3 \quad \text{with} \quad \bar{\boldsymbol{\gamma}}_k = \sum_{\beta=1}^{2} \begin{bmatrix} \mu_{\beta k}\mathbf{a}_1 \cdot \mathbf{a}_\beta \\ \mu_{\beta k}\mathbf{a}_2 \cdot \mathbf{a}_\beta \end{bmatrix}. \tag{3.21}
$$

Under the condition of large deformations but small strains, it is possible to simplify the generalized strains $\bar{\boldsymbol{\psi}}_k$ and $\bar{\boldsymbol{\gamma}}_k$ by assuming in Eq. (3.20) and Eq. (3.21) $\mathbf{a}_\alpha \cdot \mathbf{a}_\beta \approx \mathbf{A}_\alpha \cdot \mathbf{A}_\beta$, $\mathbf{a}_\alpha \cdot \mathbf{a}_{\beta},_1 \approx \mathbf{A}_\alpha \cdot \mathbf{A}_{\beta},_1$ and $\mathbf{a}_\alpha \cdot \mathbf{a}_{\beta},_2 \approx \mathbf{A}_\alpha \cdot \mathbf{A}_{\beta},_2$, so that they become independent from the displacement of the reference surface:

$$
\begin{aligned}
\bar{\boldsymbol{\psi}}_k &\approx \sum_{\beta=1}^{2} \begin{bmatrix} \mu_{\beta k}\mathbf{A}_1 \cdot \mathbf{A}_{\beta},_1 + \mu_{\beta k},_1 \mathbf{A}_1 \cdot \mathbf{A}_\beta \\ \mu_{\beta k}\mathbf{A}_2 \cdot \mathbf{A}_{\beta},_2 + \mu_{\beta k},_2 \mathbf{A}_2 \cdot \mathbf{A}_\beta \\ \mu_{\beta k}(\mathbf{A}_1 \cdot \mathbf{A}_{\beta},_2 + \mathbf{A}_2 \cdot \mathbf{A}_{\beta},_1) + \mu_{\beta k},_2 \mathbf{A}_1 \cdot \mathbf{A}_\beta + \mu_{\beta k},_1 \mathbf{A}_2 \cdot \mathbf{A}_\beta \end{bmatrix} \\
\bar{\boldsymbol{\gamma}}_k &\approx \sum_{\beta=1}^{2} \begin{bmatrix} \mu_{\beta k}\mathbf{A}_1 \cdot \mathbf{A}_\beta \\ \mu_{\beta k}\mathbf{A}_2 \cdot \mathbf{A}_\beta \end{bmatrix}.
\end{aligned}
\tag{3.22}
$$

We can note that, in the simplified form, the generalized strains defined in the previous equation are linear in the warping amplitudes and their derivatives. Moreover, the generalized transverse shear strains depends only on the warping amplitudes, so that, the discrete version of model will be automatically free from transverse shear locking. From this point of view, the proposed model can be seen as a generalization of the one proposed in [102] for shear-deformable shells, that can be recovered by selecting the warping profile as a linear function of the thickness coordinate (plane section hypothesis).

3.2.3 Remarks on the geometrical exactness of the hierarchic shell

It is worth noting that the large deformation/small strain hierarchic shell model formulated above is geometrically exact, a term commonly used to mean that the strain measure is not affected by rigid body motions of arbitrary magnitude and, then, by changes of observer. This fact is easy to prove and is inherent in the hierarchical theory. Indeed, rigid motions are described in terms of displacement of the shell reference surface only. This means that they do not contribute to the warping part of the strain, as clear also by looking at Eq. (3.22), and the warping displacement is purely deformational. The additive split of the total Green-Lagrange strain in Eq. (3.18) into warping part and basic Kirchhoff-Love geometrically exact part makes the proof of invariance of the total strain under superposition of rigid motions trivial.

3.2.4 From covariant to local Cartesian strain components

The total covariant strain components collected in Voigt notation can be written as

$$\bar{\boldsymbol{\varepsilon}}_p = \bar{\mathbf{e}} + \xi^3 \bar{\boldsymbol{\chi}} + \sum_{k=1}^{n} \bar{\boldsymbol{\psi}}_k w_k \qquad \bar{\boldsymbol{\varepsilon}}_t = \sum_{k=1}^{n} \bar{\boldsymbol{\gamma}}_k w_{k,3} \tag{3.23}$$

where the transverse shear ones coincide with the warping contribution. In order to impose the constitutive law, it is convenient to express the strain components in a local Cartesian coordinate system whose $x-y$ plane is tangent to the shell reference surface. For a general 3D continuum, this transformation is reported, for instance, in [131, 66]. The simplification of this transformation accounting for the Kirchhoff-Love shell hypothesis and neglecting its variation through the thickness furnishes the sought relationship:

$$\begin{aligned} \boldsymbol{\varepsilon}_p =& \mathbf{T}_p \bar{\boldsymbol{\varepsilon}}_p \quad \text{with} \quad \mathbf{T}_p = \begin{bmatrix} x_\xi^2 & x_\eta^2 & 2x_\xi x_\eta \\ y_\xi^2 & y_\eta^2 & 2y_\xi y_\eta \\ x_\xi y_\xi & x_\eta y_\eta & x_\xi y_\eta + x_\eta y_\xi \end{bmatrix}^{-T} \\ \boldsymbol{\varepsilon}_t =& \mathbf{T}_t \bar{\boldsymbol{\varepsilon}}_t \quad \text{with} \quad \mathbf{T}_t = \begin{bmatrix} x_\xi & x_\eta \\ y_\xi & y_\eta \end{bmatrix}^{-T} . \end{aligned} \tag{3.24}$$

The coefficients of the transformation matrices are $x_\xi = \mathbf{i}_1 \cdot \mathbf{A}_1$, $y_\xi = \mathbf{i}_2 \cdot \mathbf{A}_1$, $x_\eta = \mathbf{i}_1 \cdot \mathbf{A}_2$, $y_\eta = \mathbf{i}_1 \cdot \mathbf{A}_2$ with $\mathbf{i}_1$ and $\mathbf{i}_2$ the unit vectors along the axis of the local Cartesian coordinates where the material properties are defined.

3.2.5 Pre-integration of the elasticity matrices

For a linear elastic material, e.g. isotropic, the constitutive matrices linking stress and strain are

$$\mathbf{C}_p = \frac{E}{1-\nu^2} \begin{bmatrix} 1 & \nu & 0 \\ \nu & 1 & 0 \\ 0 & 0 & (1-\nu)/2 \end{bmatrix} \qquad \mathbf{C}_t = \begin{bmatrix} G & 0 \\ 0 & G \end{bmatrix} \tag{3.25}$$

where $\mathbf{C}_p$ is the plane stress matrix and $\mathbf{C}_t$ is a diagonal matrix made with the shear modulus of the material. Collecting the local Cartesian generalized in-plane and transverse strains in vectors

$$\boldsymbol{\varepsilon}_P = \begin{bmatrix} \mathbf{e} \\ \boldsymbol{\chi} \\ \boldsymbol{\psi}_1 \\ \vdots \\ \boldsymbol{\psi}_n \end{bmatrix} \qquad \boldsymbol{\varepsilon}_T = \begin{bmatrix} \boldsymbol{\gamma}_1 \\ \vdots \\ \boldsymbol{\gamma}_n \end{bmatrix} \tag{3.26}$$

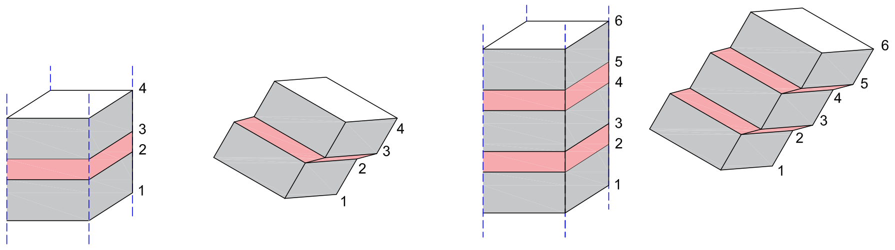

3 layers

5 layers

Figure 3.1: Kinematics of laminates with alternating stiff/soft layers.

obtained from the covariant ones through Eq. (3.24), the equivalence of strain energy per unit of reference surface

$$W = \frac{1}{2}\int_{\xi_b^3}^{\xi_t^3} (\boldsymbol{\varepsilon}_p^T \mathbf{C}_p \boldsymbol{\varepsilon}_p + \boldsymbol{\varepsilon}_t^T \mathbf{C}_t \boldsymbol{\varepsilon}_t) d\xi^3 = \frac{1}{2}(\boldsymbol{\varepsilon}_P^T \mathbf{D}_P \boldsymbol{\varepsilon}_P + \boldsymbol{\varepsilon}_T^T \mathbf{D}_T \boldsymbol{\varepsilon}_T) \tag{3.27}$$

provides the generalized constitutive matrices

$$\mathbf{D}_P = \begin{bmatrix} \mathbf{D}_{mm} & \mathbf{D}_{mb} & \mathbf{D}_{mw_1} & \dots & \mathbf{D}_{mw_n} \\ & \mathbf{D}_{bb} & \mathbf{D}_{bw_1} & \dots & \mathbf{D}_{bw_n} \\ & & \mathbf{D}_{w_1 w_1} & \dots & \mathbf{D}_{w_1 w_n} \\ & \text{sym} & & \ddots & \vdots \\ & & & & \mathbf{D}_{w_n w_n} \end{bmatrix} \quad \mathbf{D}_T = \begin{bmatrix} \mathbf{D}_{T11} & \dots & \mathbf{D}_{T1n} \\ & \ddots & \vdots \\ \text{sym} & & \mathbf{D}_{Tnn} \end{bmatrix}$$

where

$$\mathbf{D}_{mm} = \int_{\xi_b^3}^{\xi_t^3} \mathbf{C}_p \qquad \mathbf{D}_{mb} = \int_{\xi_b^3}^{\xi_t^3} \xi^3 \mathbf{C}_p \qquad \mathbf{D}_{mw_k} = \int_{\xi_b^3}^{\xi_t^3} w_k \mathbf{C}_p$$

$$\mathbf{D}_{bb} = \int_{\xi_b^3}^{\xi_t^3} \xi^3 \xi^3 \mathbf{C}_p \qquad \mathbf{D}_{bw_k} = \int_{\xi_b^3}^{\xi_t^3} \xi^3 w_k \mathbf{C}_p \qquad \mathbf{D}_{w_i w_j} = \int_{\xi_b^3}^{\xi_t^3} w_i w_j \mathbf{C}_p$$

$$\mathbf{D}_{Tij} = \int_{\xi_b^3}^{\xi_t^3} w_{i,3}\, w_{j,3}\, \mathbf{C}_t.$$

Each sub-matrix is obtained in the pre-processing stage by integrating over the shell thickness. The integrals are calculated as a discrete sums of contributions of each layer to take into account the change of material properties through the thickness.

3.3 Modeling laminates with alternating layup

In this section, focus is given to possible choices of the warping model for composite shells with alternating stiff/soft layers. Typical examples are polymer-metal composites and glass laminates. In this last case, the stiff parts are glass layers coupled by soft parts usually made of PVB or silicone. When the stiffness of the two material types differ of many orders of magnitude, the hypotheses of plane section remaining plane after deformation becomes unreliable and the solution obtained by the first order plate theory inaccurate, even using shear correction factors. The typical kinematics is depicted in Fig.3.1 for the example case of 3 and 5 layers respectively. Solid models can be used to obtain a reliable solution by discretizing the structure also through the thickness. However, general purpose solid finite elements are not suitable for layered plates because of the high number of DOFs. The KL model hierarchically enhanced by warping can be adopted for a simple and efficient modeling of this class of composites, after a proper selection of the warping profile.

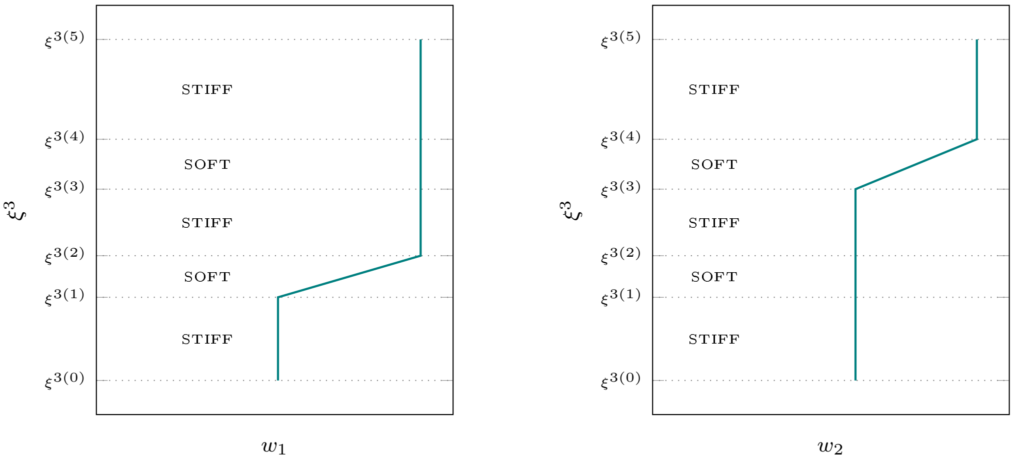

Figure 3.2: Warping functions with independent transverse shear deformations of the soft interlayers (WI) for 5 alternating stiff/soft layers.

3.3.1 Warping profile with independent transverse shear deformations of the soft layers

The alternating layup induces a specific deformation pattern, which distinguishes them from other composites [70, 53]. The transverse shear strains tend to concentrate in the soft interlayers, with a nearly constant distribution in the thickness, while they are negligible in the stiff plies. Moreover, although the interlayers are soft, the bonding capacity is such that the stiff layers are all subjected to almost identical rotations with respect with their normals in the undistorted configuration. The warping profile is chosen as proposed for the first time in [70]. In practice, a number of warping profiles equal to the soft interlayers is considered. The generic warping function w_k is defined layer-wise as

$$w_k(\xi^3) = \begin{cases} -1 & \text{if} \quad \xi^3 < \xi^3_{bk} \\ \dfrac{2(\xi^3 - \xi^3_{bk})}{t_k} - 1 & \text{if} \quad \xi^3_{bk} \leq \xi^3 \leq \xi^3_{tk} \\ 1 & \text{if} \quad \xi^3 > \xi^3_{tk} \end{cases} \tag{3.28}$$

where t_k is the thickness of the kth soft layer whose bottom and top interface are located at ξ^3_{bk} and ξ^3_{tk} respectively. For instance, in the case of 3 layers the warping profile at the 4 interfaces of the laminate is $\{-1, -1, 1, 1\}$. In the 5 layers case, the two warping profiles at the 6 interfaces are $\{-1, -1, 1, 1, 1, 1\}$ and $\{-1, -1, -1, -1, 1, 1\}$. A rigid translation is conveniently subtracted from the warping shapes such that $w_k(\xi^3_r) = 0$ for a correct imposition of the boundary conditions on the reference surface corresponding to $\xi^3 = \xi^3_r$. The same profiles, but with independent amplitudes, can be assumed along both the directions defined by the tangent vectors $\mathbf{A}_1$ and $\mathbf{A}_2$. The total number of variables of the model at each point over the shell surface is $n_t = 3 + 2n_s$: 3 components of the reference surface displacement and 2 amplitudes for the warping profile associated to each of the n_s soft layers. For the case of 5 layers, the 2 warping functions are illustrated in Fig. 3.2. Compared to the co-rotational shell model proposed in [70], our proposal is purely Total Lagrangian, i.e. the strain measure accuracy is not affected by the mesh size, and the number of variables is reduced by imposing that all stiff layers maintain the same director orthogonal to the deformed surface.

3.3.2 Warping profile with a single zig-zag shape

The refined ZZT provides a single piecewise linear shape of the warping profile over the whole thickness of the laminate, denoted in following as $w(\xi^3)$, avoiding the subscript k

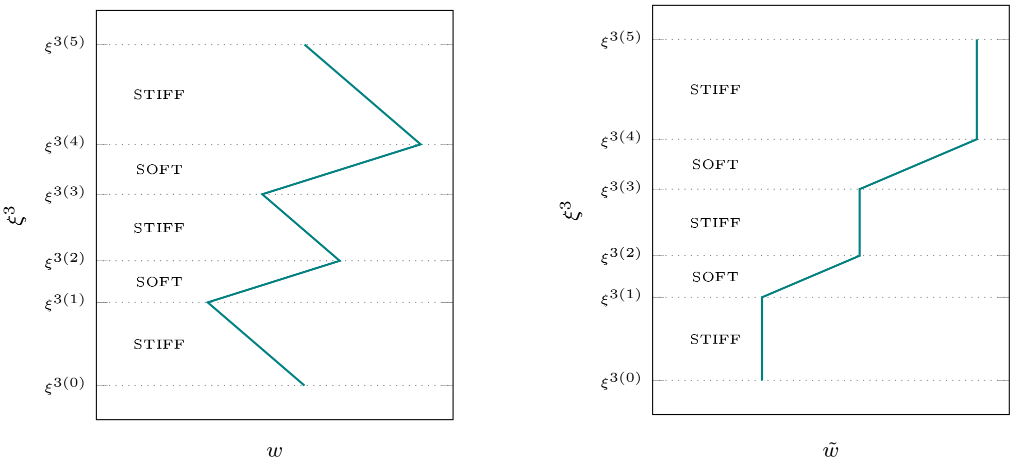

ZZ function

Rotated ZZ function

Figure 3.3: Zig-zag warping function (WZ) for 5 alternating stiff/soft layers: the function coming from the refined ZZT on the left and the function rotated in order to minimize the shear deformation of the stiff layers on the right.

previously used in the case of multiple shapes. According to this theory, the zig-zag function is defined by the $N+1$ interface values $w^{(j)}$, with $j = 0, 1, ...N$ and N the overall number of layers. The theory sets $w(\xi^3)$ to vanish at the top and bottom surfaces of the laminate, i.e. $w^{(0)} = w^{(N)} = 0$. The internal interface values are computed as

$$w^{(j)} = w^{(j-1)} + h^{(j)}\beta^{(j)} \quad \text{with} \quad j = 1, ..., N-1 \tag{3.29}$$

where $h^{(j)}$ is the thickness of the jth layer. $\beta^{(j)}$ is the slope of the zig-zag function in each layer j, and is obtained as

$$\beta^{(j)} = \frac{\bar{G}}{G^{(j)}} - 1 \quad \text{with} \quad j = 1, ..., N \tag{3.30}$$

where $G^{(j)}$ is the shear modulus of the jth layer and $\bar{G}$ denotes a weighted average of G over the laminate thickness, i.e.

$$\bar{G} = \left(\frac{1}{h} \sum_{j=1}^{N} \frac{h^{(j)}}{G^{(j)}} \right)^{-1} \tag{3.31}$$

The complete derivation of these equations can be found in [133]. Let us consider a layup made of 5 alternating stiff/soft layers. As we can observe on the left side of Fig. 3.3, the constraint of vanishing zig-zag function at the top and bottom surfaces produces a profile characterized by non-null slop, and then transverse shear strain, in all layers including the stiff ones.

Instead, it was demonstrated in a number of papers, e.g. in [70], that the transverse shear strains tend to vanish in the stiff layers. This is not an issue when the zig-zag function is used to enhance shear deformable beam and shell models, because the transverse shear strains of the basic models can compensate for the additional part coming from the zig-zag function, so recovering the Kirchhoff-Love behavior of the stiff layers. The price to pay, in this case, is the need for independent rotational DOFs for describing the section rotation, complicating also the expressions for finite 3D rotations. Instead, if we want to avoid these additional variables and to keep using the proposed Kirchhoff-Love model hierarchically enhanced with warping, it is necessary to modify the zig-zag function in such a way as to minimize the slop of the zig-zag function in the stiff layer. We propose a formula to rotate the zig-zag shape. Starting from the one obtained with the formulas above, the rotated zig-zag function $\tilde{w}$ is obtained as

$$\tilde{w}(\xi^3) = w(\xi^3) - \varphi\xi^3 \quad \text{with} \quad \varphi = \frac{\sum_{j=1}^{N} G^{(j)} h^{(j)} \beta^{(j)}}{\sum_{j=1}^{N} G^{(j)} h^{(j)}} \tag{3.32}$$

where φ represents a weighted average of the zig-zag function slop over the laminate thickness, in order to concentrate the transverse shear deformation in the soft layers only. Finally, a rigid displacement, e.g. the value of $\tilde{w}(\xi^3)$ at the reference shell surface, can be also subtracted to $\tilde{w}$ for an easy imposition of the support boundary condition. The rotated zig-zag function is illustrated on the right side of Fig. 3.3 for a layup with 5 alternating stiff/soft layers. The resulting shell model is accurate also when the zig-zag effects become important, although based on just 5 DOFs per reference surface point, i.e. 3 displacements and the 2 amplitudes of $\tilde{w}$ along the two directions identified by the tangent vectors $\mathbf{A}_1$ and $\mathbf{A}_2$, regardless of the number of layers. In the limit case of stiffness ratio tending to infinity, the approach is equivalent to the one proposed in [46] for enhancing a linear Euler-Bernoulli beam, where $\tilde{w}(\xi^3)$ is defined as $w(\xi^3) + \xi^3$.

3.4 Effective isogeometric formulation

3.4.1 The isogeometric shell element

Following the isoparametric concept, geometry and displacement field of the reference surface and warping amplitudes are approximated, over each element, as follows

$$\mathbf{X}(\xi,\eta) = \mathbf{N}_u(\xi,\eta)\mathbf{X}_e, \quad \mathbf{u}(\xi,\eta) = \mathbf{N}_u(\xi,\eta)\mathbf{d}_e, \quad \boldsymbol{\mu}(\xi,\eta) = \mathbf{N}_\mu(\xi,\eta)\boldsymbol{\mu}_e \tag{3.33}$$

where $\mathbf{X}_e$, $\mathbf{d}_e$ and $\boldsymbol{\mu}_e$ collect the discrete parameters at the control points of the element associated to geometry, reference surface displacement and warping amplitudes respectively. The matrices $\mathbf{N}_u(\xi,\eta)$ and $\mathbf{N}_\mu(\xi,\eta)$ collect bivariate NURBS functions [51]. Exploiting the isogeometric approximation, the strain components become

$$\boldsymbol{\varepsilon}_P = \boldsymbol{\varepsilon}_P(\mathbf{q}_e) \qquad \boldsymbol{\varepsilon}_T = \boldsymbol{\varepsilon}_T(\mathbf{q}_e) \quad \text{with} \quad \mathbf{q}_e = \begin{bmatrix} \mathbf{d}_e \\ \boldsymbol{\mu}_e \end{bmatrix}. \tag{3.34}$$

3.4.2 Strain energy, discrete operators and equilibrium path

Collecting in vector $\mathbf{q}$ all the DOFs for the approximation of the reference surface displacement and the warping amplitudes over the structure, the overall strain energy can be expressed as a sum of element contributions $\Phi(\mathbf{q}) \equiv \sum_e \Phi_e(\mathbf{q}_e)$, where the element strain energy can be decomposed into in-plane and transverse part as

$$\Phi_e(\mathbf{q}_e) \equiv \Phi_{Pe}(\mathbf{q}_e) + \Phi_{Te}(\mathbf{q}_e) \quad \text{with} \quad \begin{cases} \Phi_{Pe}(\mathbf{q}_e) = \displaystyle\int_{\Omega_e} \left(\frac{1}{2} \boldsymbol{\varepsilon}_P^T \mathbf{D}_P \boldsymbol{\varepsilon}_P \right) d\Omega_e \\ \Phi_{Te}(\mathbf{q}_e) = \displaystyle\int_{\Omega_e} \left(\frac{1}{2} \boldsymbol{\varepsilon}_T^T \mathbf{D}_T \boldsymbol{\varepsilon}_T \right) d\Omega_e \end{cases} \tag{3.35}$$

where Ω_e is the element domain. It is worth highlighting that the model is path-independent for conservative external loads, since it is based on the total elastic potential parametrized in terms of displacement variables. The differentiation of the generalized strains in Eq.(3.34) provides the tangent compatibility operators

$$\mathbf{B}_P(\mathbf{q}_e) = \frac{\partial \boldsymbol{\varepsilon}_P}{\partial \mathbf{q}_e} \qquad \mathbf{B}_T = \frac{\partial \boldsymbol{\varepsilon}_T}{\partial \mathbf{q}_e} \tag{3.36}$$

where $\mathbf{B}_P$ is a function of the discrete DOFs, while $\mathbf{B}_T$ is constant considering the simplified strain expression in Eq. (3.22). The internal force vector of the element can be then evaluated as

$$\mathbf{s}_e(\mathbf{q}_e) \equiv \frac{\partial \Phi_e}{\partial \mathbf{q}_e} = \mathbf{s}_{Pe}(\mathbf{q}_e) + \mathbf{K}_{Te}\mathbf{q}_e \quad \text{with} \quad \begin{cases} \mathbf{s}_{Pe}(\mathbf{q}_e) = \displaystyle\int_{\Omega_e} \left(\mathbf{B}_P(\mathbf{q}_e)^T \mathbf{D}_P \boldsymbol{\varepsilon}_P(\mathbf{q}_e)\right) d\Omega_e \\ \mathbf{K}_{Te} = \displaystyle\int_{\Omega_e} \left(\mathbf{B}_T^T \mathbf{D}_T \mathbf{B}_T\right) d\Omega_e \end{cases} \tag{3.37}$$

where $\mathbf{s}_{eT}(\mathbf{q}_e)$ is the contribution to the element internal forces due to the in-plane strains and $\mathbf{K}_{Te}$ is the constant element stiffness matrix associated to the transverse shear strains. A further differentiation provides the element tangent stiffness matrix as

$$\mathbf{K}_e(\mathbf{q}_e) \equiv \frac{\partial \mathbf{s}_e}{\partial \mathbf{q}_e} = \mathbf{K}_{Pe}(\mathbf{q}_e) + \mathbf{K}_{Te} \tag{3.38}$$

where

$$\mathbf{K}_{Pe}(\mathbf{q}_e) = \int_{\Omega_e} \left(\mathbf{B}_P(\mathbf{q}_e)^T \mathbf{D}_P \mathbf{B}_P(\mathbf{q}_e) + \mathbf{G}(\mathbf{q}_e, \boldsymbol{\sigma}_P(\mathbf{q}_e))\right) d\Omega_e \quad \text{with} \quad \boldsymbol{\sigma}_P(\mathbf{q}_e) = \mathbf{D}_P \boldsymbol{\varepsilon}_P(\mathbf{q}_e) \tag{3.39}$$

and the geometric contribution $\mathbf{G}$ is defined as

$$\mathbf{G}(\mathbf{q}_e, \boldsymbol{\sigma}(\mathbf{q}_e)) = \sum_{k=1}^{6} \sigma_{Pk} \boldsymbol{\Psi}_k(\mathbf{q}_e) \quad \text{with} \quad \boldsymbol{\Psi}_k(\mathbf{q}_e) = \frac{\partial^2 \varepsilon_{Pk}}{\partial \mathbf{q}_e^2} \tag{3.40}$$

since only the first six components of $\boldsymbol{\sigma}_P$, i.e. membrane strains and curvatures, are non-linear in the discrete DOFs.

The equilibrium of slender elastic structures subject to conservative loads amplified by a proportionality factor λ is expressed by the discrete version of the virtual work equation:

$$\mathbf{r}(\mathbf{q}, \lambda) \equiv \mathbf{s}(\mathbf{q}) - \lambda \mathbf{f} = \mathbf{0}, \tag{3.41}$$

where $\mathbf{r} : \mathbb{R}^{N+1} \to \mathbb{R}^N$ is a non-linear vectorial function of the vector $\{\mathbf{q}, \lambda\} \in \mathbb{R}^{N+1}$, collecting the configuration $\mathbf{q} \in \mathbb{R}^N$ and the load multiplier $\lambda \in \mathbb{R}$, $\mathbf{s}(\mathbf{q})$ is the global internal force vector and $\mathbf{f}$ the reference load vector. Equation (3.41) represents a system of N equations and $N+1$ unknowns and its solutions define the *equilibrium paths* as curves in $\mathbb{R}^{N+1}$. The Riks arc-length method [115] is the general solution strategy to trace these curves in a step-by-step manner from a known initial configuration $\mathbf{q}_0$ corresponding to $\lambda = 0$. At each step some Newton iterations are needed to solve (3.41), with the Jacobian involving the global tangent stiffness matrix, obtained by assembling the element ones in Eq. (4.16). Load-controlled and displacement-controlled schemes are recovered as a particular choice of Riks constraint surface [83].

3.4.3 Remarks on the iterative solution

Robustness and efficiency of the iterative solution is achieved by using the mixed integration point (MIP) strategy [83, 79], particularly suitable for the considered problem. It was already demonstrated in many works (see e.g. ([83, 85, 79, 106]) that the MIP Newton method definitely solves the convergence issues of displacement-based formulations in large deformation problems, guarantying the same robustness (very large steps with a few iterations) as that observed in mixed/hybrid finite element formulations [131, 141] for solids, shells and beams. For the basic Kirchhoff-Love model, the excellent iterative performances are demonstrated in [67]. Since, the new shell model proposed in this work in an enrichment of the Kirchhoff-Love one where the additional displacement and strain are linear in the warping DOFs, i.e. not affecting the model non-linearity, the proposal is characterized by an identical iterative behavior as that reported in [67]. The incremental-iterative procedure used for the numerical tests follows exactly that detailed in [40] based on MIP method and adaptive step size.

3.4.4 Locking, NURBS selection and patch-wise selective reduced integration

It is worth noting that the transverse shear strains are linear functions of the warping amplitudes (no derivatives) only. This means that they are naturally free from locking and, then, the associated stiffness matrix $\mathbf{K}_{Te}$ can be evaluated, only once since independent from $\mathbf{q}$, by a full numerical integration. Instead, the in-plane strains are affected by membrane locking as in the standard KL model, also for initially flat plates undergoing finite deformations. To avoid such an undesired inaccuracy one could use NURBS with a very high order, but this would compromise the efficiency due to the reduced sparsity and the greater number of integration points. Instead we propose a selective reduced integration for the internal forces $\mathbf{s}_{Pe}$ and tangent stiffness $\mathbf{K}_{Pe}$ associated to the in-plane strains. Among all possible schemes, we adopt the patch-wise reduced integration named S_0^3 (notation according to [1]) that was identified in [67] as the best solution to avoid locking with cubic NURBS basis functions with C^2 continuity for the standard KL model without spurious modes. The notation means that points and weights are defined over the patch in order to integrate exactly functions of order 3 and C^0 continuity. The corresponding points and weights depend on the knot vector (mesh) and can be found using the algorithm provided in [54], that is simple and inexpensive. Beside the locking issue, the scheme S_0^3 is very efficient because of the very small number of integration points, asymptotically about 1.5×1.5 points per cubic element. Number and position of the points is not equal in each element, but they are distributed over the patch to take into account the inter-element high continuity. Concerning the number of discrete DOFs, it is worth noting that C^2 cubic NURBS are based on $(n_{e1} + 3) \times (n_{e2} + 3)$ control points, where n_{e1} and n_{e2} are the number of elements in the two parametric directions, i.e. asymptotically one control point per element. This is a great advantage over high order Lagrangian finite elements.

3.5 Numerical tests

The proposed isogeometric Kirchhoff-Love model hierarchically enhanced with warping profiles is tested in a sample of numerical experiments concerning both plane and curved structures undergoing buckling and large deflections. The two warping models described in Section 3.3 are employed. Comparisons are made between the models below.

- KL: Basic Kirchhoff-Love shell model without warping;
- KLWI: Hierarchic Kirchhoff-Love shell model with the warping model of Section 3.3.1 based on independent shear deformations of the soft layers;
- KLWZ: Hierarchic Kirchhoff-Love shell model with the warping model of Section 3.3.2 based on a single zig-zag function;
- Abaqus shell: Mindlin-Reissner shell model (FSDT) of Abaqus with shear correction factors;
- Abaqus solid: fully solid model of Abaqus with through-the-thickness discretization assumed as reference solution.

The basic KL can be recovered by constraining the warping amplitudes of KLWI and KLWZ to vanish all over the domain.

The layups illustrated in Fig. 3.4 are considered in the simulations.

The elastic parameters of the stiff layers are typical of soda-lime glass, whereas the stiffness of the interlayers may be representative of silicone, polyvinyl butyral and ionoplast SentryGlas. It is worth noting that only a warping function is used in KLWI for 3-layer layups to capture the sliding of the soft layer and this is the same as that of KLWZ for large stiffness ratios of the materials. Therefore, the two models coincides in this case. Instead, they are different for layups with more than 3 layers: KLWI utilizes $3 + 2n_s = 2 + N$ DOFs per surface point with n_s te number of soft layers and N the total number of layers, while

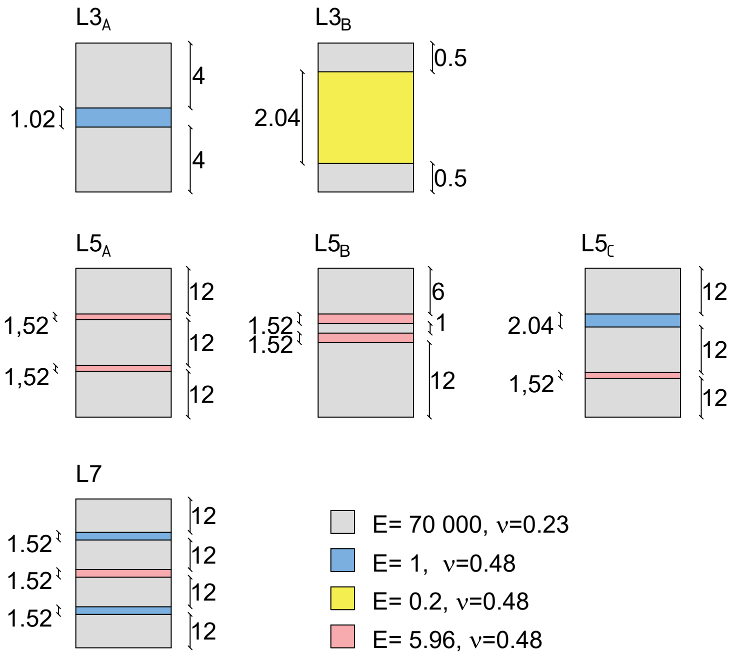

Figure 3.4: Illustration of the layups used in the analyses in terms of number, thickness (mm), Young modulus E (MPa) and Poisson coefficient of the layers.

Layers	KL	Abaqus shell	KLWZ	KLWI	Abaqus solid-shell	Abaqus solid
N	3	5	5	$2+N$	$3(N+1)$	$3(2N+1)$
3	3	5	5	5	12	21
5	3	5	5	7	18	33
7	3	5	5	9	24	45

Table 3.1: Number of unknowns per surface point of the different models.

KLWZ only 5 DOFs regardless of the number of layers. In order to summarize the cost of the different models in terms of unknowns, the corresponding number of DOFs per surface point is reported in Tab. 3.1. It is worth noting that the Abaqus solid solution obtained with quadratic FEs is also quite well reproduced by the Abaqus linear solid-shell FEs (one per layer), that however, still requires many more DOFs than the shell models, including the proposed ones. Besides the number of unknowns, a significant advantage of 2D models is that no numerical integration is required through the thickness, with a further reduction of the number of operations. In addition, a nice feature of the proposals KLWZ and KLWI is that the strain measure is non-linear only in the 3 reference surface displacement DOFs and linear in the others (see Eq. (3.22) and Eq. (4.5)), with a consequent reduced complexity in the computation of internal forces and tangent stiffness matrix compared to 3D models non-linear in all the DOFs. The basic KL is the most efficient choice, but it tends to be largely overstiff for the considered laminates. It is included in the results to quantify how much the section warping affects the prediction. The Abaqus FSDT shell model has the same number of DOFs as KLWZ, but it considers warping only indirectly and approximatively by means of shear correction factors tuned for laminates. However, this model becomes unreliable for high stiffness ratios of the layers, as occurs for typical alternating laminates.

The numerical results will focus on the main outputs governing the mechanical behavior of alternating laminates with high stiffness ratios:

- load-displacement paths;
- in-plane stresses in the stiff layers;

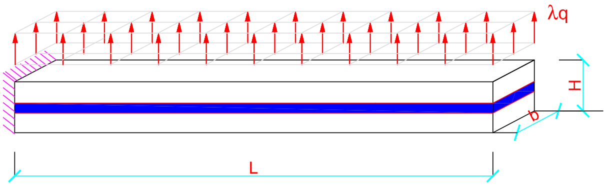

Figure 3.5: Cantilever beam under transverse load: geometry, load, and boundary conditions.

- transverse shear strains in the soft interlayers.

The load-displacement curves are the main object, necessary to assess deformability and stability. The in-plane stresses dominate the strength check of the stiff layers. Transverse shear stresses are largely negligible in the stiff layers, which behave as Kirchhoff-Love shells loosely coupled by the interlayers, compared to the in-plane stresses. However, if desired, they can be accurately obtained from the in-plane stresses by a standard equilibrium-based stress recovery (e.g. see [104]). Finally, an accurate prediction of transverse shear strains/stresses is required in the soft interlayers to check the bonding capacity. It is worth noting that these strains can be computed directly from the kinematics in the proposed shell model with warping and the corresponding stresses are obtained by applying the constitutive law. As demonstrated in [70], the 3D solution furnishes transverse shear strains/stresses practically constant through the interlayer thickness for the considered laminates.

3.5.1 Multi-layer cantilever beam

Large deflection due to a transverse distributed load

The first test displays the non-linear analysis of a cantilever beam of length $L = 500$ mm and and $b = 10$ mm subjected to a distributed transversal load on the top stiff layer as illustrated in Fig. 3.5. To begin with, the stacking sequences $L3_A$ and $L3_B$ are considered. The reference surface load is $q = 10^{-3}$ MPa for $L3_A$ and $q = 10^{-4}$ MPa for $L3_B$.

The beam is analyzed with the KLWI model (coincident with KLWZ) and different meshes varying the number of elements along the length. The finest mesh is considered for the basic KL solution. The load factor vs. tip displacement equilibrium curve is reported in Fig. 3.6 for the two layups and using the different models. The transverse component w and the axial component u are monitored. As can be seen from the comparison between the different meshes adopted, the rate of convergence of the model is remarkable. The comparison shows a very good performance of the proposed solution, given the good agreement with the Abaqus solid solution. On the contrary, the lack of transverse shear deformations in the basic KL model brings to over-stiff solutions. Also the shear deformable shell model of Abaqus is inaccurate for this class of composites because the adopted shear correction factors become unreliable for large stiffness ratios of the materials and will be discarded in the other tests. Subsequently, the same beam is analyzed with all the other layups to compare KLWI with KLWZ for more than 3 layers. Table 3.2a shows the linear elastic solution for the tip displacement considering $q = 10^{-3}$ MPa and a converged mesh. It is possible to observe that KLWI demonstrates to be robust for every type of alternating layups. KLWZ provides the same results for $L5_A$ (uniform stiff layers and uniform soft layers) and $L5_B$ (non-uniform stiff layers and uniform soft layers) with a reduced number of DOFs with respect to KLWZ, but its prediction is inaccurate for $L5_C$ (non-symmetric) and $L7$ (symmetric), both characterized by non-uniform soft layers. This holds also varying the beam length as reported in Tab. 3.2b and 3.2c, apart from very slender cases for which warping gets less important. The reason of this inaccuracy for non-uniform soft layers can be understood by looking at Fig. 3.7, showing the ratio of the transverse shear deformations of the soft layers for $L5_C$ (two soft layers, i.e. 2 and 4) and $L7$ (three soft layers, i.e. 2, 4 and 6) obtained for the linear elastic solution. It can be seen that the ratio of the transverse shear deformations among non-uniform soft layers varies with the beam length. This means that KLWZ, based

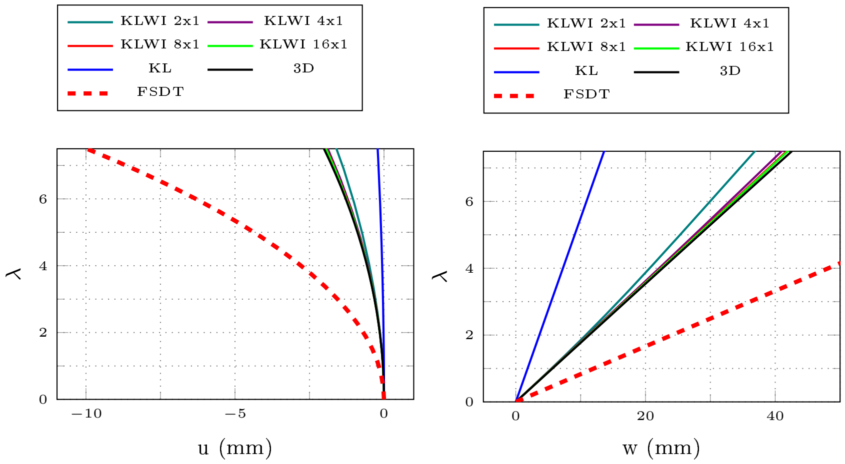

Layup $L3_A$

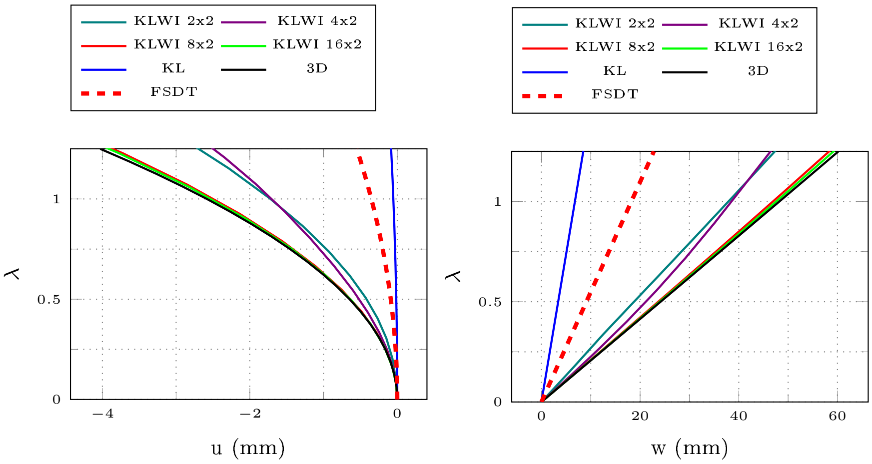

Layup $L3_B$

Figure 3.6: Cantilever beam under transverse load: comparison of the equilibrium path in terms of vertical (w) and axial (u) displacement components at the free end obtained by KLWI and KL shell model with solid model and FSDT shell model of Abaqus.

Layup	KLWI	KLWZ	Abaqus solid
$L5_A$	1.13e-1	1.13e-1	1.13e-1
$L5_B$	3.87e-1	3.87e-1	3.88e-1
$L5_C$	1.51e-1	8.73e-2	1.52e-1
$L7$	1.17e-1	7.65e-2	1.17e-1

(a) Beam length $L = 500mm$

$L(mm)$	KLWI	KLWZ	Abaqus solid	$L(mm)$	KLWI	KLWZ	Abaqus solid
250	1.33e-2	5.80e-3	1.36e-2	250	1.02e-2	5.42e-3	1.04e-2
500	1.51e-1	8.73e-2	1.52e-1	500	1.17e-1	7.65e-2	1.17e-1
1000	1.43	1.15	1.44	1000	1.02	0.85	1.03
2000	13.1	12.3	13.1	2000	7.90	7.39	7.90
3000	49.6	48.1	49.6	3000	26.9	25.9	26.9

(b) Layup $L5_C$ varying the beam length

(c) Layup $L7$ varying the beam length

Table 3.2: Cantilever beam under transverse load: converged linear elastic tip transverse displacement (mm) varying layup and beam length for KLWI and KLWZ shell models and Abaqus solid model.

on a single zig-zag function constraining this deformation ratio, cannot capture the correct behavior. This means that a single zig-zag function, whatever it is, is not sufficient in case of non-uniform soft layers, even for symmetric stacking sequences as $L7$.

Buckling under compression

The same cantilever beam seen in the previous test is now subjected to a compression load on the glass layers at the free end section, as described in Fig. 3.8. The layups $L3_A$ and $L3_B$ are considered. The reference edge compression load is $q = h_{st} \cdot 1$ MPa, with h_{st} (mm) the sum of the thicknesses of the stiff layers. The reference shell surface corresponds to the middle surface of the laminate.

The same meshes considered in the previous example are adopted here, comparing the KLWI model (equivalent to KLWZ) to the basic KL model and the Abaqus solid results. In order to avoid the bifurcation jump of the perfect structure after almost null pre-buckling deformations, a small transverse tip edge load of magnitude $q \cdot 10^{-4}$ is applied as an out-of-plane imperfection. Figure 3.9 shows the curve of the imperfect structure for the two layups and the different models, in terms of load multiplier vs. transverse displacement at the free end. In this case, the coarsest mesh is sufficient for the KLWI model to capture the right behavior of the structure, in agreement with Abaqus solid solution. Instead, the basic KL model dramatically over-estimates the buckling load of the structure.

3.5.2 3-layer simply supported square plate

Large deflection under transverse load

The large deformation of a simply supported square plate under a transverse load is studied in this test. Geometry, load and boundary conditions are reported in Fig. 3.10. Both the layups $L3_A$ and $L3_B$ are considered in the test. The support is applied on the perimeter of the middle surface of the shell. The reference surface load is $q = 10^{-4}$ MPa for both the stacking sequences.

Different meshes are considered for the KLWI model, while only the finest mesh is adopted for the basic KL model. The reference shell surface corresponds to the middle surface of the packet. In Fig. 3.11, the equilibrium path in terms of load factor vs. the out-of-plane displacement at the center of the plate is shown. The membrane contribution to the overall stiffness grows with the deformation rate, causing the increase of the curve slope. Once again, the superposition of the curves obtained with the KLWI model for the different meshes and the curve obtained from Abaqus solid model testifies to the high level

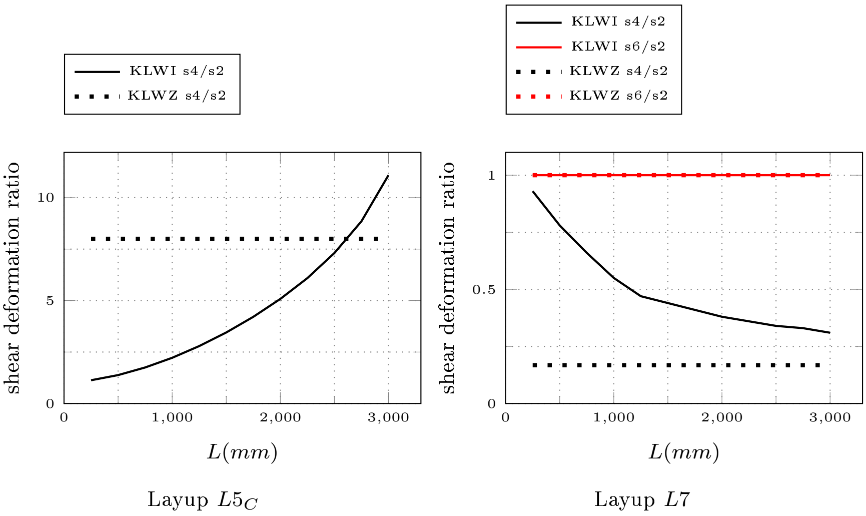

Layup $L5_C$ Layup $L7$

Figure 3.7: Cantilever beam under transverse load: mean transverse shear deformation (s) ratio of the soft interlayers in the linear elastic solution varying the beam length. Layup $L5_C$ has two soft interlayers, denoted as 2 and 4 counting from the bottom. Layup $L7$ has three soft interlayers, denoted as 2, 4, 6 counting from the bottom, with 2 and 6 of uniform thickness and material.

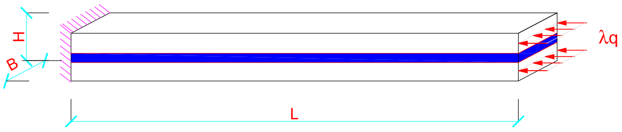

Figure 3.8: Cantilever beam under compression: geometry, load, and boundary conditions.

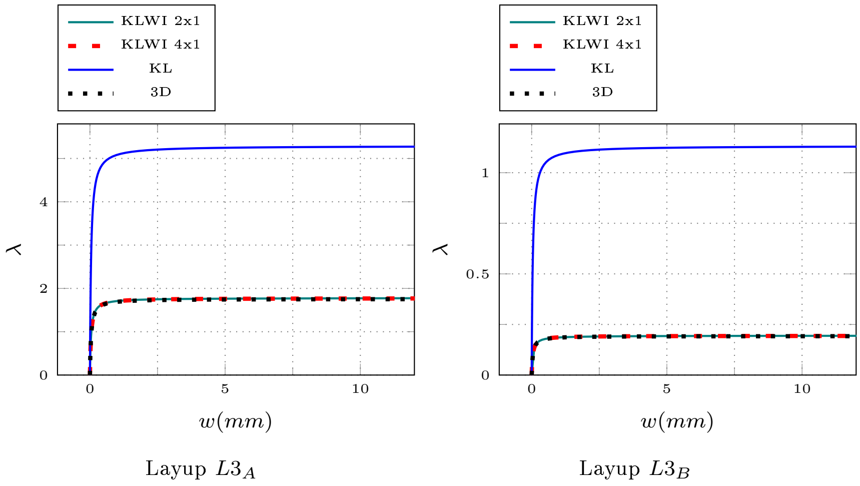

Layup $L3_A$ Layup $L3_B$

Figure 3.9: Cantilever beam under compression: comparison of the equilibrium path in terms of vertical displacement component at the free end (w) obtained by KLWI, KL shell model and Abaqus solid model.

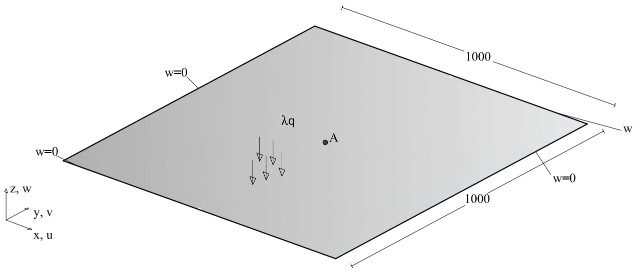

Figure 3.10: 3-layer square plate under transverse load: geometry (mm), load and boundary conditions.

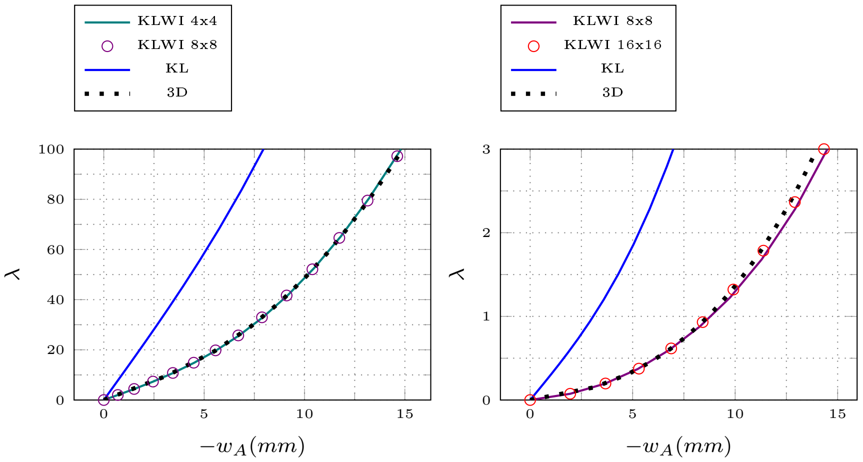

Layup $L3_A$ Layup $L3_B$

Figure 3.11: 3-layer square plate under transverse load: equilibrium path in terms of the transverse displacement component at the plate center and comparison between KLWI shell model, KL shell model and the solid model from Abaqus.

of accuracy achievable by the proposed solution. Equally accurate is the representation of the stress field, as depicted in Fig. 3.12, where the stress component σ_{11} is plotted over the top and bottom surfaces of the glass layers for the different meshes. Also here, the correct representation of the results is achieved also with coarse meshes and validated by the Abaqus 3D solution. Similar conclusions are addressed for the evaluation of the shear strain field in the interlayer, reported in Fig. 3.13. It is worth noting the accuracy of the proposed hierarchic model also when the strain of the interlayer is actually significant. The distribution of σ_{11} and γ_{13} along the thickness is also illustrated in Fig. 3.14 corresponding to their respective surface points of maximum.

Finally, the path-independence and the iterative performances of the numerical model are assessed in Tab. 3.3 for layup $L3_B$. To this aim, a load-controlled scheme with fixed step length is adopted here. The maximum load level is reached with 1, 2 or 4 load subdivisions (steps). When using a single step, the standard full Newton is not able to converge to the equilibrium configuration due to the significant non-linearity of the problem. It can obtain the solution only by 2 or more load subdivisions and a relevant number of total iterations (linear systems). Instead, the MIP Newton method [83, 79] is able to provide the solution with a single step and 7 total iterations. In any case, the predicted final displacement for the maximum load is exactly the same independently of the incrementation procedure highlighting the path-independence of the proposal.

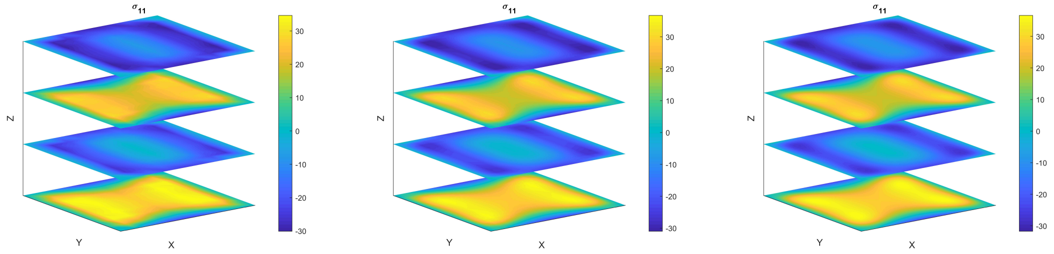

KLWI 8x8 KLWI 16x16 KLWI 32x32

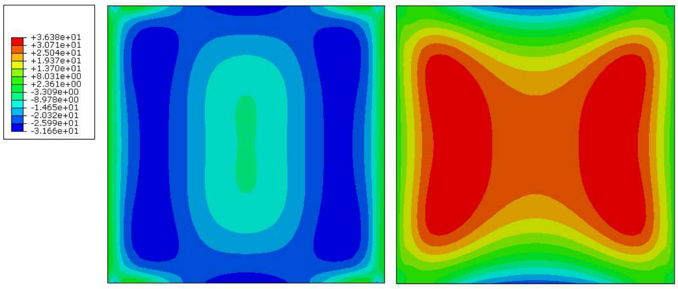

Top (on the left) and bottom (on the right) laminate surfaces from Abaqus solid

Figure 3.12: 3-layer square plate under transverse load: convergence of the stress component σ_{11} (MPa) at the last equilibrium point over the top and bottom surfaces of the stiff layers and comparison with Abaqus solid model for layup $L3_A$.

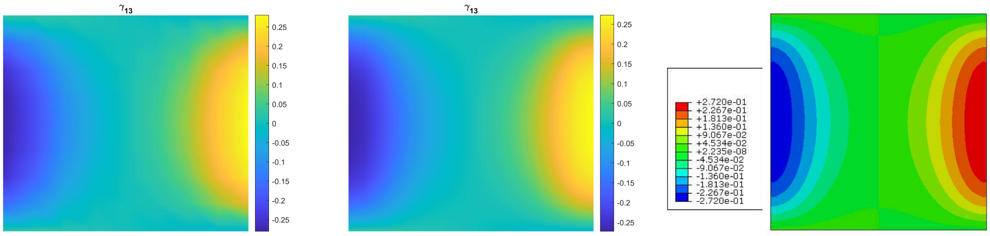

KLWI 8x8 KLWI 16x16 Abaqus solid

Figure 3.13: 3-layer square plate under transverse load: convergence of the transverse shear strain γ_{13} over the interlayer and comparison to solid model results from Abaqus for layup $L3_A$ at the last equilibrium point.

Steps	Newton iterations	MIP Newton iterations	$-w_A(\lambda = 3)$
1	fails	7	14.2768
2	23	11	14.2768
4	27	16	14.2768

Table 3.3: 3-layer square plate under transverse load: number of total iterations and final displacement vs number of increments to reach the maximum load factor $\lambda = 3$ for layup $L3_B$ and shell model KLWI (coincident with KLWZ) with a mesh 16×16.

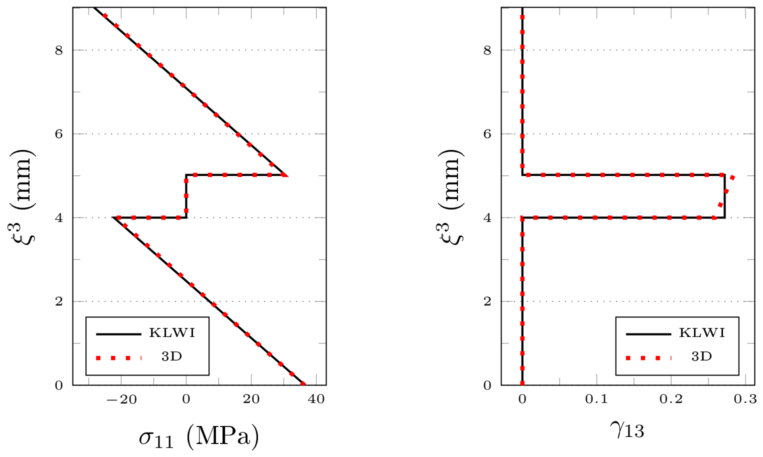

Figure 3.14: 3-layer square plate under transverse load: through-the-thickness distribution of σ_{11} (MPa) and γ_{13} at the last equilibrium point at the their peak point for layup $L3_A$ and comparison to 3D Abaqus model.

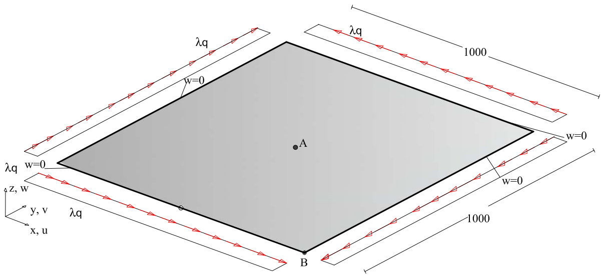

Figure 3.15: 3-layer square plate under transverse load: geometry (mm), load and boundary conditions.

Buckling under in-plane shear load

The following test addresses the buckling behavior of a simply supported square plate under a self-equilibrted in-plane shear load. The $L3_A$ and $L3_B$ stacking sequences are analyzed. Geometry, loads and boundary conditions are illustrated in Fig. 3.15. The reference edge compression load is $q = h_{st} \cdot 1$ MPa, with h_{st} (mm) the sum of the thicknesses of the stiff layers, in the direction parallel to each edge. The support is applied on the perimeter of the middle surface assumed as reference shell surface.

The plate is discretized with progressively refining meshes for the KLWI model, while, as in the previous tests, only the finest mesh is used for the basic KL model. A geometric imperfection with the shape of the first linearized buckling mode and an amplitude equal to 0.1 mm is added to the perfect model. The equilibrium path of the imperfect structure is shown in Fig. 3.16 in terms of out-of-plane displacement of the plate center and the buckling modes are depicted right below the curves for both the layups. The imperfection causes a smooth change in the behavior and the stiffness reduction after the buckling point. Also in this case the KLWI model proves to be accurate, if compared to the reference Abaqus solid solution. Similarly, the stress field is well represented with coarse meshes, as can be seen in Figs. 3.17 where the component σ_{11} is shown for $L3_A$ and for the different meshes adopted. The corresponding values obtained by the Abaqus solid model are reported for comparison. Finally, the coarse-mesh accuracy of the results is confirmed also for the transverse shear strain γ_{13} in the interlayer, as reported in Fig. 3.18 and 3.19 for the two layups. It is worth noting that $L3_B$ generally requires a little finer mesh compared to $L3_A$. From the strain plots, it is clear that this is not due to some sort of locking, but just to the narrower bands

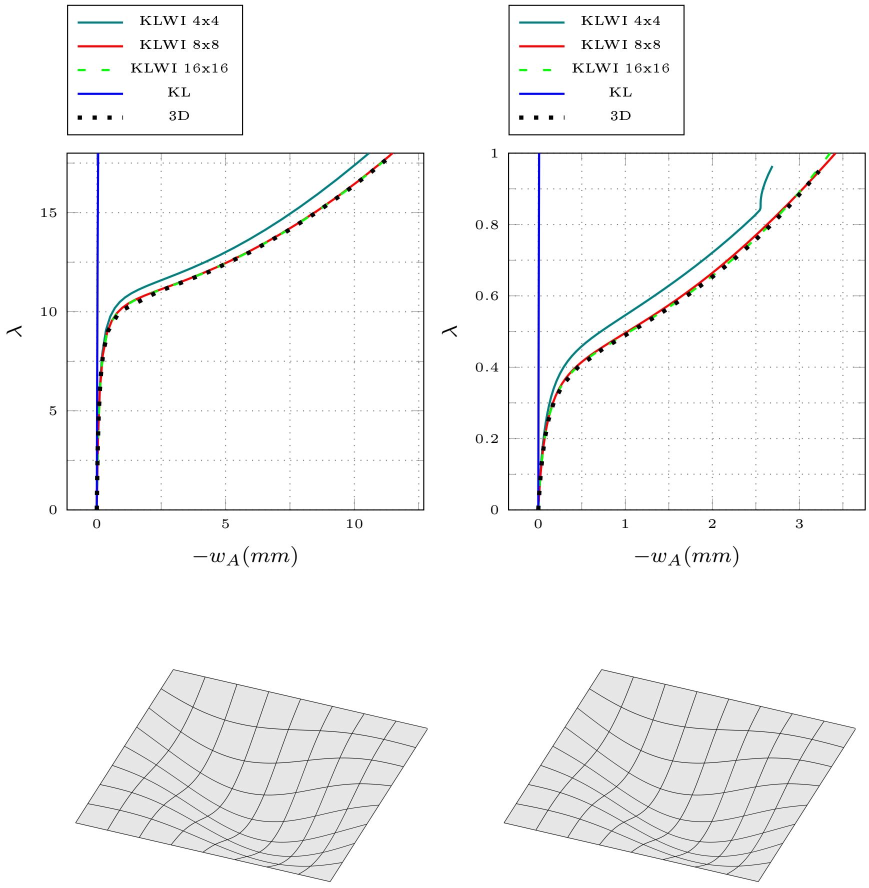

layup $L3_A$ layup $L3_B$

Figure 3.16: 3-layer square plate under in-plane shear: equilibrium path in terms of the transverse displacement component at the plate center obtained by KLWI and KL shell model and Abaqus solid model with illustration of the first linearized buckling mode for the two layups.

characterizing the $L3_B$ solution.

3.5.3 5-layer rectangular plate simply supported on 4 edges

The following test aims at analyzing the performance of the proposed model in case of more than 3 layers. A rectangular simply supported plate made of 5 alternating layers (layup $L5$) is considered for this purpose. The support is assigned on the perimeter of the bottom layer. Two different loading cases are assumed:

- Transverse load $q = 10^{-3}$ MPa distributed over the top layer;
- Axial compression edge load $q = h_{st} \cdot 1$ MPa, with h_{st} (mm) the sum of the thicknesses of the stiff layers, distributed along the short edges.

Geometry, loads and boundary conditions are depicted in Fig. 3.20. The analysis is carried out for different meshes, with double number of elements over the longer edges, for the layup $L5_A$ (symmetric and with uniform soft layers). The equilibrium paths are plotted in Fig. 3.21. The two load conditions are characterized by large deflection and buckling respectively. In particular, for the second load case, the structure is nudged on the bifurcated path introducing a geometric imperfection with the shape of the first linearized buckling mode and a maximum deviation equal to 0.1 mm. The deformed configurations at the last

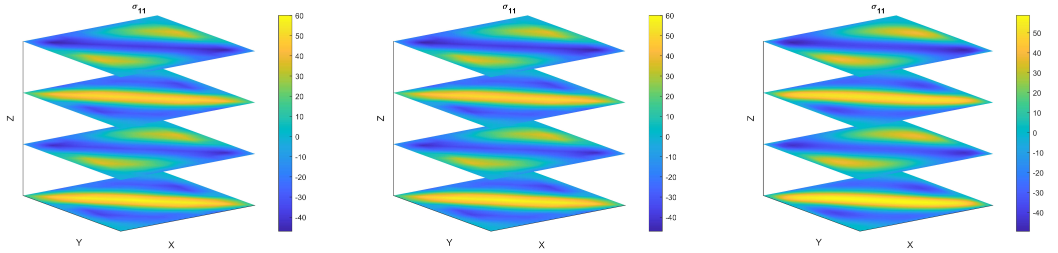

KLWI 4x4 KLWI 8x8 KLWI 16x16

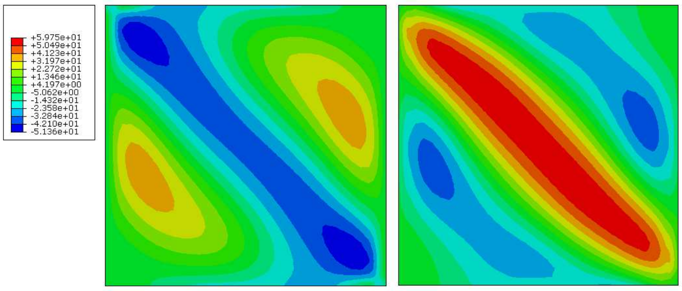

Top (on the left) and bottom (on the right) laminate surfaces from Abaqus solid

Figure 3.17: 3-layer square plate under in-plane shear: convergence of the stress component σ_{11} (MPa) at the last equilibrium point over the top and bottom surfaces of the stiff layers and comparison with Abaqus solid model for layup $L3_A$.

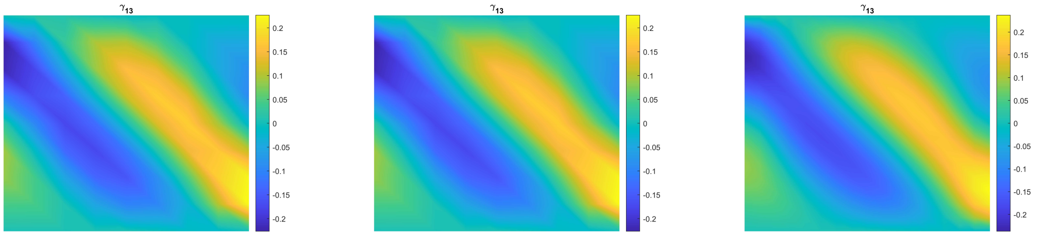

KLWI 4x4 KLWI 8x8 KLWI 16x16

Figure 3.18: 3-layer square plate under in-plane shear: convergence of transverse shear strain γ_{13} at the last equilibrium point over the interlayer for layup $L3_A$.

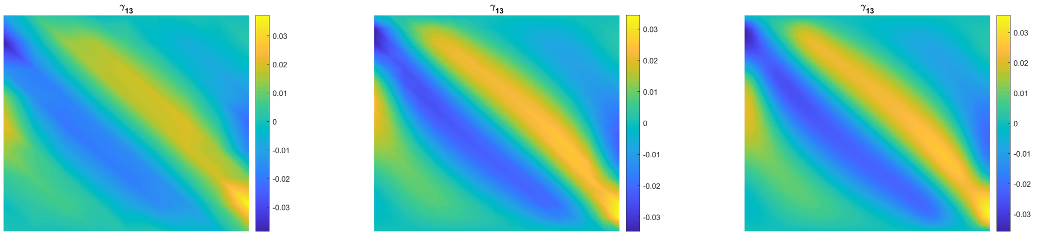

KLWI 8x8 KLWI 16x16 KLWI 32x32

Figure 3.19: 3-layer square plate under in-plane shear: convergence of the transverse shear strain γ_{13} over the interlayer for layup $L3_B$ at the last equilibrium point.

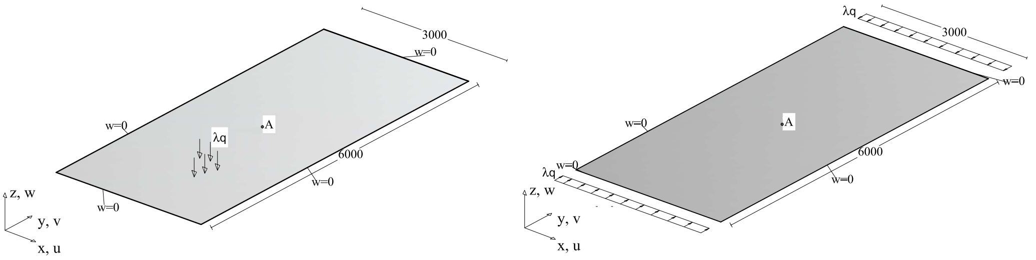

Transverse load Axial compression

Figure 3.20: Rectangular plate: geometry (mm), loads, and boundary conditions.

Layup	KL	KLWI	KLWZ	Abaqus solid
$L5_A$	43.40	17.42	17.42	17.43
$L5_B$	14.59	8.045	8.055	8.050
$L5_C$	44.94	11.24	14.15	11.53

Table 3.4: 5-layer rectangular plate under compression load: linearized buckling load multiplier for the different models and layups.

equilibrium point are also reported below the curves in Fig. 3.21. The comparisons of the different models confirms the accuracy of the proposed KLWI model also in case of multiple soft layers, unlike the basic KL model. Also in this case, coarse meshes are sufficient to obtained the solid reference solution. The analysis is repeated for a fine converged mesh also for the other 5-layer layups: $L5_B$ (non-uniform stiff layers and uniform soft layers) and $L5_C$ (uniform stiff layers and non-uniform soft layers). The corresponding load-deflection curves are depicted in Fig. 3.22 for the transverse load case, including the comparison with the model with a single zig-zag warping function KLWZ. It is possible to observe that, also in this case, KLWZ proves to be a convenient alternative (less DOFs) to KLWI for alternating layups with uniform soft layers, while it results less accurate for non-uniform soft layers. Similar considerations hold when considering the compression load case, for which the linearized buckling load multiplier is reported in Tab. 3.4 for the different models and layups. KLWZ has the same accuracy as KLWI for $L5_A$ and $L5_B$, while the non-uniform soft layers of $L5_C$ negatively affects its prediction. On the other hand, considering the geometry of $L5_A$, Fig. 3.23 demonstrates the reliability of KLWZ for uniform soft layers in predicting the linearized buckling load also for all possible stiffness ratio of the two materials. Interestingly, when the stiffness of the soft layers tends to vanish, the hierarchic model is able to recover the correct limit P_{crit0} of the uncoupled stiff layers. Furthermore, the basic KL gets inaccurate for stiffness ratios $E_{soft}/E_{stiff} < 10^{-2}$.

3.5.4 Curved panel under vertical load

The final test concerns the non-linear analysis of the curved laminated glass panel whose geometry and boundary condition are reported in Fig. 3.24. The aim of the test is just to assess the correctness of the hierarchic formulation for initially curved geometries.

A vertical distributed load $q = 1$ MPa and $q = 10^{-3}$ MPa are applied for the layup $L3_A$ and $L3_B$ respectively. The roof is modeled using four different meshes, varying the number of elements in both dimensions from 4 to 32, each time doubling the refinement. In Fig. 3.25 the vertical displacement at the midpoint of the straight side of the structure is reported against the load multiplier λ. The KLWI model is compared to the KL model and the reference prediction obtained using the solid model in Abaqus. The reference shell surface corresponds to the lower surface of the laminate where the support is applied. The results testify the accuracy of the proposed model also in the case of curved geometries. The remarkable coarse-mesh accuracy of the discretization method is confirmed also in this case.

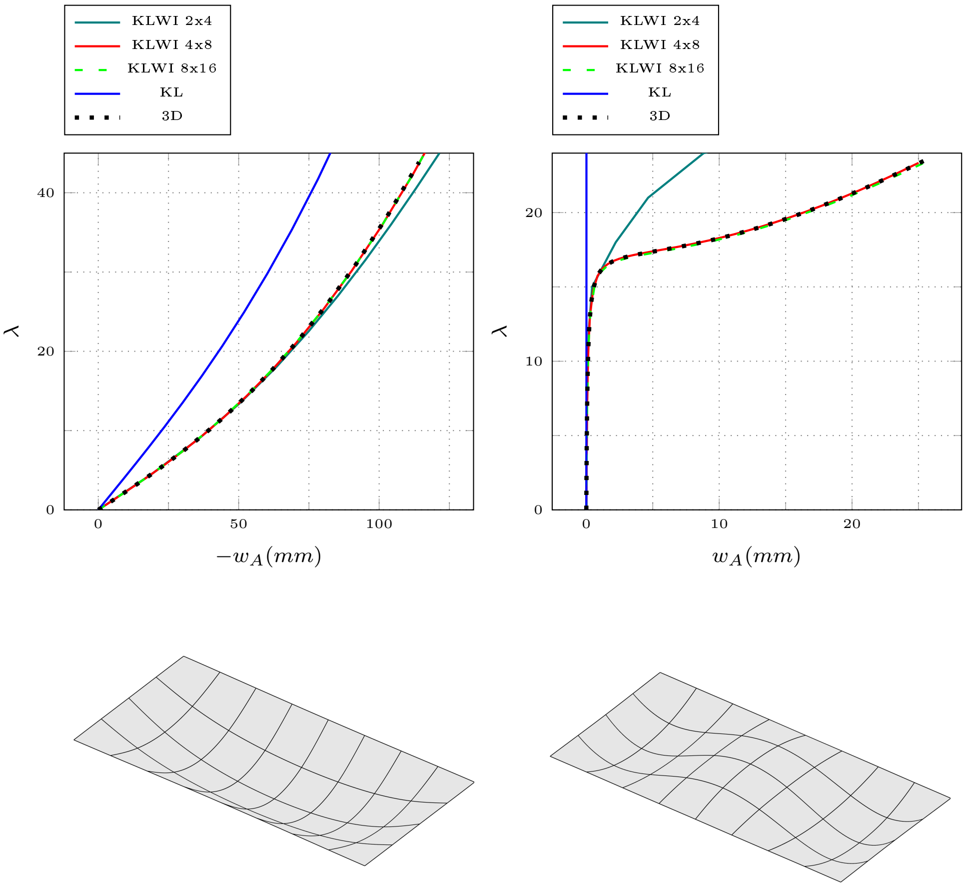

Transverse load

Axial compression

Figure 3.21: 5-layer rectangular plate: equilibrium path in terms of the transverse displacement component at the plate center for KLWI shell model, KL shell model and Abaqus solid model for the two load cases and layup $L5_A$. Deformed configuration plots for the maximum load factor (scale factor 10).

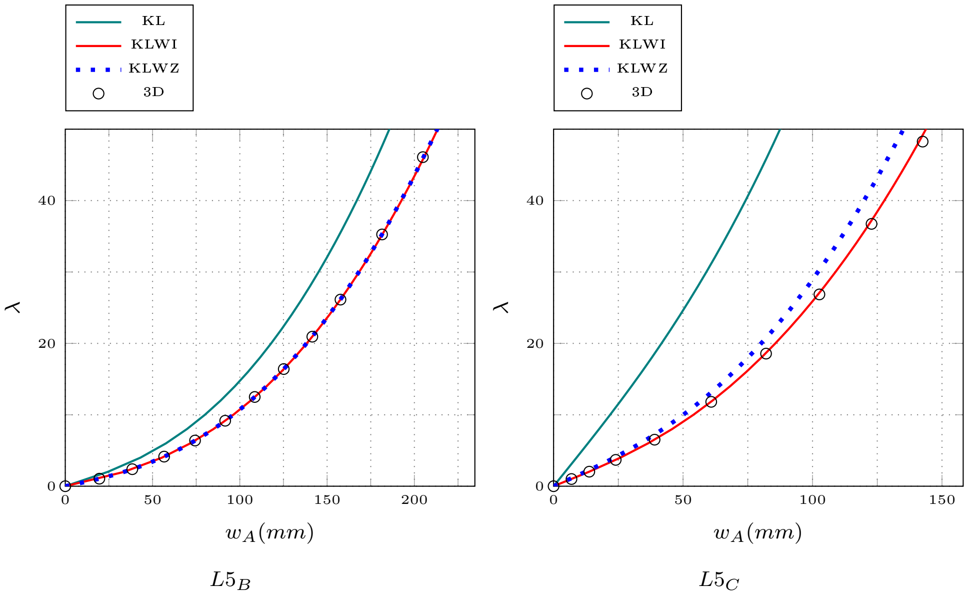

Figure 3.22: 5-layer rectangular plate under transverse load: converged equilibrium path in terms of the transverse displacement component at the plate center for KLWI shell model, KL shell model and Abaqus solid model for layup $L5_B$ and $L5_C$.

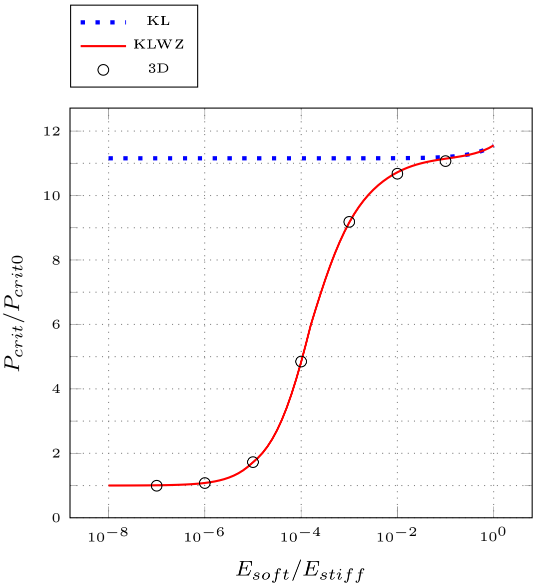

Figure 3.23: 5-layer rectangular plate under compression load: linearized buckling load multiplier for layup $L5_A$ normalized with respect to that of the uncoupled stiff layers P_{crit0} varying the stiffness ratio of the layers.

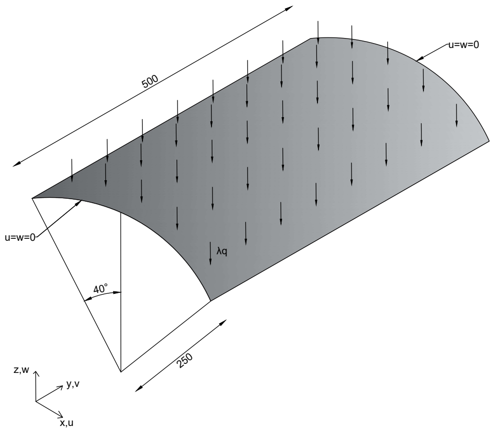

Figure 3.24: Curved panel: geometry (mm), loads, and boundary conditions.

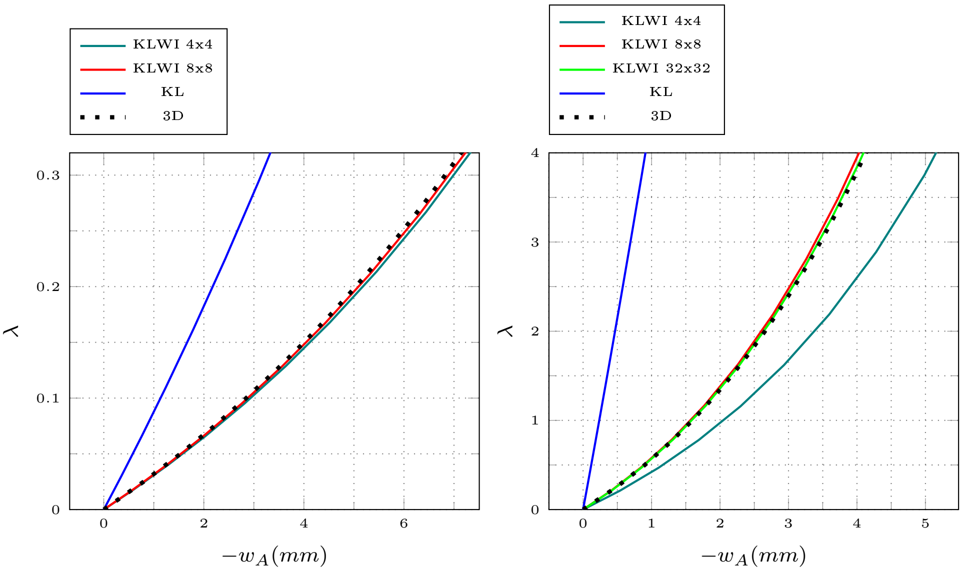

Layup $L3_A$

Layup $L3_B$

Figure 3.25: Curved panel: equilibrium path in terms of the transverse displacement component at the mid point of the longitudinal edge and comparison of KLWI shell model, KL shell model and Abaqus solid results.

Layer index	Layer material	Layer thickness		
		$HL1$	$HL2$	$HL3$
1	(F)	1/5h	1/15h	3/25h
2	(C)	1/5h	2/15h	5/25h
3	(F)	1/5h	3/15h	9/25h
4	(C)	1/5h	4/15h	5/25h
5	(F)	1/5h	5/15h	3/25h

Table 3.5: Hemispherical shell: description of the three layups, labeled as $HL1$, $HL2$ and $HL3$.

3.5.5 Multi-layer hemispherical shell with 18° cut-off

This benchmark concerns a 5-layer hemispherical shell with a circular cut-off at its top, as reported in Fig. 3.26 (one quarter of the shell with symmetric boundary conditions), with the same geometry, loads and material layups proposed in [70]. The input data are given in dimensionless form as in [70]. The hole aperture is 18°, the sphere radius is 10, and the shell thickness is $h = 0.075$. The shell is subjected to equal and opposite concentrated forces applied at the four cardinal points of its equator amplified by the factor λ. The top and bottom curved edges are free. The rigid body motion is eliminated by fixing the vertical displacement at an arbitrary point. This final tests is aimed at assessing the accuracy of the proposed shell models for a doubly curved shell and for very large deformations. Three alternative layups are considered, including symmetric and asymmetric laminations. The layer material type and thickness for each layup are reported in Tab. 3.5, where layer 1 denotes the interior layer of the hemispherical shell. The material parameters for the stiff layers (F) and soft layers (C) are: $E_F = 1.0 \times 10^7$, $E_C = 5.0 \times 10^3$ and $\nu_F = \nu_C = 0.2$.

Exploiting the symmetry, only one quarter of the shell is modeled. The non-linear load-displacement curves (see Fig. 3.27) obtained with are in good agreement with those reported in [70] and obtained with a Reissner corotational shell model enhanced with warping which reproduces the 3D solution. As observed for the other tests, KLWZ gives the correct solution (coincident with KLZI) for layups $HL1$ and $HL3$ characterized by uniform soft layers (same thickness and material), while a small error affects the solution for $HL2$. This error is smaller in this test compared to the others due to the milder difference in the stiffness of the materials and is canceled when using KLWI. This confirms the reliability of our more efficient models with warping (fewer DOFs compared to [70]) also for doubly curved shells undergoing very large displacements (more than half the radius) and rotations. As shown in [70], the FSDT shell is inaccurate in this case due to the significant warping, with results close to the KL solution reported in Fig. 3.27.

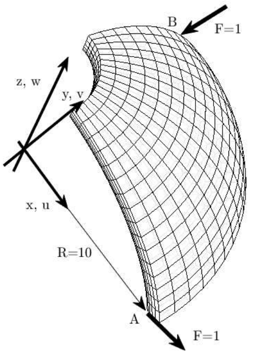

Figure 3.26: Hemispherical shell: geometry (enlarged in the thickness direction) and applied loads.

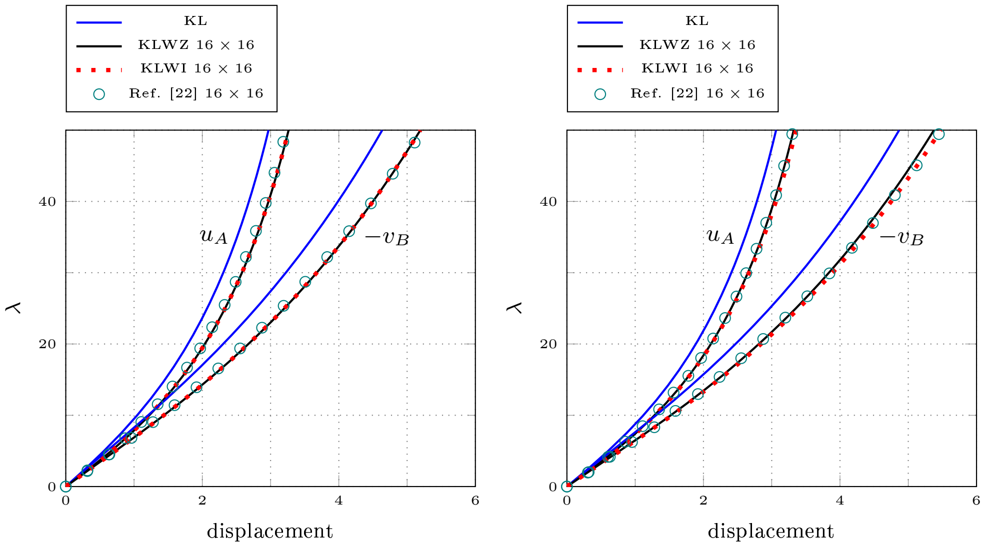

Layup $HL1$ Layup $HL2$

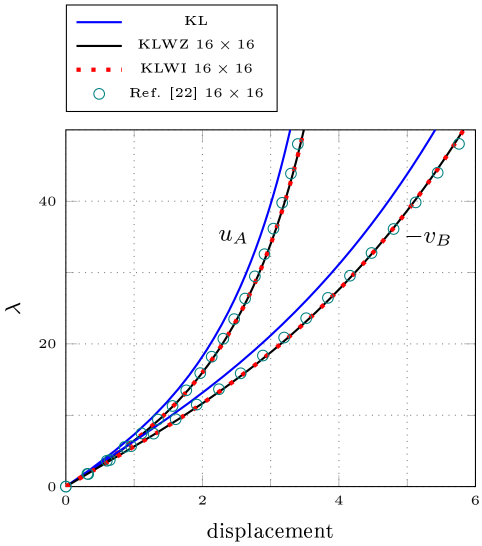

Layup $HL3$

Figure 3.27: Equilibrium paths for the hemispherical shell: comparison of KLWZ and KLWI shell models with the results from [70] for layup $HL1$, $HL2$ and $HL3$.

3.6 Summary

This Chapter presented a Total Lagrangian large deformation Kirchhoff-Love model hierarchically enhanced with warping profiles generically selected by the user. The small strain hypothesis was exploited to derive a simple and efficient yet accurate strain measure. An effective NURBS-based discretization was proposed for the problem in weak form, characterized by excellent coarse-mesh accuracy and small number of integration points. A numerical investigation demonstrated the correctness of the hierarchic formulation in large displacement and buckling problems. Particular attention was given to the modeling of alternating stiff/soft stacking sequences, representing a technically significant example characterized by a peculiar warping profile: transverse shear strains concentrate in the soft interlayers while the stiff layers behave as Kirchhoff-Love shells with equal rotation of the normal. Two warping models were studied: 1) independent transverse shear deformations of the soft layers and 2) single zigzag function linking these deformations. The comparison with the reference solid solution showed the great accuracy and reliability of the first warping model, whose number of DOFs depends on the number of soft layers, when usual shell models provide largely wrong predictions. On the other hand, the second warping model allows to reduce the unknowns to five per surface point regardless of the number of layers. This reduction produces no loss of accuracy when the soft interlayers are uniform in terms of thickness and stiffness, as in most practical cases. However, the first warping model is recommended for non-uniform soft layers. In this case, the actual warping profile varies widely even with structural properties other than the layup, so that a single zigzag function, whatever it is, results unreliable. The first warping model seems also the ideal choice for more complex simulations taking into account also thermal and viscous effects.

Chapter 4

New robust and efficient global iterations for large deformation finite element analysis of beams and shells with material non-linearity

In large rotation analyses of beams and shells with displacement-based discretization, the iterative burden grows considerably with the membrane/flexural stiffness ratio. For linear elastic materials, it was shown that a stress-displacement iteration solves this issue and reduces the computational cost even of several times. Convergence problems occur also when large rotations are coupled to material non-linearity, even if this case is not well addressed in the literature. The extension of the mixed iteration to large deformation problems with non-linear constitutive laws is faced in this Chapter , focusing on elastoplasticity. New iterative schemes are derived for both displacement-based finite elements (DFEs) and mixed finite elements (MFEs), each featuring further variables in the linearization along with displacements. For DFEs, it is shown that the most convenient approach is to impose the constitutive law for an independent integration point strain, with the strain-displacement compatibility solved together with the global equilibrium. For MFEs, as an extension of this strategy, the most performing scheme solves element compatibility and global equilibrium simultaneously, with the element state evaluated for independent strains work-conjugate of the stress DOFs. In both cases, global linear systems in displacements only are required and strain-driven material laws are easily considered. Numerous tests validate the proposed iterative schemes showing a significant reduction of the computational cost compared to standard approaches.

4.1 Introduction

Thin structural elements like rods, plates and shells can be assumed as a mechanical model for an incredibly wide range of engineering problems. Aerospace composite structures [73, 33, 47], steel cold-formed beams [25] and tanks [42] are classical applications in the fields of mechanical, civil and aerospace engineering. But the flexibility of this model is witnessed by much more unconventional applications: blood vessels [45], contact lenses [122], carbon nanotubes [38, 40], muscular tissues [96], drape simulations [142] and even spider webs [58] can be modeled as beams and shells. That explains the great interest arising about the need to optimize our knowledge and control over the related analysis tools, in particular for large deformations and material non-linearities.

The macroscopic distinctive feature of this family of structures is the lack of homogeneity in the three dimensions, which makes the length prevailing over the cross section in beams and the mid-surface spans predominant over the thickness in plates and shells. This brings as a consequence that the axial/membrane stiffness is significantly greater than the flexural one and geometric non-linearities due to large deformations and/or buckling usually arise, even when the material is still in the elastic range.

Traditionally, the modeling of slender beams and shells is approached through the finite element (FE) method. The discrete equilibrium non-linear equations are completed with an arc-length constraint and solved in an incremental-iterative manner using the Newton method, thus obtaining the equilibrium path of the structure. Two major aspects affect the computational burden of this well-established strategy, namely the discretization, i.e. total number of discrete degrees of freedom (DOFs) and sparsity of the discrete equations, and the iterative burden needed to obtain the points of the equilibrium curve. In this work, attention is mainly addressed to this second aspect.

The existing FE technology is mainly based on two formulations. In displacement-based FEs (DFEs) the kinematic field is directly interpolated and the unknowns of the problem are the discrete displacement DOFs. Strategies like Assumed Natural Strain (ANS), Enhanced Assumed Strain (EAS) and reduced integrations are very popular choice to improve the accuracy of DFEs avoiding locking. In mixed (stress-displacement) FEs (MFEs), both stress and displacement are directly approximated, with the stress shape functions designed to avoid locking. A disadvantage of MFEs with respect to DFEs is that the evaluation of the internal force vector is more involved and time consuming, especially for non-linear material laws for which an iterative element state determination is needed [99]. However, for some particular problems such as for beams undergoing plasticity and relatively small deformations, MFEs can require coarser meshes due to the excellent approximation of the equilibrated stress field [132]. This feature is generally lost for large deformations and general shell problems [131]. As an advantage of the mixed formulation, many studies have proven it to be more robust in geometrically non-linear analysis of elastic structures when compared to the displacement-based formulation, also allowing larger steps in path-following non-linear analyses and fewer Newton iterations. In [131] a displacement and a mixed (hybrid-stress) solid-shell FE are developed which yield close predictions, but the Newton method converges more readily and can withstand larger load increments for the MFE in all the examined problems. In [26, 141], the authors draw similar conclusions in the context of Reissner shell FEs. The superior convergence of MFEs was also observed in unconventional geometrically non-linear analyses, such as the Koiter-Newton method [86] and generalized path-following methods [81]. Some considerations on the topic are drawn also in [92] for the solution in strong form with the collocation method. The iterative advantages of MFEs can be observed also in implicit large deformation dynamics as shown in [9]. Nevertheless, it is necessary to mention a precursory work [37], where for the first time it was shown that the path-following analysis of slender elastic beams discretized via DFEs is affected by an iterative burden that increases with the axial/flexural stiffness ratio in large rotation problems. According to that paper, this feature is due to the fact that the stress used to evaluate the iteration matrix can be affected by a large error when computed from wrong displacements predicted during the iterations. This does not occur for MFEs, where the discrete stress DOFs are independent variables of the iterative process. A more recent work [82] investigated the fast convergence and the high robustness of MFEs in the more general context of large deformation 3D elasticity. One of the main conclusion of this work is that the readier convergence of the Newton method for MFEs is not linked to the FE interpolation, but due just to the different format of the iterations. This result is the starting point of [83], where, for linear elastic materials, the benefit of a mixed iterative scheme in large deformations was extended to DFEs without introducing a FE approximation for the stress. The strategy, called MIP (Mixed Integration Point) Newton, consists in relaxing the constitutive equations at each integration point. This allows, on the one hand, to maintain the original form of the displacement-based internal forces and stiffness matrix, but at the same time to directly predict and correct the stress at each integration point as independent variable in the iterative process. As a consequence, using the MIP method, the ready convergence of MFEs is obtained also for DFEs. Extensions was made by various authors to Isogeometric Analysis [64], strong form solutions [93], patch coupling via penalty stiffness [65], where the method permits the use of very high penalty coefficients, and implicit dynamics [84]. It is important to note that for both MFEs and MIP formulations, the stress variables are local to the FE or the IP respectively. They are condensed out locally before solving the global linear system of the current iteration that maintains, then, the same size and sparsity of the displacement formulation. Finally, the MIP method was recently extended to EAS solid FEs [106] considering also material non-linearity, focusing on large strain problems and a simplified MIP iteration.

A simple and fully consistent extension of the mixed iteration strategy to the large deformation analysis of beams and shells with non-linear constitutive law is considered in this Chapter. Focus is given to large rotation/small strain elastoplasticity, where the high stiffness ratios have a huge impact on the simulation cost using standard solution schemes. With respect to the linear material case, for both DFEs and MFEs, new iterative schemes are derived and assessed, each featuring further independent variables in the linearization along with displacements. For DFEs, it is shown that the most convenient approach is to impose the constitutive law for an independent integration point strain, with the strain-displacement compatibility solved together with the global equilibrium. For linear material law, this is equivalent to the stress-displacement MIP method [83] in improving efficiency and robustness in large rotation problems with high stiffness ratios. They differs for non-linear materials, where the new proposal allows to use standard strain-driven constitutive equations solved exactly at each global iteration. The issue of an optimal iterative procedure arises also for MFEs when considering general non-linear materials. As an extension of this strategy, the most performing scheme solves element compatibility and global equilibrium simultaneously, with the element state evaluated for independent strains work-conjugate of the stress DOFs. Also in this case, the non-linear material law can be imposed in a classical strain-driven way. In both cases of DFEs and MFEs, global linear systems in displacements only are required, so that the cost of each global iteration remains unchanged. Numerous tests on beams and shells are reported to validate the proposed schemes and to show their far superior efficiency compared to standard iterative solutions. The Chapter is organized as follows: Section 2 reports a short overview of DFEs, also improved by EAS, and MFEs for general material law with the definition of some notation; Section 3 discusses the iterative schemes for DFEs with and without EAS, focusing on the novel strain-displacement iteration method for non-linear material; Section 4 provides an extension of the strain-displacement iteration to MFEs in the case of non-linear material; Section 5 describes briefly the beam and shell models and their FE discretizations used in the numerical tests together with some implementation details required to make the numerical tests completely reproducible; Section 6 presents the numerical tests and discusses the improvements in terms of robustness and efficiency of the proposal; a concluding summary is reported in Section 7.

4.2 Finite element formulations for large deformation analysis with non-linear material

This section recalls three well-established finite element formulations for large deformation problems with material non-linearity. The main equations are presented for general structural and material models for the subsequent developments and also in order to introduce the main notation.

4.2.1 Displacement-based finite elements

In DFE formulations only the displacement field is interpolated in each element of the structural domain:

$$\mathbf{u}[\boldsymbol{\xi}] = \mathbf{N}_d[\boldsymbol{\xi}]\mathbf{d}_e \tag{4.1}$$

where $\mathbf{d}_e$ are the element discrete kinematic DOFs, linked to the global ones $\mathbf{d}$ by the relation $\mathbf{d}_e = \mathbf{A}_e\mathbf{d}$ with $\mathbf{A}_e$ the assembly operator, and $\boldsymbol{\xi}$ are the coordinates used to express the FE interpolation. The term displacement is used in a wide sense, including also rotations if they exist in the structural model. The dependence on the coordinates will be omitted in the following in order to simplify the notation. The components of the strain or generalized strain can be collected in a vector $\boldsymbol{\varepsilon} = \boldsymbol{\varepsilon}[\mathbf{u}]$ that, introducing the interpolation in (4.1), assumes the form

$$\boldsymbol{\varepsilon} = \boldsymbol{\varepsilon}[\mathbf{d}_e], \tag{4.2}$$

generally non-linear in $\mathbf{d}_e$. The variation of the strain vector can be written as

$$\delta\boldsymbol{\varepsilon} = \mathbf{B}[\mathbf{d}_e]\delta\mathbf{d}_e,$$

with $\mathbf{B}[\mathbf{d}_e]$ the virtual/tangent compatibility operator of the discrete model. The structural problem parametrized in terms of all the displacement DOFs collected in $\mathbf{d}$ can be formulated in weak form by means of the virtual work equation

$$\delta\Pi[\mathbf{d}] = \int_V \left(\delta\boldsymbol{\varepsilon}^T\boldsymbol{\sigma}[\boldsymbol{\varepsilon}]\right) dV - \delta W^{\text{ext}} = 0 \quad \forall\delta\mathbf{d}, \tag{4.3}$$

where V is the spatial structural domain, W^{ext} is the work of the external loads and a generic $\boldsymbol{\sigma}[\boldsymbol{\varepsilon}] = \boldsymbol{\sigma}[\mathbf{d}]$ denotes in a simplified way, from now on, the vector collecting the stress components computed from any constitutive model in terms of specified strain, strain rate (plasticity) or functional of strain (viscoelasticity). Equation (4.3) leads to the discrete equilibrium equations of the FE model

$$\mathbf{s}[\mathbf{d}] - \mathbf{p} = \mathbf{0}, \tag{4.4}$$

where $\mathbf{p}$ is the discrete external load vector and $\mathbf{s}[\mathbf{d}]$ is the global internal force vector obtained by assembling the element counterparts

$$\mathbf{s}_e[\mathbf{d}_e] = \int_{V_e} \left(\mathbf{B}[\mathbf{d}_e]^T\boldsymbol{\sigma}[\mathbf{d}_e]\right) dV_e = \sum_g \mathbf{B}_g[\mathbf{d}_e]^T\boldsymbol{\sigma}_g[\mathbf{d}_e]w_g \tag{4.5}$$

usually computed using a numerical integration with the subscript g denoting quantities evaluated at the generic IP and w_g its weight.

4.2.2 Displacement-based finite elements with Enhanced Assumed Strain

A popular and effective technique for improving the accuracy of DFEs is EAS [12]. Essentially, EAS can be seen as a displacement formulation with additional incompatible approximation functions for the displacement or directly for the strain field in the most common versions. In this last case, the strain is approximated as

$$\boldsymbol{\varepsilon} = \boldsymbol{\varepsilon}[\mathbf{d}_e, \boldsymbol{\alpha}_e] = \boldsymbol{\varepsilon}_c[\mathbf{d}_e] + \boldsymbol{\varepsilon}_i[\boldsymbol{\alpha}_e], \tag{4.6}$$

where $\boldsymbol{\varepsilon}_c$ denotes the standard compatible strain computed from the displacement DOFs $\mathbf{d}_e$, corresponding to the compatible displacement approximation, i.e. satisfying the inter-element continuity, while $\boldsymbol{\varepsilon}_i$ denotes the incompatible strain defined by element-wise parameters $\boldsymbol{\alpha}_e$. Using $\boldsymbol{\alpha}_e$ as discrete strain variables, we have a linear dependence

$$\boldsymbol{\varepsilon}_i[\boldsymbol{\alpha}_e] = \mathbf{N}_\alpha \boldsymbol{\alpha}_e$$

also for large deformations, as opposite to the non-linear relationship $\boldsymbol{\varepsilon}_c[\mathbf{d}_e]$. The equations of the DFE with EAS have the same structure of those seen in the previous subsection:

$$\mathbf{s}_e[\mathbf{d}_e, \boldsymbol{\alpha}_e] = \int_{V_e} \left(\mathbf{B}[\mathbf{d}_e, \boldsymbol{\alpha}_e]^T \boldsymbol{\sigma}[\mathbf{d}_e, \boldsymbol{\alpha}_e] \right) dV_e. \tag{4.7}$$

Usually, $\boldsymbol{\alpha}_e$ are defined at element level, so that they can be condensed out before solving the global linear systems of the Newton iterations in the nodal displacements only. It is worth noting that more general EAS methods also exist, where different fields are enhanced. On this aspect, readers are referred to a very recent paper [107] and the references contained therein.

4.2.3 Mixed stress-displacement finite elements

In MFEs, also known as hybrid-stress elements, in addition to the displacement interpolation, an independent approximation of the stress field [108, 100] is introduced:

$$\boldsymbol{\sigma}[\boldsymbol{\xi}] = \mathbf{N}_\sigma[\boldsymbol{\xi}] \boldsymbol{\beta}_e, \tag{4.8}$$

where $\boldsymbol{\beta}_e$ collects the discrete stress DOFs. The Hellinger-Reissner principle can be used to derive the discrete equations of the large deformation FE model when the inverse form of the stress-strain law is available. Instead, when a non-linear constitutive law is given in stress-strain form, it is convenient to derive the problem equations by means of the Hu-Washizu weak form [132, 99, 80]:

$$\begin{aligned} \delta\Pi[\boldsymbol{\sigma}, \mathbf{u}, \boldsymbol{\varepsilon}] = & \int_V \left(\delta\boldsymbol{\varepsilon}^T \left(\boldsymbol{\sigma}[\boldsymbol{\varepsilon}] - \boldsymbol{\sigma} \right) + \delta\boldsymbol{\sigma}^T \left(\boldsymbol{\varepsilon}[\mathbf{u}] - \boldsymbol{\varepsilon} \right) + \delta\boldsymbol{\varepsilon}[\mathbf{u}]^T \boldsymbol{\sigma} \right) dV - \delta W^{\text{ext}} = 0 \\ & \forall \delta\boldsymbol{\sigma}, \delta\mathbf{u}, \delta\boldsymbol{\varepsilon}. \end{aligned} \tag{4.9}$$

In the previous equation, $\boldsymbol{\varepsilon}$ is the independent strain while $\boldsymbol{\varepsilon}[\mathbf{u}]$ denotes the strain computed from the displacement field. Similarly, $\boldsymbol{\sigma}$ is the independent stress while $\boldsymbol{\sigma}[\boldsymbol{\varepsilon}]$ denotes, in a simplified way, the stress computed from any constitutive model in terms of specified strain, strain rate or functional of strain. It is worth noting that the Hu-Washizu formulation allows also the use of independent shape functions for the strain field [97]. However, if we focus on hybrid-stress MFEs, where only stress and displacement fields are directly approximated with independent shape functions, the strain can be defined at the IPs using to compute the integral over the domain. At FE level, we have

$$\begin{aligned} \delta\Pi_e = & \sum_g \left(\delta\boldsymbol{\varepsilon}_g^T \left(\boldsymbol{\sigma}_g[\boldsymbol{\varepsilon}_g] - \mathbf{N}_{\sigma_g} \boldsymbol{\beta}_e \right) + \delta\boldsymbol{\beta}_e^T \mathbf{N}_{\sigma_g}^T \left(\boldsymbol{\varepsilon}_g[\mathbf{d}_e] - \boldsymbol{\varepsilon}_g \right) + \delta\mathbf{d}_e^T \mathbf{B}_g^T \mathbf{N}_{\sigma_g} \boldsymbol{\beta}_e \right) w_g + \\ & - \delta\mathbf{d}_e^T \mathbf{p}_e = \sum_g \delta\boldsymbol{\varepsilon}_g^T \left(\boldsymbol{\sigma}_g[\boldsymbol{\varepsilon}_g] - \mathbf{N}_{\sigma_g} \boldsymbol{\beta}_e \right) w_g + \delta\boldsymbol{\beta}_e^T \left(\boldsymbol{\gamma}_e[\mathbf{d}_e] - \sum_g \mathbf{N}_{\sigma_g}^T \boldsymbol{\varepsilon}_g w_g \right) + \\ & + \delta\mathbf{d}_e^T \mathbf{Q}_e^T \boldsymbol{\beta}_e - \delta\mathbf{d}_e^T \mathbf{p}_e = 0 \qquad \forall \delta\boldsymbol{\beta}, \delta\mathbf{d}, \delta\boldsymbol{\varepsilon}_1, \ldots, \delta\boldsymbol{\varepsilon}_n. \end{aligned} \tag{4.10}$$

In the previous equations, the subscript $g = 1, \ldots, n$ denotes quantities evaluated at the generic IP with weight w_g, vector $\boldsymbol{\gamma}_e$ is the element strain work-conjugate to the element stress DOFs $\boldsymbol{\beta}_e$ and $\mathbf{Q}_e$ is the element tangent compatibility operator:

$$\boldsymbol{\gamma}_e[\mathbf{d}_e] = \sum_g \mathbf{N}_{\sigma_g}^T \boldsymbol{\varepsilon}_g[\mathbf{d}_e] w_g, \tag{4.11}$$

$$\mathbf{Q}_e[\mathbf{d}_e] = \frac{\partial \boldsymbol{\gamma}_e[\mathbf{d}_e]}{\partial \mathbf{d}_e} = \sum_g \mathbf{N}_{\sigma_g}^T \mathbf{B}_g[\mathbf{d}_e] w_g. \tag{4.12}$$

The discrete equations coming from (4.10) for the whole FE model can be written as

$$\text{Global equations} \quad \mathbf{Q}^T \boldsymbol{\beta} - \mathbf{p} = \mathbf{0} \tag{4.13a}$$

$$\text{Element equations} \quad \begin{cases} \boldsymbol{\gamma}_e[\mathbf{d}_e] - \sum_g \mathbf{N}_{\sigma_g}^T \boldsymbol{\varepsilon}_g w_g = \mathbf{0} \\ \boldsymbol{\sigma}_g[\boldsymbol{\varepsilon}_g] - \mathbf{N}_{\sigma_g} \boldsymbol{\beta}_e = \mathbf{0}, \quad \forall g. \end{cases} \tag{4.13b}$$

The global equations state the equilibrium of external load vector $\mathbf{p}$ and internal forces $\mathbf{Q}^T\boldsymbol{\beta}$ computed by assembling the element contribution $\mathbf{Q}_e^T\boldsymbol{\beta}_e$. The first of the element equations (4.13b) links the IP strains $\boldsymbol{\varepsilon}_g$ to the discrete displacements $\mathbf{d}_e$, while the others impose that the stress $\boldsymbol{\sigma}_g[\boldsymbol{\varepsilon}_g]$ at each IP g coming from the constitutive equations must be equal to the stress satisfying the assumed approximation in Eq. (4.8). Since no shape functions are used for the strain field, it is interesting to observe that, when the inverse stress-strain law is available, it is possible to write explicitly $\boldsymbol{\varepsilon}_g$ in terms of $\boldsymbol{\beta}_e$ from the last equations of system (4.13b) and, substituting $\boldsymbol{\varepsilon}_g[\boldsymbol{\beta}_e]$ in the first of (4.13b), the equations of the Hellinger-Reissner formulation are recovered. Therefore, the Hu-Washizu weak form with IP strains can be seen just as a rewriting of the Hellinger-Reissner equations aimed at circumventing the need for the inverse constitutive law $\boldsymbol{\varepsilon}_g[\boldsymbol{\beta}_e]$ by replacing it with an implicit $\boldsymbol{\sigma}_g[\boldsymbol{\varepsilon}_g] = \mathbf{N}_{\sigma_g}\boldsymbol{\beta}_e$.

4.3 Iterative schemes for displacement-based FEs based on mixed integration points

This section discusses the standard Newton method for DFEs, highlighting its deficiency, and proposes a novel MIP Newton method based on independent IP strain that allow to avoid the convergence problems for large rotations and to use standard strain-driven constitutive law for non-linear materials. In order to simplify the discussion, attention is focused on the iterative solution for an assigned load, that is easily generalized to the Riks arc-length analysis.

4.3.1 The Newton scheme in displacement variables

In the general case, the relation between the internal force vector $\mathbf{s}$ and the nodal displacements vector $\mathbf{d}$ is non-linear and an incremental-iterative algorithm is needed to solve the discrete equilibrium Eq. (4.4) in order to trace the equilibrium path. The basic approach in this context consists in using Newton iterations to drive to zero the norm of the residual at each step of the incremental process. Starting from an estimate $\mathbf{d}^j$ of the displacement DOFs at the jth iteration, the residual of the equilibrium Eq. (4.4) is computed as:

$$\mathbf{r}[\mathbf{d}^j] = \mathbf{s}[\mathbf{d}^j] - \mathbf{p}. \tag{4.14}$$

Then, the correction $\dot{\mathbf{d}}$ of the displacement vector is evaluated by solving the linear system

$$\dot{\mathbf{d}} = -\left(\mathbf{K}^j\right)^{-1} \mathbf{r}[\mathbf{d}^j], \tag{4.15}$$

with the tangent stiffness matrix

$$\mathbf{K}^j = \frac{\partial \mathbf{s}[\mathbf{d}]}{\partial \mathbf{d}} |_{\mathbf{d}=\mathbf{d}^j}$$

and the displacements are updated as

$$\mathbf{d}^{j+1} = \mathbf{d}^j + \dot{\mathbf{d}}.$$

The tangent stiffness matrix is computed by assembling the element contributions

$$\mathbf{K}_e[\mathbf{d}_e] \equiv \frac{\partial \mathbf{s}_e[\mathbf{d}_e]}{\partial \mathbf{d}_e} = \int_{V_e} \left(\mathbf{B}[\mathbf{d}_e]^T \mathbf{C}_t \mathbf{B}[\mathbf{d}_e] + \mathbf{G}[\boldsymbol{\sigma}[\mathbf{d}_e], \mathbf{d}_e]\right) dV_e, \tag{4.16}$$

where $\mathbf{C}_t = \dfrac{\partial \boldsymbol{\sigma}}{\partial \boldsymbol{\varepsilon}}$ is the algorithmic tangent constitutive matrix.

The geometric part of the stiffness matrix is computed as

$$\mathbf{G}[\mathbf{d}_e, \boldsymbol{\sigma}[\mathbf{d}_e]] = \sum_k \sigma_k[\mathbf{d}_e] \boldsymbol{\Psi}_k[\mathbf{d}_e] \quad \text{with} \quad \boldsymbol{\Psi}_k[\mathbf{d}_e] \equiv \frac{\partial^2 \varepsilon_k[\mathbf{d}_e]}{\partial \mathbf{d}_e^2}, \tag{4.17}$$

where σ_k and ε_k are the kth component of $\boldsymbol{\sigma}$ and $\boldsymbol{\varepsilon}$ respectively. It is worth noting that the geometric stiffness matrix depends on the stress $\boldsymbol{\sigma}[\mathbf{d}_e]$ computed from the displacements. For large rotations and high stiffness ratios, this displacement-based stress tends to be very inaccurate during the iterations and leads to an inefficient solution that requires a large number of global iterations.

4.3.2 The Newton scheme in displacement and IP strain

A new alternative Newton iterative scheme that improves the convergence for DFEs in large rotation problems is based on the relaxation of the compatibility equations at the level of each integration point during the iterations. At element level, we can rewrite the problem equations as

$$\begin{cases} \mathbf{r}_{g\epsilon} \equiv \boldsymbol{\varepsilon}_g[\mathbf{d}_e] - \boldsymbol{\varepsilon}_g, \quad \forall g \\ \mathbf{r}_d \equiv \displaystyle\sum_{g=1}^{n} (\mathbf{B}_g[\mathbf{d}_e]^T \boldsymbol{\sigma}_g[\boldsymbol{\varepsilon}_g] w_g) - \mathbf{p}_e, \end{cases} \tag{4.18}$$

where, from now on, $\boldsymbol{\varepsilon}_g$ denotes the independent strain at the gth IP, $\boldsymbol{\varepsilon}_g[\mathbf{d}_e]$ is the strain coming from the displacement DOFs through the compatibility equations and $\boldsymbol{\sigma}_g[\boldsymbol{\varepsilon}_g]$ is the stress computed from the independent strain through any constitutive law. Compared to the MIP method in stress and displacement [83], the proposed one is more suitable for non-linear material laws that are usually available in strain-driven form. The two methods coincide in linear elasticity, but the new one is not derived from a Hellinger-Reissner principle, circumventing the need for an inverse stress-strain law through independent IP strains. Interestingly, the relaxation of the compatibility equations at the IPs is sufficient to give to DFEs the enhanced efficiency and robustness observed in MFEs and original MIP method both based on independent stress.

The differentiation of (4.18) gives

$$\begin{aligned} &\frac{\partial \mathbf{r}_{g\epsilon}}{\partial \boldsymbol{\varepsilon}_g} = -\mathbf{I} \qquad &&\frac{\partial \mathbf{r}_{g\epsilon}}{\partial \mathbf{d}_e} = \mathbf{B}_g[\mathbf{d}_e] \\ &\frac{\partial \mathbf{r}_d}{\partial \boldsymbol{\varepsilon}_g} = \mathbf{B}_g[\mathbf{d}_e]^T \mathbf{C}_{tg} w_g \qquad &&\frac{\partial \mathbf{r}_d}{\partial \mathbf{d}_e} = \sum_{g=1}^{n} \mathbf{G}_g[\mathbf{d}_e, \boldsymbol{\sigma}_g[\boldsymbol{\varepsilon}_g]] w_g, \end{aligned} \tag{4.19}$$

where the IP contribution to the geometric stiffness $\mathbf{G}_g$ is now a function of the stress computed from the independent strain $\boldsymbol{\varepsilon}_g$, instead of that coming from the displacements as in the standard scheme. It is worth noting that also the algorithmic tangent constitutive matrix $\mathbf{C}_{tg}$ is evaluated using the independent strain just like $\boldsymbol{\sigma}_g[\boldsymbol{\varepsilon}_g]$. The linear system in Eq. (4.15) to be solved at each global iteration becomes, at the element level,

$$\begin{bmatrix} -\mathbf{I} & & & \mathbf{B}_1 \\ & \ddots & & \vdots \\ & & -\mathbf{I} & \mathbf{B}_n \\ \mathbf{B}_1[\mathbf{d}_e]^T \mathbf{C}_{t1} w_1 & \dots & \mathbf{B}_n[\mathbf{d}_e]^T \mathbf{C}_{tn} w_n & \sum_g^n \mathbf{G}_g w_g \end{bmatrix}^j \begin{bmatrix} \dot{\boldsymbol{\varepsilon}}_1 \\ \vdots \\ \dot{\boldsymbol{\varepsilon}}_n \\ \dot{\mathbf{d}}_e \end{bmatrix} = \begin{bmatrix} \mathbf{0} \\ \vdots \\ \mathbf{0} \\ \mathbf{p}_e \end{bmatrix} - \begin{bmatrix} \mathbf{r}_{1\epsilon} \\ \vdots \\ \mathbf{r}_{n\epsilon} \\ \sum_g^n \left(\mathbf{B}_g^T \boldsymbol{\sigma}_g[\boldsymbol{\varepsilon}_g] w_g\right), \end{bmatrix}^j \tag{4.20}$$

where the superscript on matrices denotes that they are evaluated at the current estimate of the jth iteration.

By performing a static condensation of the strain $\dot{\boldsymbol{\varepsilon}}_g$, locally defined at the level of the IP, we obtain

$$\dot{\boldsymbol{\varepsilon}}_g = \mathbf{B}_g^j \dot{\mathbf{d}}_e + \mathbf{r}_{g\epsilon}^j = \mathbf{B}_g^j \dot{\mathbf{d}}_e + \boldsymbol{\varepsilon}_g[\mathbf{d}_e^j] - \boldsymbol{\varepsilon}_g^j, \tag{4.21}$$

that substituted in the last of Eq. (4.20) gives

$$\mathbf{K}_e[\mathbf{d}_e^j, \boldsymbol{\varepsilon}_1^j, \ldots, \boldsymbol{\varepsilon}_n^j]\dot{\mathbf{d}}_e = -\mathbf{r}_e[\mathbf{d}_e^j, \boldsymbol{\varepsilon}_1^j, \ldots, \boldsymbol{\varepsilon}_n^j], \tag{4.22}$$

with the condensed tangent stiffness matrix

$$\mathbf{K}_e[\mathbf{d}_e^j, \boldsymbol{\varepsilon}_1^j, \ldots, \boldsymbol{\varepsilon}_n^j] = \sum_{g=1}^{n} \left(\mathbf{B}_g[\mathbf{d}_e^j]^T \mathbf{C}_{tg} \mathbf{B}_g[\mathbf{d}_e^j] + \mathbf{G}_g[\mathbf{d}_e^j, \boldsymbol{\varepsilon}_g^j] \right) w_g. \tag{4.23}$$

This matrix has the same form as the classical displacement-based one (4.16). However, this time, it depends on the independent strain at the integration points, which is directly predicted and corrected during the iterations. The condensed residual vector is

$$\mathbf{r}_e[\mathbf{d}_e^j, \boldsymbol{\varepsilon}_1^j, \ldots, \boldsymbol{\varepsilon}_n^j] = \mathbf{s}_e[\mathbf{d}_e^j, \boldsymbol{\varepsilon}_1^j, \ldots, \boldsymbol{\varepsilon}_n^j] - \mathbf{p}_e,$$

with the condensed internal forces

$$\mathbf{s}_e[\mathbf{d}_e^j, \boldsymbol{\varepsilon}_1^j, \ldots, \boldsymbol{\varepsilon}_n^j] = \sum_{g}^{n} \left(\mathbf{B}_g^{j\,T} \boldsymbol{\sigma}_g[\boldsymbol{\varepsilon}_g^j] + \mathbf{B}_g[\mathbf{d}_e^j]^T \mathbf{C}_{tg} (\boldsymbol{\varepsilon}_g[\mathbf{d}_e^j] - \boldsymbol{\varepsilon}_g^j) \right) w_g.$$

These coincide with the internal forces of the displacement-based formulation in Eq. (4.5) at each iteration in case of linear material law but only at the converged equilibrium point for non-linear materials.

The linear system in Eq. (4.22) is solved at global level after a standard FE assemblage so obtaining $\dot{\mathbf{d}}$. The strain corrections $\dot{\boldsymbol{\varepsilon}}_g$ are then retrieved by local back-substitutions.

4.3.3 Comparison of the different schemes for DFEs

The two iterative schemes for DFEs are compared in Tab. 4.1. It is clear that the cost of the iteration for the two methods is exactly the same, since the global condensed residual and tangent stiffness matrix have the same size (only displacement DOFs). The difference is only that the MIP Newton $\mathbf{d}$-$\boldsymbol{\varepsilon}$ performs a direct initial estimate of the independent IP strain as $\boldsymbol{\varepsilon}_g^1 = \boldsymbol{\varepsilon}_{g(k)} + \Delta\boldsymbol{\varepsilon}_g$, with $\boldsymbol{\varepsilon}_{g(k)}$ the known value at the previous equilibrium state k and $\Delta\boldsymbol{\varepsilon}_g$ taken along the path tangent or extrapolated from previous equilibrium points as for the displacement, and a direct correction of the IP strain according to Eq. (4.21). This solves the iterative issue of the standard Newton for structures with high stiffness ratios and, at the same time, permits a simple use of strain-driven constitutive laws. Finally, the equilibrium curve provided by the two methods is identical. Only the iterative burden changes. The other implementation details of the incremental-iterative analysis are those reported in 1.1.2.

	Newton d	**Newton d-ε**
Predictor	$\mathbf{d}^1 = \mathbf{d}_{(k)} + \Delta\mathbf{d}$	$\mathbf{d}^1 = \mathbf{d}_{(k)} + \Delta\mathbf{d}$ $\boldsymbol{\varepsilon}_g^1 = \boldsymbol{\varepsilon}_{g(k)} + \Delta\boldsymbol{\varepsilon}_g$
Iteration matrix	$\mathbf{K}[\mathbf{d}^j]$	$\mathbf{K}[\mathbf{d}^j, \boldsymbol{\varepsilon}_1^j, \ldots, \boldsymbol{\varepsilon}_n^j]$
Residual vector	$\mathbf{s}[\mathbf{d}^j] - \mathbf{p}$	$\mathbf{s}[\mathbf{d}^j, \boldsymbol{\varepsilon}_1^j, \ldots, \boldsymbol{\varepsilon}_n^j] - \mathbf{p}$
New estimate	$\mathbf{d}^{j+1} = \mathbf{d}^j + \dot{\mathbf{d}}$	$\mathbf{d}^{j+1} = \mathbf{d}^j + \dot{\mathbf{d}}$ $\boldsymbol{\varepsilon}_g^{j+1} = \boldsymbol{\varepsilon}_g^j + \dot{\boldsymbol{\varepsilon}}$

Table 4.1: Schematic description of the principal points of the algorithms for DFEs for obtaining a new equilibrium point $k+1$ within an incremental analysis: The differences between the standard Newton and the Newton in displacement and IP strain are marked in blue.

4.4 Iterative schemes for mixed stress-displacement FEs

This section discusses three possible iterative schemes for MFEs, highlighting for each of them pros and cons. The first one is a Newton scheme in displacement only, with the element stress DOFs written as a function of the nodal displacements. The second one is the extension to the large deformation case of the one proposed in [132], where nodal displacements, element stress DOFs and IP strain are considered as independent variables in the linearization. The third one is a novel scheme where nodal displacements and element strains work-conjugate to the element stress DOFs are the primal variables of the iteration. The global residual and iteration matrix has the same size for all the three methods, since only displacement variables are maintained at global level.

4.4.1 The Newton scheme in displacement variables

The equations of mixed stress-displacement FEs can be solved with a purely displacement-based iteration scheme by driving to zero the norm of the residual force vector

$$\mathbf{r}[\mathbf{d}] = \mathbf{s}[\mathbf{d}] - \mathbf{p}, \tag{4.24}$$

with the global internal force vector $\mathbf{s}$ obtained by assembling the element contributions

$$\mathbf{s}_e[\mathbf{d}_e] = \mathbf{Q}_e[\mathbf{d}_e]^T \boldsymbol{\beta}_e[\mathbf{d}_e]. \tag{4.25}$$

where the discrete stress parameters $\boldsymbol{\beta}_e[\mathbf{d}_e]$ are obtained at element level by solving the element state equations (4.13b) for the assigned $\mathbf{d}_e$ [80]. The procedure, known as element state determination, for computing $\boldsymbol{\beta}_e[\mathbf{d}_e]$ and $\boldsymbol{\varepsilon}_g[\mathbf{d}_e]$ with $g = 1, \ldots, n$ requires at each global equilibrium iteration the solution of an element-wise non-linear system by local Newton iterations:

$$\text{prescribed} \quad \mathbf{d}_e, \quad \text{find} \quad \boldsymbol{\beta}_e, \boldsymbol{\varepsilon}_1, \ldots, \boldsymbol{\varepsilon}_n \quad \text{such that} \quad \begin{cases} \boldsymbol{\gamma}_e[\mathbf{d}_e] - \sum_g \mathbf{N}_{\sigma_g} \boldsymbol{\varepsilon}_g w_g = \mathbf{0} \\ \boldsymbol{\sigma}_g[\boldsymbol{\varepsilon}_g] - \mathbf{N}_{\sigma_g} \boldsymbol{\beta}_e = \mathbf{0}, \quad \forall g. \end{cases} \tag{4.26}$$

The implicit differentiation of the element state Eq. (4.26) with respect to $\mathbf{d}_e$

$$\begin{cases} \mathbf{Q}_e - \sum_g \mathbf{N}_{\sigma_g}^T \dfrac{\partial \boldsymbol{\varepsilon}_g}{\partial \mathbf{d}_e} w_g = \mathbf{0} \\ \mathbf{C}_{tg} \dfrac{\partial \boldsymbol{\varepsilon}_g}{\partial \mathbf{d}_e} - \mathbf{N}_{\sigma_g} \dfrac{\partial \boldsymbol{\beta}_e}{\partial \mathbf{d}_e} = \mathbf{0}, \quad \forall g. \end{cases} \tag{4.27}$$

provides

$$\frac{\partial \boldsymbol{\beta}_e}{\partial \mathbf{d}_e} = \mathbf{H}_{et}^{-1}\mathbf{Q}_e \quad \text{with} \quad \mathbf{H}_{et} = \sum_g \mathbf{D}_g^T \mathbf{C}_{tg}^{-1} \mathbf{N}_{\sigma_g} w_g \tag{4.28}$$

where $\mathbf{H}_{et}$ is the algorithmic element tangent compliance matrix. A global Newton scheme in displacements gives the correction $\dot{\mathbf{d}}$ of the displacement vector $\mathbf{d}^j$ at the jth global iteration by solving the linear system

$$\dot{\mathbf{d}} = -\left(\mathbf{K}^j\right)^{-1} \mathbf{r}[\mathbf{d}^j], \tag{4.29}$$

with the tangent stiffness matrix

$$\mathbf{K}^j = \frac{\partial \mathbf{s}[\mathbf{d}]}{\partial \mathbf{d}} \,|_{\mathbf{d}=\mathbf{d}_j}$$

The displacements are then updated as

$$\mathbf{d}^{j+1} = \mathbf{d}^j + \dot{\mathbf{d}}.$$

The tangent stiffness matrix is computed by assembling the element contributions

$$\mathbf{K}_e[\mathbf{d}_e] \equiv \frac{\partial \mathbf{s}_e[\mathbf{d}_e]}{\partial \mathbf{d}_e} = \mathbf{Q}[\mathbf{d}_e]^T \mathbf{H}_{et}^{-1} \mathbf{Q}[\mathbf{d}_e] + \boldsymbol{\Gamma}[\mathbf{d}_e, \boldsymbol{\beta}_e[\mathbf{d}_e]] \tag{4.30}$$

with

$$\boldsymbol{\Gamma}[\mathbf{d}_e, \boldsymbol{\beta}_e[\mathbf{d}_e]] = \int_{V_e} \left(\mathbf{G}[\mathbf{d}_e, \boldsymbol{\sigma}[\boldsymbol{\beta}_e[\mathbf{d}_e]]]\right) dV_e.$$

This displacement-based approach is very similar to a standard Newton for DFEs. The differences are that the converged solution can be made locking-free by the assumed stress shape functions and an iterative element state determination (Eq. (4.13b)) is required at each global iteration. Strain-driven constitutive laws are easily considered. As the standard Newton for DFEs, this scheme is affected by iterative difficulties for slender structures because of the term $\boldsymbol{\beta}_e[\mathbf{d}_e]$ in the geometric stiffness (Eq. (4.30)).

4.4.2 The Newton scheme in stress, strain and displacement

An interesting alternative iterative scheme is obtained by directly linearizing all problem equations in system (4.13), that at element level can be written as

$$\begin{cases} \mathbf{r}_d \equiv \mathbf{Q}_e[\mathbf{d}_e]^T \boldsymbol{\beta}_e - \mathbf{p}_e = \mathbf{0} \\ \mathbf{r}_\epsilon \equiv \mathbf{Q}_e[\mathbf{d}_e]\mathbf{d}_e - \sum_g \mathbf{N}_{\sigma_g}^T \boldsymbol{\varepsilon}_g w_g = \mathbf{0} \\ \mathbf{r}_g \equiv \boldsymbol{\sigma}_g[\boldsymbol{\varepsilon}_g] - \mathbf{N}_{\sigma_g}\boldsymbol{\beta}_e = \mathbf{0}, \quad \forall g, \end{cases} \tag{4.31}$$

with respect to $\boldsymbol{\beta}_e$, $\mathbf{d}_e$ and $\boldsymbol{\varepsilon}_g$. The linearized incremental form at element level from the current estimates of the jth iteration is

$$\begin{cases} \mathbf{Q}_e[\mathbf{d}_e^j]^T \dot{\boldsymbol{\beta}}_e + \boldsymbol{\Gamma}[\boldsymbol{\beta}_e^j, \mathbf{d}_e^j]\dot{\mathbf{d}}_e = -\mathbf{r}_d^j \\ \mathbf{Q}_e[\mathbf{d}_e^j]\dot{\mathbf{d}}_e - \sum_g \mathbf{N}_{\sigma_g}^T \dot{\boldsymbol{\varepsilon}}_g^j w_g = -\mathbf{r}_\epsilon^j \\ \mathbf{C}_{tg}\dot{\boldsymbol{\varepsilon}}_g - \mathbf{D}_g \dot{\boldsymbol{\beta}}_e = -\mathbf{r}_g^j, \quad \forall g. \end{cases} \tag{4.32}$$

The solution of this linear system gives the corrections needed for the Newton update

$$\begin{cases} \boldsymbol{\varepsilon}_g^{j+1} = \boldsymbol{\varepsilon}_g^j + \dot{\boldsymbol{\varepsilon}}_g \\ \boldsymbol{\beta}_e^{j+1} = \boldsymbol{\beta}_e^j + \dot{\boldsymbol{\beta}}_e \\ \mathbf{d}_e^{j+1} = \mathbf{d}_e^j + \dot{\mathbf{d}}_e, \end{cases} \tag{4.33}$$

that can be obtained at global level after a local condensation of $\dot{\boldsymbol{\beta}}_e$ and $\dot{\boldsymbol{\varepsilon}}_g$. From the third of Eq. (4.32) we obtain

$$\dot{\boldsymbol{\varepsilon}}_g = \mathbf{C}_{tg}^{-1}(\mathbf{N}_{\sigma_g}\dot{\boldsymbol{\beta}}_e - \mathbf{r}_g^j), \tag{4.34}$$

and, substituting into the second one,

$$\dot{\boldsymbol{\beta}}_e = \mathbf{H}_{et}^{-1}(\mathbf{Q}[\mathbf{d}_e^j]\dot{\mathbf{d}}_e + \tilde{\boldsymbol{\gamma}}_e) \quad \text{with} \quad \begin{cases} \mathbf{H}_{et} = \sum_g \mathbf{D}_g^T\mathbf{C}_{tg}^{-1}\mathbf{N}_{\sigma_g} w_g \\ \tilde{\boldsymbol{\gamma}}_e = \sum_g \mathbf{D}_g^T\mathbf{C}_{tg}^{-1}\mathbf{r}_g^j w_g + \mathbf{r}_\epsilon^j. \end{cases} \tag{4.35}$$

Using Eq. (4.34) and Eq. (4.35), the linearized equilibrium equations (the first of Eq. (4.32)) become

$$\mathbf{Q}_e[\mathbf{d}_e^j]^T\mathbf{H}_{et}^{-1}(\mathbf{Q}_e[\mathbf{d}_e^j]\dot{\mathbf{d}}_e + \tilde{\boldsymbol{\gamma}}_e) + \boldsymbol{\Gamma}[\boldsymbol{\beta}_e^j, \mathbf{d}_e^j]\dot{\mathbf{d}}_e = -\mathbf{r}_d^j.$$

Defining the condensed tangent stiffness matrix of the element as

$$\mathbf{K}_e[\mathbf{d}_e, \boldsymbol{\beta}_e, \boldsymbol{\varepsilon}_1, \ldots, \boldsymbol{\varepsilon}_n] = \mathbf{Q}_e[\mathbf{d}_e]^T\mathbf{H}_{et}^{-1}\mathbf{Q}_e[\mathbf{d}_e] + \boldsymbol{\Gamma}[\mathbf{d}_e, \boldsymbol{\beta}_e],$$

the condensed form of the linearized equilibrium equations, in the only unknown $\dot{\mathbf{d}}_e$, is:

$$\mathbf{K}_e^j\dot{\mathbf{d}}_e = -\mathbf{r}_e^j \quad \text{with} \quad \mathbf{r}_e = \mathbf{r}_d + \mathbf{Q}_e[\mathbf{d}_e]^T\mathbf{H}_{et}^{-1}\tilde{\boldsymbol{\gamma}}_e \tag{4.36}$$

The linear system in Eq. (4.36) is solved at global level after a standard FE assemblage for $\dot{\mathbf{d}}$, while $\dot{\boldsymbol{\beta}}_e$ and $\dot{\boldsymbol{\varepsilon}}_g$ are then retrieved by local back-substitutions. In doing this, it is possible to note that the condensed residual can be subdivided, exploiting the definition of $\mathbf{r}_d$ in Eq. (4.31), as $\mathbf{r}_e = \mathbf{s}_e - \mathbf{p}_e$, with the condensed internal forces computed in this scheme as

$$\mathbf{s}_e[\mathbf{d}_e, \boldsymbol{\beta}_e \boldsymbol{\varepsilon}_1, \ldots, \boldsymbol{\varepsilon}_n] = \mathbf{Q}_e[\mathbf{d}_e]^T\boldsymbol{\beta}_e + \mathbf{Q}_e[\mathbf{d}_e]^T\mathbf{H}_{et}^{-1}\tilde{\boldsymbol{\gamma}}_e. \tag{4.37}$$

It is worth noting that both the condensed stiffness matrix $\mathbf{K}_e$ and the condensed internal forces $\mathbf{s}_e$ of the element depends on the IP strains $\boldsymbol{\varepsilon}_1, \ldots, \boldsymbol{\varepsilon}_n$, since $\mathbf{C}_{tg}$, $\mathbf{r}_g$ and $\mathbf{r}_\epsilon$ depend on them. This scheme has two main advantages compared to the one seen in the previous subsection: i) the independent correction of the stress avoids the increase of global iterations for high stiffness ratios; ii) the element state equations are solved together with the global equilibrium, so avoiding multiple local iterations at element level for each global one. Its only drawback is the possible increase of global iterations when the material non-linearity is predominant over the geometric one.

4.4.3 The Newton scheme in strain and displacement

Another possibility is now presented with the aim of avoiding the drawback of the previous scheme. The idea is to relax the element compatibility equations $\boldsymbol{\gamma}_e[\mathbf{d}_e]$ introducing the generalized strain $\boldsymbol{\gamma}_e$ work-conjugate of the stress DOFs as independent variable. The element equations are rewritten as

$$\begin{cases} \mathbf{r}_\gamma \equiv \boldsymbol{\gamma}_e[\mathbf{d}_e] - \boldsymbol{\gamma}_e \\ \mathbf{r}_d \equiv \mathbf{Q}_e[\mathbf{d}_e]^T\boldsymbol{\beta}_e[\boldsymbol{\gamma}_e] - \mathbf{p}_e \end{cases} \tag{4.38}$$

where the stress DOFs $\boldsymbol{\beta}_e[\boldsymbol{\gamma}_e]$ are obtained from the element state equations (4.13b) for the assigned $\boldsymbol{\gamma}_e$ instead of $\boldsymbol{\gamma}_e[\mathbf{d}_e]$ coming from the assigned displacement. The element state determination for computing $\boldsymbol{\beta}_e[\boldsymbol{\gamma}_e]$ requires at each global equilibrium iteration the solution of an element-wise non-linear system by local Newton iterations:

$$\text{prescribed} \quad \boldsymbol{\gamma}_e, \quad \text{find} \quad \boldsymbol{\beta}_e, \boldsymbol{\varepsilon}_1, \ldots, \boldsymbol{\varepsilon}_n \quad \text{such that} \quad \begin{cases} \boldsymbol{\gamma}_e - \sum_g \mathbf{N}_{\sigma_g}^T\boldsymbol{\varepsilon}_g w_g = \mathbf{0} \\ \boldsymbol{\sigma}_g[\boldsymbol{\varepsilon}_g] - \mathbf{N}_{\sigma_g}\boldsymbol{\beta}_e = \mathbf{0}, \quad \forall g. \end{cases} \tag{4.39}$$

The differentiation of (4.38) gives

$$\begin{aligned} \frac{\partial \mathbf{r}_\gamma}{\partial \boldsymbol{\gamma}_e} &= -\mathbf{I} & \frac{\partial \mathbf{r}_\gamma}{\partial \mathbf{d}_e} &= \mathbf{Q}_e[\mathbf{d}_e] \\ \frac{\partial \mathbf{r}_d}{\partial \boldsymbol{\gamma}_e} &= \mathbf{Q}_e[\mathbf{d}_e]^T \mathbf{H}_{et}^{-1} & \frac{\partial \mathbf{r}_d}{\partial \mathbf{d}_e} &= \boldsymbol{\Gamma}_e[\mathbf{d}_e, \boldsymbol{\sigma}_g[\boldsymbol{\beta}_e[\boldsymbol{\gamma}_e]]], \end{aligned} \tag{4.40}$$

where the geometric stiffness matrix $\boldsymbol{\Gamma}_e$ is now a function of the displacement DOFs and of the independent element strain $\boldsymbol{\gamma}_e$. The linear system of the Newton iteration, at the element level, becomes

$$\begin{bmatrix} -\mathbf{I} & \mathbf{Q}_e[\mathbf{d}_e] \\ \mathbf{Q}_e[\mathbf{d}_e]^T \mathbf{H}_{et}^{-1} & \boldsymbol{\Gamma}_e[\mathbf{d}_e, \boldsymbol{\gamma}_e] \end{bmatrix}^j \begin{bmatrix} \dot{\boldsymbol{\gamma}}_e \\ \dot{\mathbf{d}}_e \end{bmatrix} = \begin{bmatrix} \mathbf{0} \\ \mathbf{p}_e \end{bmatrix} - \begin{bmatrix} \mathbf{r}_\gamma \\ \mathbf{Q}_e[\mathbf{d}_e]^T \boldsymbol{\beta}_e[\boldsymbol{\gamma}_e] \end{bmatrix}^j \tag{4.41}$$

where the superscript on the quantities denotes that they are evaluated during the iterative process with the current estimate of $\boldsymbol{\gamma}_e$ and $\mathbf{d}_e$.

By performing a static condensation of the strains $\dot{\boldsymbol{\gamma}}_e$, locally defined at the element level, we obtain

$$\dot{\boldsymbol{\gamma}}_e = \mathbf{Q}_e^j \dot{\mathbf{d}}_e + \mathbf{r}_\gamma^j = \mathbf{Q}_e^j \dot{\mathbf{d}}_e + \boldsymbol{\gamma}_e[\mathbf{d}_e^j] - \boldsymbol{\gamma}_e^j \tag{4.42}$$

that, substituted in the last of Eq. (4.41), gives

$$\mathbf{K}_e[\mathbf{d}_e^j, \boldsymbol{\gamma}_e^j] \dot{\mathbf{d}}_e = -\mathbf{r}_e[\mathbf{d}_e^j, \boldsymbol{\gamma}_e^j] \tag{4.43}$$

with

$$\mathbf{K}_e[\mathbf{d}_e, \boldsymbol{\gamma}_e] = \mathbf{Q}_e[\mathbf{d}_e]^T \mathbf{H}_{et}^{-1} \mathbf{Q}_e[\mathbf{d}_e] + \boldsymbol{\Gamma}_e[\mathbf{d}_e, \boldsymbol{\gamma}_e] \tag{4.44}$$

the condensed tangent stiffness matrix, that has the same form as the displacement-based iteration matrix in Eq. (4.30). However, this time, it also depends on the independent generalized strain of the element, which are now directly predicted and corrected during the iterations. The condensed residual vector is

$$\mathbf{r}_e[\mathbf{d}_e, \boldsymbol{\gamma}_e] = \mathbf{s}_e[\mathbf{d}_e, \boldsymbol{\gamma}_e] - \mathbf{p}_e$$

with the condensed internal forces

$$\mathbf{s}_e[\mathbf{d}_e, \boldsymbol{\gamma}_e] = \mathbf{Q}_e[\mathbf{d}_e]^T \boldsymbol{\beta}_e[\boldsymbol{\gamma}_e] + \mathbf{Q}_e[\mathbf{d}_e]^T \mathbf{H}_{et}^{-1} (\boldsymbol{\gamma}_e[\mathbf{d}_e] - \boldsymbol{\gamma}_e)$$

which reduce to the displacement-based internal forces $\mathbf{Q}_e[\mathbf{d}_e]^T \boldsymbol{\beta}_e[\mathbf{d}_e]$ of the scheme in subsection 4.4.1 for linear elastic material during the iterations, but only at the converged point for generally non-linear materials.

This scheme is a good compromise that avoids: i) the iterative difficulties of the scheme in subsection 4.4.1 for slender structures since the geometric stiffness is evaluated with the stress coming from the independent $\boldsymbol{\gamma}_e$; ii) the growth of the global iterations for material-dominated non-linearity of the scheme in subsection 4.4.2 because the element state equations, and then also the constitutive law, are closed at each global iteration. Compared to the scheme in subsection 4.4.2 local iterations are needed at element level to determinate the element state, but this is rewarded by the general reduction of global iterations for relevant material non-linearities.

4.4.4 Comparison of the different schemes for MFEs

The three iterative schemes described in this section are briefly summarized in Tab. 4.2 in order to highlight the main differences. The Newton in displacements only suffers from an increase of global iterations for slender structures undergoing large rotations. This issue is solved by both the alternative schemes, where further independent variables are considered. The Newton $\mathbf{d}$-$\boldsymbol{\beta}$-$\boldsymbol{\varepsilon}$, in addition to nodal displacements, performs an independent initial estimate of element stress DOFs and IP strain in the predictor stage along the path tangent or as extrapolation of previous equilibrium states ($\Delta\boldsymbol{\beta}$, $\Delta\boldsymbol{\varepsilon}_g$) and a direct correction according to Eq. (4.34) and Eq. (4.35). It eliminates also the local iterations to determine the element state but may suffer from an increase of global iterations for significant material non-linearity. The Newton $\mathbf{d}$-$\boldsymbol{\gamma}$ uses an initial estimate of the element strain $\boldsymbol{\gamma}_e$ from the previous equilibrium points independent of the displacements and a direct correction according to (4.42). This scheme is the most robust choice for large rotations and widespread material non-linearity. All the schemes have global residual and tangent stiffness matrix with the same size, due to the condensation of the local variables, and provide the same final equilibrium curve. For the implementation details of the incremental-iterative see Section 1.1.2.

	Newton d	**Newton d-$\boldsymbol{\beta}$-$\boldsymbol{\varepsilon}$**	**Newton d-$\boldsymbol{\gamma}$**
Predictor	$\mathbf{d}^1 = \mathbf{d}_{(k)} + \Delta\mathbf{d}$	$\mathbf{d}^1 = \mathbf{d}_{(k)} + \Delta\mathbf{d}$ $\boldsymbol{\varepsilon}_g^1 = \boldsymbol{\varepsilon}_{g(k)} + \Delta\boldsymbol{\varepsilon}_g$ $\boldsymbol{\beta}^1 = \boldsymbol{\beta}_{(k)} + \Delta\boldsymbol{\beta}$	$\mathbf{d}^1 = \mathbf{d}_{(k)} + \Delta\mathbf{d}$ $\boldsymbol{\gamma}^1 = \boldsymbol{\gamma}_{(k)} + \Delta\boldsymbol{\gamma}$
Local FE iterations	$\boldsymbol{\beta}_e[\mathbf{d}_e^j]$	–	$\boldsymbol{\beta}_e[\boldsymbol{\gamma}_e^j]$
Iteration matrix	$\mathbf{K}[\mathbf{d}^j, \boldsymbol{\beta}[\mathbf{d}^j]]$	$\mathbf{K}[\mathbf{d}^j, \boldsymbol{\beta}^j, \boldsymbol{\varepsilon}_1^j, \dots, \boldsymbol{\varepsilon}_N^j]$	$\mathbf{K}[\mathbf{d}^j, \boldsymbol{\beta}[\boldsymbol{\gamma}^j]]$
Residual vector	$\mathbf{s}[\mathbf{d}^j] - \mathbf{p}$	$\mathbf{s}[\mathbf{d}^j, \boldsymbol{\beta}^j, \boldsymbol{\varepsilon}_1^j, \dots, \boldsymbol{\varepsilon}_N^j] - \mathbf{p}$	$\mathbf{s}[\mathbf{d}^j, \boldsymbol{\beta}[\boldsymbol{\gamma}^j]] - \mathbf{p}$
New estimate	$\mathbf{d}^{j+1} = \mathbf{d}^j + \dot{\mathbf{d}}$	$\mathbf{d}^{j+1} = \mathbf{d}^j + \dot{\mathbf{d}}$ $\boldsymbol{\varepsilon}_g^{j+1} = \boldsymbol{\varepsilon}_g^j + \dot{\boldsymbol{\varepsilon}}_g$ $\boldsymbol{\beta}_e^{j+1} = \boldsymbol{\beta}_e^j + \dot{\boldsymbol{\beta}}_e$	$\mathbf{d}^{j+1} = \mathbf{d}^j + \dot{\mathbf{d}}$ $\boldsymbol{\gamma}_e^{j+1} = \boldsymbol{\gamma}_e^j + \dot{\boldsymbol{\gamma}}_e$

Table 4.2: Schematic description of the principal points of the algorithms for MFEs for obtaining a new equilibrium point $k+1$ within an incremental analysis: The differences between the displacement-based Newton and the alternative schemes are marked in red and blue.

4.5 Structural models and finite elements

The excellent performances of the proposed iterative strategies with respect to the Newton method in displacements only hold for any structural model and FE implementation. However, in this section, some details about these aspects are provided, in order to make the numerical tests presented in the next section completely reproducible. In particular the structural models considered are chosen to be as simple and general as possible: i) 2D frames, based on the Reissner geometrically exact beam model; ii) 3D shells, based on a solid-shell FE model and the Green-Lagrange strain measure. A Total Lagrangian formulation is chosen for both the models, even if other formulations can be easily employed. The elasto-plastic constitutive law is integrated by a Backward Euler method with an additive split of the strain in elastic and plastic part under the assumption of large deformations but small strains [14, 16].

4.5.1 Model and discretization for beam structures

The 2D beam model

The 2D beam model is based on the geometrically exact Reissner-Antman [114, 3] strain measure

$$\boldsymbol{\varepsilon} = \begin{bmatrix} e \\ \gamma \\ \chi \end{bmatrix} \quad \text{with} \quad \begin{cases} e = (1 + u,_s) \cos\varphi + w,_s \sin\varphi - 1 \\ \gamma = -(1 + u,_s) \sin\varphi + w,_s \cos\varphi \\ \chi = \varphi,_s \end{cases} \tag{4.45}$$

where u, w, φ are, respectively, the axial displacement, the transversal displacement and the rotation, functions of the abscissa along the beam axis s. The constitutive law is assumed elastic for the shear part, i.e. the shear force is $T = GAr\gamma$, where G is the shear modulus, A

is the cross-section area, r is the shear correction factor. An elastic-perfectly plastic material law is used for the normal stress-normal strain law on the section by means of a fiber approach [80]. The relationship between rate of normal stress σ and rate of normal strain ϵ in each fiber is defined by the Young modulus E and the yield function $f(\sigma) \equiv |\sigma| - \sigma_y \leq 0$ with σ_y the yield stress. The backward Euler scheme is adopted for the integration in each step of the path-following analysis. The axial force N and the bending moment M of the section are then computed by integrating σ over the section, so obtaining the generalized stress vector $\boldsymbol{\sigma} \equiv \begin{bmatrix} N & T & M \end{bmatrix}^T$.

The displacement-based beam element with assumed strain

The FE is assumed to be straight. The approximation of u, w, φ is based on a 3 node quadratic Lagrangian interpolation. The nodes are located at the ends and at the midspan of the element. The interpolation of u, w, φ is introduced in Eq. (4.45) so obtaining the discrete strain-displacement relationship in Eq. (4.2). Two Gauss integration points could be used to evaluate the internal force vector and the stiffness matrix for a locking-free discretization. However, an odd Gauss-Lobatto rule would be more suitable to capture the inelastic behavior at the end-sections. Nevertheless, the direct use of a Gauss-Lobatto rule, e.g. with 3 points, makes the element prone to shear and membrane locking. Note that the latter occurs also for initially straight elements in large deformation problems. To avoid this inconvenience, we adopt an assumed strain strategy. In practice, the discrete strain-displacement law is redefined as

$$\boldsymbol{\varepsilon}_{AS}[\mathbf{d}_e, s] = \left(1 - \frac{s - s_1}{s_2 - s_1}\right) \boldsymbol{\varepsilon}_1[\mathbf{d}_e] + \frac{s - s_1}{s_2 - s_1} \boldsymbol{\varepsilon}_2[\mathbf{d}_e], \tag{4.46}$$

where $\boldsymbol{\varepsilon}_1$ and $\boldsymbol{\varepsilon}_2$ are standard displacement-based strains evaluated at the 2 Gauss points. Using this assumed strain technique, we have now a locking-free strain along the whole element axis and 3 Gauss-Lobatto points are used for the numerical integration of internal forces and tangent stiffness matrix in order to include the end-sections. The formulation remains purely displacement-based with no extra variables.

The mixed stress-displacement beam element

Another possibility to avoid locking is the use of a mixed stress-displacement formulation. In this case, beside the displacement field, also the stress resultants and moment are directly approximated along the beam axis as

$$\boldsymbol{\sigma}[s] = \begin{bmatrix} N \\ T \\ M \end{bmatrix} = \mathbf{N}_\sigma[s] \boldsymbol{\beta}_e \quad \text{with} \quad \mathbf{N}_\sigma[s] = \begin{bmatrix} \frac{1-s}{2} & 0 & 0 & \frac{1+s}{2} & 0 & 0 \\ 0 & \frac{1-s}{2} & 0 & 0 & \frac{1+s}{2} & \\ 0 & 0 & \frac{1-s}{2} & 0 & 0 & \frac{1+s}{2} \end{bmatrix} \tag{4.47}$$

with $s \in [-1; 1]$. It is worth noting the stress interpolation is discontinuous across elements, so that the 6 discrete stress DOFs $\boldsymbol{\beta}_e$ are internal variables of the element. The chosen stress approximation is able to recover the exact equilibrium for zero distributed loads and small displacements, while for large deformations it provides just a locking-free solution. Moreover, an odd Gauss-Lobatto rule can be directly used to impose the constitutive law also at the end-sections.

4.5.2 Model and discretization for shells

For the shell structures a solid-shell element is used. However, iterative schemes are applicable to other shell models [137, 56, 65].

The displacement-based solid-shell element with ANS and EAS

This solid-shell element is an improved version of the displacement-based hexahedron proposed in [131] by means of EAS. It is adopted here in a Total Lagrangian formulation based on a Green-Lagrange strain measure. Denoting with $\boldsymbol{\xi} = \{\xi, \eta, \zeta\}$ the convective coordinates used to express the FE interpolation, the current configuration is described by the reference position vector $\mathbf{X}[\boldsymbol{\xi}] \equiv \{X[\boldsymbol{\xi}], Y[\boldsymbol{\xi}], Z[\boldsymbol{\xi}]\}$ and by the displacement field $\mathbf{u}[\boldsymbol{\xi}]$. Adopting the convention of summing on repeated indexes, the covariant Green-Lagrange strain measure components are

$$\bar{E}_{ij} = \frac{1}{2}\left(\mathbf{X},_i \cdot \mathbf{u},_j + \mathbf{u},_i \cdot \mathbf{X},_j + \mathbf{u},_i \cdot \mathbf{u},_j\right) \quad \text{with} \quad i,j = \xi, \eta, \zeta \tag{4.48}$$

where a comma followed by k denotes the derivative with respect to k and $(\cdot)$ denotes the scalar product. The position vector of a point inside the element and its displacement are interpolated, using a trilinear 8-node brick element, as

$$\mathbf{X}[\boldsymbol{\xi}] = \mathbf{N}_d[\boldsymbol{\xi}]\mathbf{X}_e, \qquad \mathbf{u}[\boldsymbol{\xi}] = \mathbf{N}_d[\boldsymbol{\xi}]\mathbf{d}_e, \tag{4.49}$$

where vectors $\mathbf{d}_e$ and $\mathbf{X}_e$ collect the element nodal displacements and coordinates and matrix $\mathbf{N}_d[\boldsymbol{\xi}]$ the trilinear interpolation functions. Adopting a Voigt notation the Green-Lagrange covariant strain components in Eq.(4.48) are collected in vector $\bar{\mathbf{E}} \equiv [\bar{E}_{\xi\xi}, \bar{E}_{\eta\eta}, 2\bar{E}_{\xi\eta}, \bar{E}_{\zeta\zeta}, 2\bar{E}_{\eta\zeta}, 2\bar{E}_{\xi\zeta}]^T$ that, exploiting Eq.(4.49), becomes

$$\bar{\mathbf{E}} = \left(\boldsymbol{\mathcal{L}}[\boldsymbol{\xi}] + \frac{1}{2}\boldsymbol{\mathcal{Q}}[\boldsymbol{\xi}, \mathbf{d}_e]\right)\mathbf{d}_e. \tag{4.50}$$

In order to circumvent shear and trapezoidal lockings, the natural transverse normal strain $\bar{E}_{\zeta\zeta}$ and the shear strains $\bar{E}_{\xi\zeta}, \bar{E}_{\eta\zeta}$ are redefined by the *assumed natural strain* (ANS) technique [120, 68, 12], assuming from now on that the Z-axis and the X-Y-plane are parallel to the ζ-axis and mid-surface of the shell respectively. The covariant strains can be linearized with respect to ζ in the following form

$$\bar{\mathbf{E}} \approx \begin{bmatrix} \bar{\mathbf{e}}[\xi,\eta] + \zeta\, \bar{\boldsymbol{\chi}}[\xi,\eta] \\ \bar{E}_{\zeta\zeta}[\xi,\eta] \\ \bar{\boldsymbol{\gamma}}[\xi,\eta] \end{bmatrix} \tag{4.51}$$

where

$$\bar{\mathbf{e}}[\xi,\eta] \equiv \begin{bmatrix} \bar{E}_{\xi\xi} \\ \bar{E}_{\eta\eta} \\ 2\bar{E}_{\xi\eta} \end{bmatrix}_{\zeta=0} \qquad \bar{\boldsymbol{\chi}}[\xi,\eta] \equiv \begin{bmatrix} \bar{E}_{\xi\xi},_\zeta \\ \bar{E}_{\eta\eta},_\zeta \\ 2\bar{E}_{\xi\eta},_\zeta \end{bmatrix}_{\zeta=0} \qquad \bar{\boldsymbol{\gamma}}[\xi,\eta] \equiv \begin{bmatrix} 2\bar{E}_{\eta\zeta} \\ 2\bar{E}_{\xi\zeta} \end{bmatrix}_{\zeta=0}.$$

The generalized covariant strains can be collected in vector $\bar{\boldsymbol{\varepsilon}}_c$ as

$$\bar{\boldsymbol{\varepsilon}}_c[\xi,\eta] \equiv \begin{bmatrix} \bar{\mathbf{e}} \\ \bar{E}_{\zeta\zeta} \\ \bar{\boldsymbol{\chi}} \\ \bar{\boldsymbol{\gamma}} \end{bmatrix} = \left(\boldsymbol{\mathcal{L}}_\varepsilon[\xi,\eta] + \frac{1}{2}\boldsymbol{\mathcal{Q}}_\varepsilon[\xi,\eta,\mathbf{d}_e]\right)\mathbf{d}_e, \tag{4.52}$$

where matrix $\boldsymbol{\mathcal{L}}_\varepsilon$ and $\boldsymbol{\mathcal{Q}}_\varepsilon$ are defined from Eq.(4.50) and the ANS modification, so obtaining the operator in Eq.(4.2).

In order to improve the approximation for coarse meshes, an incompatible part of the generalized strains is added to the compatible part as

$$\boldsymbol{\varepsilon}[\mathbf{d}_{ec}, \boldsymbol{\alpha}_e] = \boldsymbol{\varepsilon}_c[\mathbf{d}_{ec}] + \boldsymbol{\varepsilon}_i[\boldsymbol{\alpha}_e] = \boldsymbol{\varepsilon}_c[\mathbf{d}_{ec}] + \mathbf{N}_\alpha \boldsymbol{\alpha}_e \tag{4.53}$$

where

$$\mathbf{N}_\alpha = \begin{bmatrix} \mathbf{N}_{e\alpha} & \mathbf{0}_{3\times4} \\ \mathbf{0}_{1\times4} & \mathbf{0}_{1\times4} \\ \mathbf{0}_{3\times4} & \mathbf{N}_{e\alpha} \\ \mathbf{0}_{2\times4} & \mathbf{0}_{2\times4} \end{bmatrix} \quad \text{with} \quad \mathbf{N}_{e\alpha} = \begin{bmatrix} \xi & 0 & 0 & 0 \\ 0 & \eta & 0 & 0 \\ 0 & 0 & \xi & \eta \end{bmatrix}.$$

It is worth noting that the first 4 internal variables in $\boldsymbol{\alpha}_e$ play a relevant role in improving the membrane response. On the contrary, the second 4 variables in $\boldsymbol{\alpha}_e$ give just a slight improvement of the out-of-plane response.

Finally the generalized Cartesian strains are obtained from the natural ones as

$$\boldsymbol{\varepsilon} = \mathbf{T}\bar{\boldsymbol{\varepsilon}} \tag{4.54}$$

where matrix $\mathbf{T}$ depends on the components of matrix $\mathbf{J} = \begin{bmatrix}\mathbf{X}_{,1} & \mathbf{X}_{,2} & \mathbf{X}_{,3}\end{bmatrix}^T$ as explicitly reported in [131]. The work-conjugated generalized stresses are

$$\boldsymbol{\sigma} \equiv \left[\boldsymbol{\mathcal{N}}, s_z, \boldsymbol{\mathcal{M}}, \boldsymbol{\mathcal{T}}\right]^T \tag{4.55}$$

with

$$\begin{aligned} \boldsymbol{\mathcal{N}} &\equiv \frac{1}{2}\int_{-1}^{1}\begin{bmatrix}S_{xx}\\ S_{yy}\\ S_{xy}\end{bmatrix} d\zeta \quad & \boldsymbol{\mathcal{M}} &\equiv \frac{1}{2}\int_{-1}^{1}\zeta\begin{bmatrix}S_{xx}\\ S_{yy}\\ S_{xy}\end{bmatrix} d\zeta \\ s_z &\equiv \frac{1}{2}\int_{-1}^{1} S_{zz} d\zeta & \boldsymbol{\mathcal{T}} &\equiv \frac{1}{2}\int_{-1}^{1}\begin{bmatrix}S_{xz}\\ S_{yz}\end{bmatrix} d\zeta \end{aligned} \tag{4.56}$$

and $\mathbf{S}$ is the second Piola-Kirchhoff stress tensor. Note that, all the generalized stresses are defined for simplicity with the unit of stress, also $\boldsymbol{\mathcal{M}}$.

The linear elastic generalized constitutive matrix $\mathbf{C}$ is evaluated starting from the constitutive law $\mathbf{S} = \mathbb{C}\mathbf{E}$, performing an analytic pre-integration of $\mathbb{C}$ along the thickness direction and assuming a constant with Z stress S_{zz} instead of a constant thickness strain E_{zz}, in order to eliminate the thickness locking, following the approach proposed in [131]. An elastic-perfectly plastic behavior with associated flow rule is adopted. It is defined in terms of generalized stresses using the following yield function

$$f(\boldsymbol{\sigma}) \equiv \boldsymbol{\mathcal{N}}^T\mathbf{Y}\boldsymbol{\mathcal{N}} + 4\boldsymbol{\mathcal{M}}^T\mathbf{Y}\boldsymbol{\mathcal{M}} - \sigma_y^2 \leq 0 \quad \text{with} \quad \mathbf{Y} = \begin{bmatrix}1 & -\frac{1}{2} & 0\\ -\frac{1}{2} & 1 & 0\\ 0 & 0 & 3\end{bmatrix}$$

that is one of the simplest approximation in stress resultants of the Von Mises criterion, exact for pure membrane solicitations as well as for pure bending (see [116, 13]). The backward Euler scheme leading to the closest point projection is used to integrate the constitutive law. A 2×2 grid of integration points on the middle plane of the shell is used to evaluate the internal force vector and the stiffness matrix.

The same format of the equations holds for other displacement-based solid-shell elements [140].

The mixed stress-displacement solid-shell element with ANS

The mixed stress-displacement solid-shell element is obtained according to [131]. The kinematics is described as in the displacement-based case. The EAS is not introduced, since the direct interpolation of the stress field yields practically the same results. Only the ASN for the thickness strain is maintained to avoid trapezoidal locking. The generalized contravariant stresses can be interpolated as in [108, 131]:

$$\bar{\boldsymbol{\sigma}}[\xi, \eta] = \bar{\mathbf{N}}_\sigma[\boldsymbol{\xi}]\boldsymbol{\beta}_e \tag{4.57}$$

where $\boldsymbol{\beta}_e$ collects the 18 stress parameters. Then, the generalized Cartesian stresses are obtained from the contravariant ones as

$$\boldsymbol{\sigma} = \mathbf{T}_\sigma\bar{\boldsymbol{\sigma}} = \mathbf{N}_\sigma[\xi, \eta]\boldsymbol{\beta}_e \quad \text{with} \tag{4.58}$$

$$\mathbf{T}_\sigma = \mathbf{T}^{-T}[0, 0] \qquad \mathbf{N}_\sigma[\xi, \eta] = \mathbf{T}_\sigma\bar{\mathbf{N}}_\sigma.$$

Note that stresses are transformed with the matrix $\mathbf{T}^{-T}$ evaluated at $\xi = 0, \eta = 0$ in order to preserve the constant stress state. Other transformations are also possible [139].

4.6 Numerical Tests

The iterative schemes are tested in this section for beams/frames and shells discretized using displacement-based and mixed elements. The structural models and the finite element discretization described in the previous section are adopted. The following iterative schemes are considered:

- $DF-\mathbf{d}$: Displacement-based FE with only nodal displacements as independent variables in the iterative solution;
- $DF-\mathbf{d}\boldsymbol{\varepsilon}$: Displacement-based FE with nodal displacements and strains at the IPs as independent variables in the iterative solution;
- $DF-\mathbf{d}\boldsymbol{\alpha}$: Displacement-based FE improved by EAS with nodal displacements and EAS DOFs as independent variables in the iterative solution;
- $DF-\mathbf{d}\boldsymbol{\alpha}\boldsymbol{\varepsilon}$: Displacement-based FE improved by EAS with nodal displacements, EAS DOFs and strains at the IPs as independent variables in the iterative solution;
- $MF-\mathbf{d}$: Mixed stress-displacement FE with only nodal displacements as independent variables in the iterative solution;
- $MF-\mathbf{d}\boldsymbol{\beta}\boldsymbol{\varepsilon}$: Mixed stress-displacement FE with nodal displacements, discrete stress DOFs and strains at the IPs as independent variables in the iterative solution;
- $MF-\mathbf{d}\boldsymbol{\gamma}$: Mixed stress-displacement FE with nodal displacements and strains work-conjugate to the discrete stress DOFs as independent variables in the iterative solution.

Quasi-static analyses are considered with a reference load vector amplified by a load proportionality factor λ. A Riks arc-length method is used to obtain the equilibrium paths, using the same settings for all the iterative schemes. The complete implementation details are those reported in 1.1.2, for reproducibility purpose. The numerical tests will focus on the global iterative burden needed to compute the equilibrium curves. It is worth remembering that the schemes $MF-\mathbf{d}$ and $MF-\mathbf{d}\boldsymbol{\gamma}$ require also local FE iterations to determinate the element state at each global (structural) iteration. However, the element state determination is very efficient requiring an average number of about 2 local iterations for each global one in all the examined elastoplastic tests, in agreement with that reported in [80] for small deformation analyses. This makes the local iterative burden negligible in the overall computational cost dominated, especially for fine meshes, by the factorization of the global iteration matrix.

4.6.1 Beam tests

Eulero beam

The first test regards the compressed beam represented in Fig. 4.1. The cross section has a rectangular shape 0.1×1. The analytical critical load P_{crit} of the perfect beam is given by

$$P_{crit} = \frac{\pi^2 EJ}{L^2},$$

where E is the material young modulus, J is the moment of inertia of the cross section and L is the beam length. A transverse force F_{imp} is added to the model as imperfection:

$$F_{imp} = \frac{P_{crit}}{200\pi^2}.$$

The strength of the materials is assumed as $\sigma_y = 5 \cdot 10^5/L$ in order to have the same shape of the equilibrium path for all L. The beam is modeled using 8 FEs. The analysis is carried out for both DFEs and MFEs with different values of the length L. Results are reported in Fig. ??, where the normalized vertical displacement component at the midspan of the

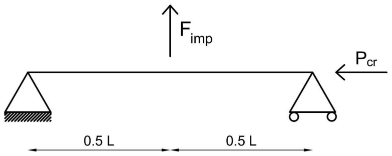

Figure 4.1: Eulero beam: geometry, load and boundary conditions.

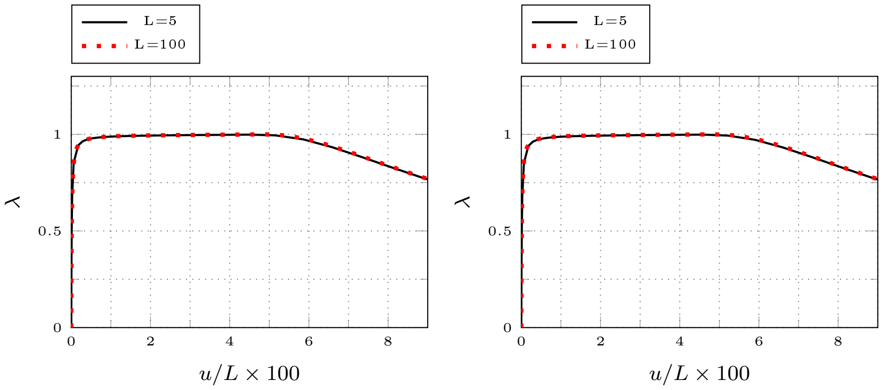

Displacement-based element

Mixed element

Eulero beam: equilibrium path in terms of load factor and normalized vertical displacement component at the midspan varying the length L for displacement-based and mixed elements.

beam is plotted against the load multipler. We can note that the two formulations provide practically the same curve, characterized by a limit point due to the plastic hinge arising in the post-buckling path. The total global iterations for the different schemes are reported in Tab. 4.3. We can observe that the schemes based on displacement variables $DF-\mathbf{d}$ and $MF-\mathbf{d}$ are affected by an increase of the iterative burden with L. Instead, $DF-\mathbf{d}\boldsymbol{\varepsilon}$, $MF-\mathbf{d}\boldsymbol{\beta}\boldsymbol{\varepsilon}$ and $MF-\mathbf{d}\boldsymbol{\gamma}$ need an almost constant value of total iterations. $DF-\mathbf{d}\boldsymbol{\varepsilon}$ is then the best option for the displacement formulation, while, $MF-\mathbf{d}\boldsymbol{\beta}\boldsymbol{\varepsilon}$ is the most efficient choice for mixed element since, compared to $MF-\mathbf{d}\boldsymbol{\gamma}$, it needs just one evaluation of the IP stress resultants at each global iteration.

Roorda Frame

Let us consider the Roorda frame represented in Fig. 4.3. The beam cross section is the same described in the previous test as well as the yield stress. The exact critical load P_{crit} of the perfect structure is given by

$$P_{crit}=\frac{1.406\pi^2 EJ}{L^2}.$$

The force F_{imp} represents the imperfection applied to the structure:

$$F_{imp}=\frac{EJ}{10^4 L^2}.$$

L	$DF-\mathbf{d}$	$DF-\mathbf{d}\boldsymbol{\varepsilon}$	$MF-\mathbf{d}$	$MF-\mathbf{d}\boldsymbol{\beta}\boldsymbol{\varepsilon}$	$MF-\mathbf{d}\boldsymbol{\gamma}$
5	129	116	128	118	118
10	128	105	129	107	106
20	135	109	135	112	112
50	152	109	161	112	112
100	178	109	186	112	111

Table 4.3: Eulero beam: total global iterations for the different schemes varying the length L.

L	$DF-\mathbf{d}$	$DF-\mathbf{d}\varepsilon$	$MF-\mathbf{d}$	$MF-\mathbf{d}\beta\varepsilon$	$MF-\mathbf{d}\gamma$
5	133	110	134	111	110
10	144	108	147	108	108
20	156	107	156	106	106
50	196	107	195	108	108
100	234	107	234	107	108

Table 4.4: Roorda frame: total global iterations for the different schemes varying the length L for positive imperfection.

Two different tests are performed for positive and negative values of the imperfection F_{imp}. The length of the members varies from 5 to 100. Each of them is modeled using 8 elements. The strength of the materials is assumed as in the previous test.

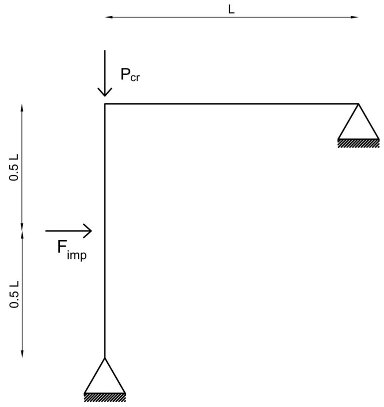

Figure 4.3: Roorda frame: geometry, load and boundary conditions.

The first test compares the accuracy of DFEs and MFEs. Their equilibrium curves are reported in Fig.4.4, where the normalized horizontal displacement at the imperfection point is monitored. Practically, the same results are obtained with the two formulations for every value of the length L and for both positive and negative imperfection.

The second test concerns the global iterative burden with the different schemes: $DF-\mathbf{d}$ and $DF-\mathbf{d}\varepsilon$ for DFEs; $MF-\mathbf{d}$, $MF-\mathbf{d}\beta\varepsilon$ and $MF-\mathbf{d}\gamma$ for MFEs. Tables 4.4 and 4.5 show the total global iterations for each test concerning positive and negative imperfection respectively. The $DF-\mathbf{d}\varepsilon$ scheme needs a lower number of iterations than the basic $DF-\mathbf{d}$ one and this difference becomes more and more evident as the length L increases. Indeed, the total number of iterations is almost the same for every length for $DF-\mathbf{d}\varepsilon$, while $DF-\mathbf{d}$ shows a significant increment of the iterations with L. The same considerations can be made for MFEs: the scheme $MF-\mathbf{d}$ requires a number of iteration increasing with L, while $MF-\mathbf{d}\beta\varepsilon$ and $MF-\mathbf{d}\gamma$ avoid this issue with similar performances. Also, $DF-\mathbf{d}\varepsilon$, $MF-\mathbf{d}\beta\varepsilon$ and $MF-\mathbf{d}\gamma$ behave very similarly in terms of iterations.

Multi-story frame

A frame structure with two spans and six stories is now taken under consideration. Cross sections, geometry and loads are depicted in Fig. 4.5. The material parameters are $E = 205$ and $\sigma_y = 235$. A convergence test in terms of number of FEs used for each beam and column is reported in Fig. 4.6, where the equilibrium curves are referred to the horizontal displacement of the top left node of the frame. The MFEs in stress-displacement exhibit a superior accuracy since 2 elements are sufficient to approximate well the solution. Instead, 8 DFEs are required to obtain similar results.

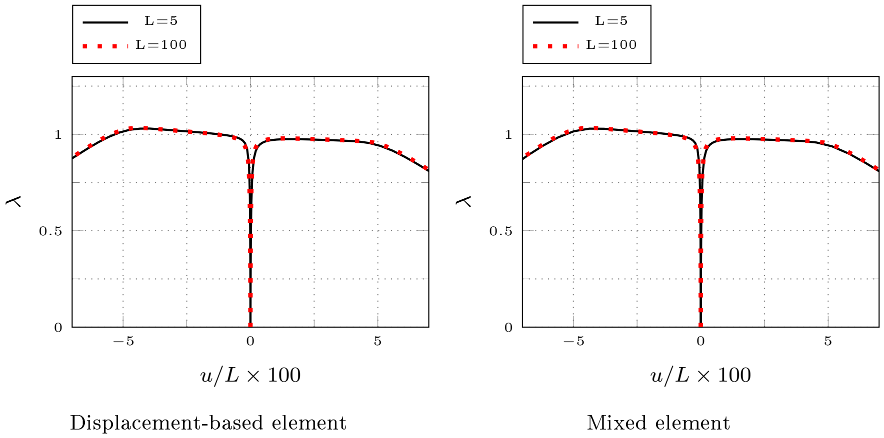

Figure 4.4: Roorda frame: equilibrium path in terms of load factor and normalized horizontal displacement at the imperfection point varying the length L and the imperfection sign for displacement-based and mixed elements.

L	$DF-\mathbf{d}$	$DF-\mathbf{d}\varepsilon$	$MF-\mathbf{d}$	$MF-\mathbf{d}\beta\varepsilon$	$MF-\mathbf{d}\gamma$
5	141	115	148	115	116
10	151	112	153	114	113
20	166	106	167	108	107
50	203	113	203	114	114
100	250	112	255	114	115

Table 4.5: Roorda frame: total global iterations for the different schemes varying the length L for negative imperfection.

The total global iterations for the different schemes are reported in Tab. 4.6 considering the finest mesh for the two formulations used in Fig. 4.6. $DF-\mathbf{d}\varepsilon$ gives the lowest number of iterations. $MF-\mathbf{d}\beta\varepsilon$ and $MF-\mathbf{d}\gamma$ succeed in reducing the total global iteration almost by half, with respect to the basic $MF-\mathbf{d}$ approach.

4.6.2 Shell tests

Lipped channel column undergoing global and local buckling

A lipped channel column, modeled as a multi-patch shell structure, under pressure load is now considered [25]. Geometry and load conditions are depicted in Fig. 4.7. The cross-sectional in-plane displacements are constrained at both ends. The elastic properties are $E = 210000$, $\nu = 0.3$ and σ_y varies from 235 to a theoretical infinite value. This structure suffers from global-local buckling interaction with unstable post-buckling, which makes it highly imperfection sensitive. In order to take it into account, an imperfection is applied to the structure which combines a global and a local mode shapes. The combination is given by:

$$\tilde{\mathbf{d}}[\theta_1] = \cos\theta_1 \tilde{\mathbf{d}}_1 + \sin\theta_1 \tilde{\mathbf{q}}_2 \quad \text{with} \quad 0 \le \theta_1 < 2\pi$$

where $\tilde{\mathbf{d}}_1$ and $\tilde{\mathbf{d}}_2$ are the displacement shapes of the first and second linearized buckling mode respectively and $\theta_1 = 0.58$ is the angle giving the worst imperfection shape in terms of

$DF-\mathbf{d}$	$DF-\mathbf{d}\varepsilon$	$MF-\mathbf{d}$	$MF-\mathbf{d}\beta\varepsilon$	$MF-\mathbf{d}\gamma$
184	134	261	141	150

Table 4.6: Multi-story frame: total global iterations for the different schemes.

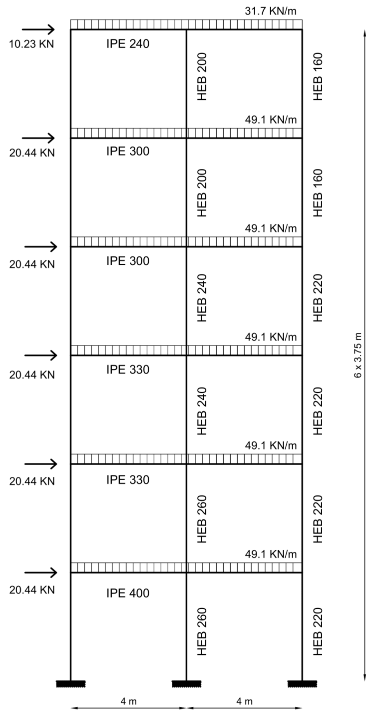

Figure 4.5: Multi-story frame: geometry, loads and boundary conditions.

σ_y	$DF - \mathbf{d}\boldsymbol{\alpha}$	$DF - \mathbf{d}\boldsymbol{\alpha}\boldsymbol{\varepsilon}$	$MF - \mathbf{d}\boldsymbol{\beta}\boldsymbol{\varepsilon}$	$MF - \mathbf{d}\boldsymbol{\gamma}$
235	135	93	118	110
355	120	80	82	76
520	111	78	77	78
$\to \infty$	100	77	77	77

Table 4.7: Lipped channel: total global iterations for the different schemes varying the yield stress.

critical load reduction [81]. The linearized buckling modes $\tilde{\mathbf{d}}_1$ and $\tilde{\mathbf{d}}_2$ and the corresponding critical loads are shown in Fig. 4.8. Three different meshes are considered as reported in Fig. 4.9. In the same figure, a detail on the interface modeling for non-smooth intersections using the solid-shell elements is also illustrated. In particular, the equivalent solid mesh seen in the beam cross-section is characterized by interface elements with a trapezoidal shape to impose the continuity. The ANS redefinition of the covariant thickness strain avoids trapezoidal locking. Figure 4.10 compares the accuracy of DFEs with EAS and MFEs for $\sigma_y = 235$. The equilibrium paths reported are referred to the maximum displacement component. Almost identical results can be observed for the two discrete formulations.

Figure 4.11 shows that a very similar accuracy is given by DFEs with EAS and MFEs also for different values of the yield stress σ_y, considering the second mesh (Fig. 4.9). The total number of iterations required by the different schemes is given in Tab. 4.7, varying also the yield stress. $DF - \mathbf{d}\boldsymbol{\alpha}$ needs the highest number of iterations, while $DF - \mathbf{d}\boldsymbol{\alpha}\boldsymbol{\varepsilon}$ allows to save about one third of the computational time. $MF - \mathbf{d}\boldsymbol{\beta}\boldsymbol{\varepsilon}$ and $MF - \mathbf{d}\boldsymbol{\gamma}$ behave similarly for this test.

U-shape cantilever beam

The U-shaped cantilever beam represented in Fig. 4.12 is now considered, with Young modulus $E = 7 \times 10^6$, Poisson ratio $\nu = 0.3$ and thickness $t = 1$. It was analyzed in a

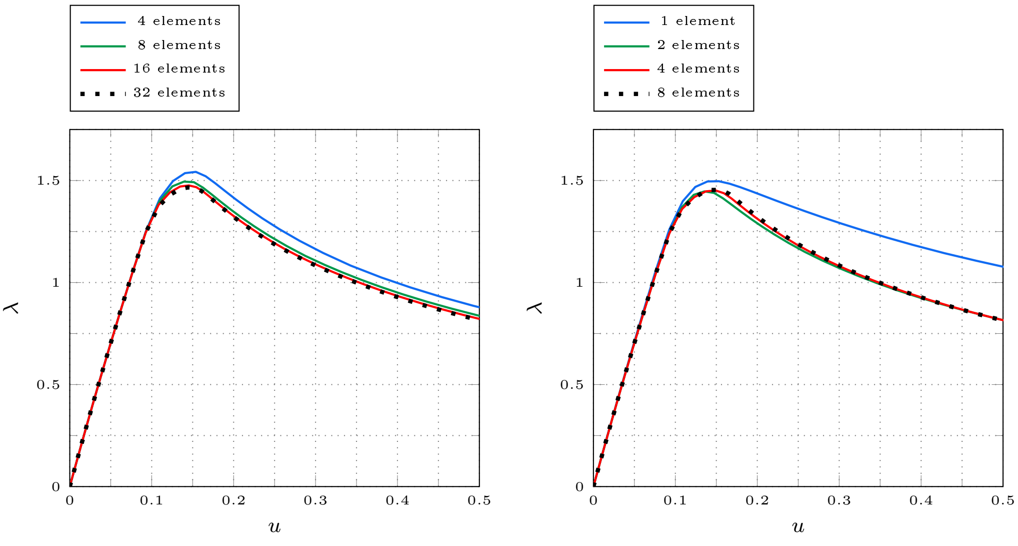

Displacement-based element

Mixed element

Figure 4.6: Multi-story frame: convergence of the equilibrium path in terms of load factor and horizontal displacement of the top left node varying the mesh for displacement-based and mixed elements.

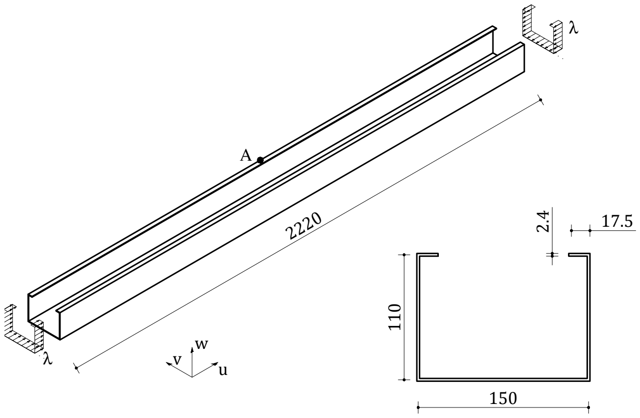

Figure 4.7: Lipped channel: geometry and load.

large number of articles [69, 74]. A mesh convergence test is carried out considering the meshes reported in Fig. 4.13. An almost identical convergence rate is highlighted for both DFEs with EAS and MFEs, comparing the equilibrium path for the maximum displacement component. Figure 4.15 shows a similar accuracy with the second mesh also varying the yield stress value. In Tab. 4.8 the iterations required by the various schemes to trace these paths are reported. $MF - \mathbf{d}\boldsymbol{\gamma}$ shows the lowest number of total iterations, followed very closely by $DF - \mathbf{d}\boldsymbol{\alpha\varepsilon}$. These two schemes exhibit robustness with respect to the material non-linearity, with a limited increase of iterations as the plastic effects become more and more important. The basic scheme $DF - \mathbf{d}\boldsymbol{\alpha}$ performs the worst regardless of σ_y. $MF - \mathbf{d}\boldsymbol{\beta\varepsilon}$ is similar to $MF - \mathbf{d}\boldsymbol{\gamma}$ and $DF - \mathbf{d}\boldsymbol{\alpha\varepsilon}$ in the elastic case, but much less efficient when the material non-linearity occurs.

Semi-cylinder

A semi-cylindrical structure is now considered. Geometry, load and boundary conditions are illustrated in Fig. 4.16. The Young modulus of the material is $E = 2068.50$ and the

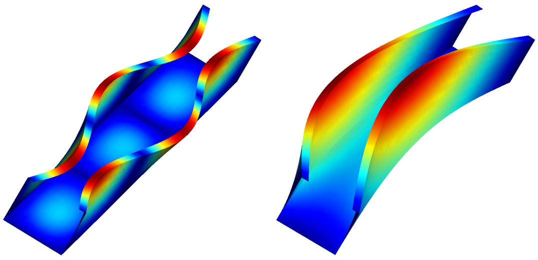

$\lambda_1 = 0.503$ $\lambda_2 = 0.504$

Figure 4.8: Lipped channel: first linearized buckling loads and corresponding modes of the perfect structure used as imperfection basis.

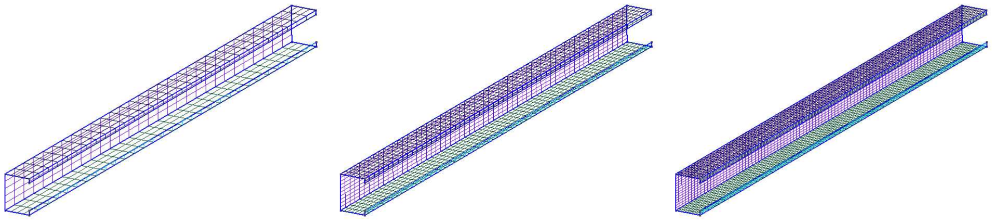

Mesh 1 Mesh 2 Mesh 3

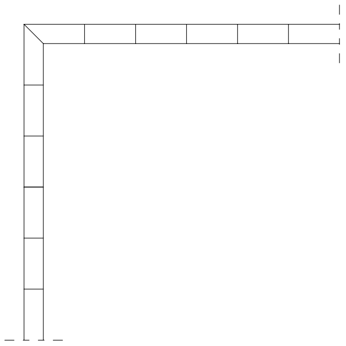

Intersection modelling

Figure 4.9: Lipped channel: meshes adopted in the analysis.

Poisson ratio is $\nu = 0.3$. Only half of the structure is discretized exploiting the symmetry using the meshes depicted in Fig. 4.17. Figure 4.18 shows a mesh convergence test comparing the equilibrium curves in terms of the maximum displacement component. DFEs with EAS and MFEs have practically the same accuracy for every mesh. The same equilibrium paths are provided by the two formulations also varying the yield stress, as shown in Fig. 4.19 for the second mesh. Finally, Tab. 4.9 provides the total global iterations to obtain those curve using the different iterative methods. The standard $DF - \mathbf{d}\boldsymbol{\alpha}$ requires many iterations in both elastic and elastoplastic case. $DF - \mathbf{d}\boldsymbol{\alpha}\boldsymbol{\varepsilon}$, $MF - \mathbf{d}\boldsymbol{\beta}\boldsymbol{\varepsilon}$ and $MF - \mathbf{d}\boldsymbol{\gamma}$ need the same iterations in the elastic case, but the performance of $MF - \mathbf{d}\boldsymbol{\beta}\boldsymbol{\varepsilon}$ deteriorates in the elasto-plastic one. Instead, $DF - \mathbf{d}\boldsymbol{\alpha}\boldsymbol{\varepsilon}$ and $MF - \mathbf{d}\boldsymbol{\gamma}$ are very robust also for the non-linear material.

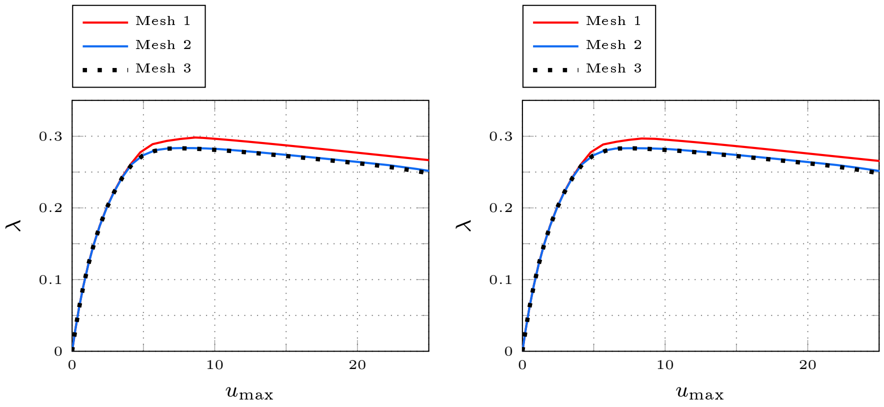

Displacement-based element with EAS

Mixed element

Figure 4.10: Lipped channel: convergence of the equilibrium path in terms of load factor and maximum displacement component for $\sigma_y = 235$ varying the mesh for displacement-based elements with EAS and mixed elements.

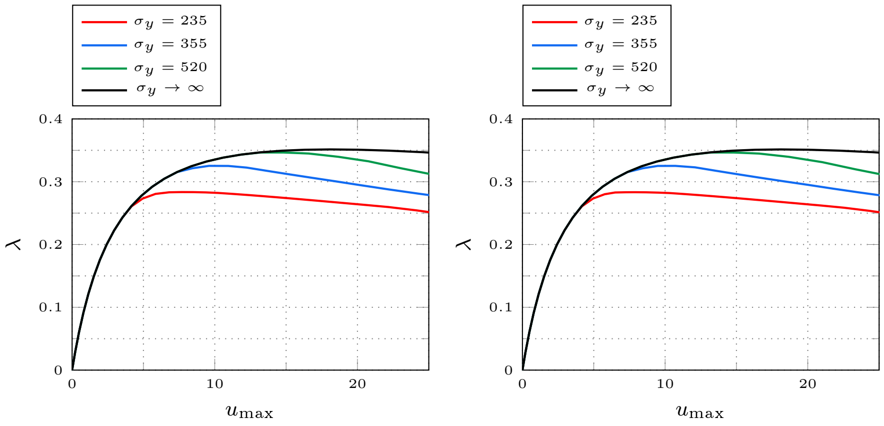

Displacement-based element with EAS

Mixed element

Figure 4.11: Lipped channel: equilibrium path in terms of load factor and maximum displacement component for $\sigma_y = 235 - 355 - 520$ and $\sigma_y \to \infty$ using the second mesh with both displacement-based elements with EAS and mixed elements.

σ_y	$DF - \mathbf{d}\boldsymbol{\alpha}$	$DF - \mathbf{d}\boldsymbol{\alpha\varepsilon}$	$MF - \mathbf{d}\boldsymbol{\beta\varepsilon}$	$MF - \mathbf{d}\boldsymbol{\gamma}$
2500	170	70	140	62
5000	136	72	161	52
$\to \infty$	112	51	66	51

Table 4.8: U-shape cantilever beam: total global iterations for the different schemes varying the yield stress.

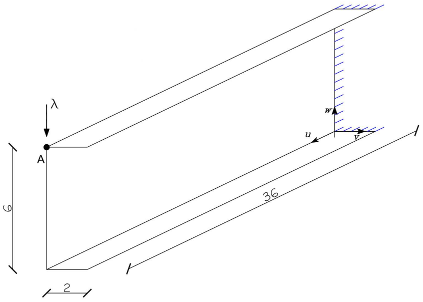

Figure 4.12: U-shape cantilever beam: geometry, load and boundary conditions.

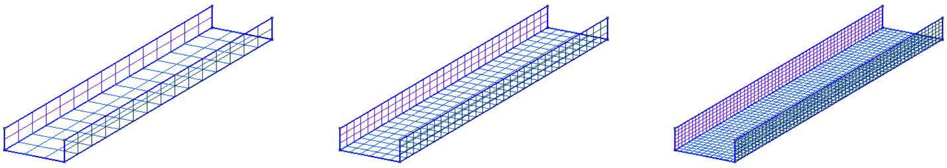

Mesh 1 Mesh 2 Mesh 3

Figure 4.13: U-shape cantilever beam: meshes adopted in the analysis.

σ_y	$DF - \mathbf{d}\boldsymbol{\alpha}$	$DF - \mathbf{d}\boldsymbol{\alpha\varepsilon}$	$MF - \mathbf{d}\boldsymbol{\beta\varepsilon}$	$MF - \mathbf{d}\boldsymbol{\gamma}$
24	630	282	795	241
$\to \infty$	433	134	134	134

Table 4.9: Semi-cylinder: total global iterations for the different schemes varying the yield stress.

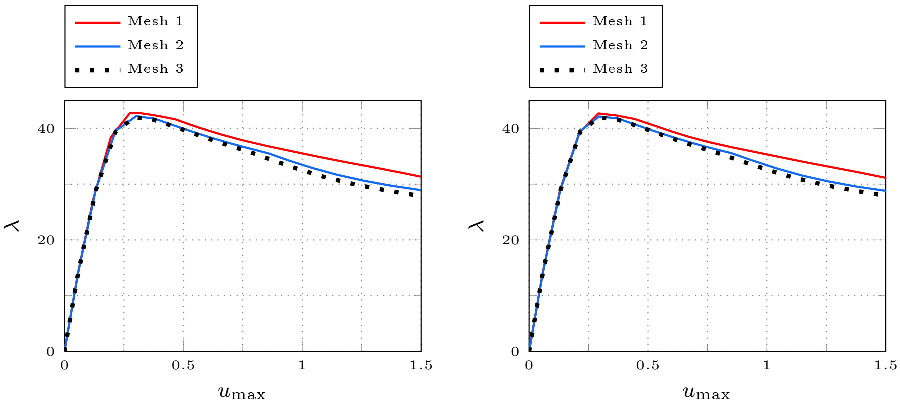

Displacement-based element with EAS

Mixed element

Figure 4.14: U-shape cantilever beam: convergence of the equilibrium path in terms of load factor and maximum displacement component for $\sigma_y = 2500$ varying the mesh for displacement-based elements with EAS and mixed elements.

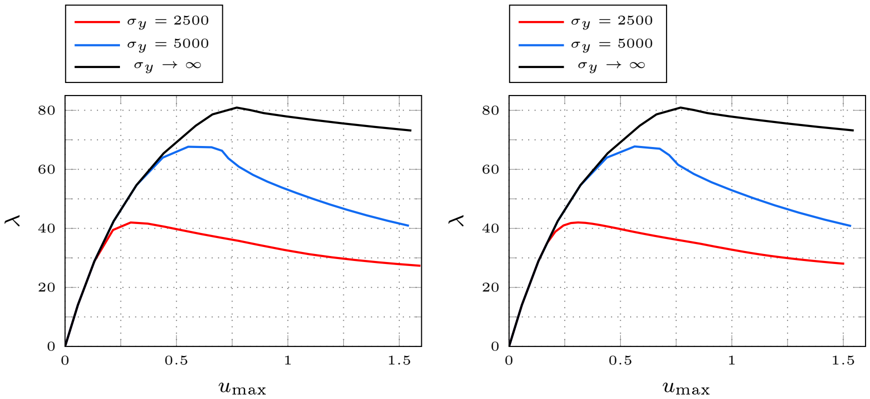

Displacement-based element with EAS

Mixed element

Figure 4.15: U-shape cantilever beam: equilibrium path in terms of load factor and maximum displacement component for $\sigma_y = 2500 - 5000$ and $\sigma_y \to \infty$ using the second mesh with both displacement-based elements with EAS and mixed elements.

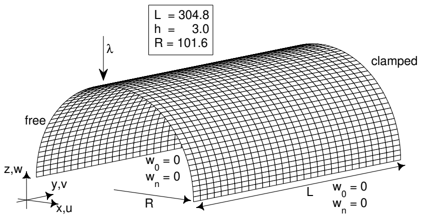

Figure 4.16: Semi-cylinder: model properties.

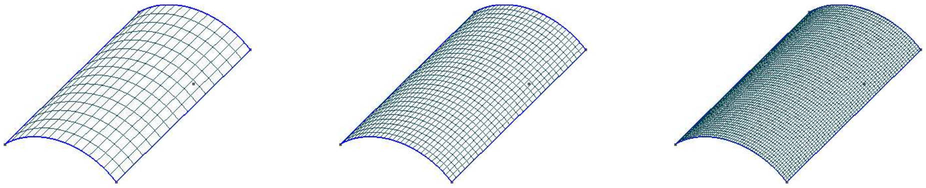

Mesh 1 Mesh 2 Mesh 3

Figure 4.17: Semi-cylinder: meshes for half of the structure adopted in the analysis.

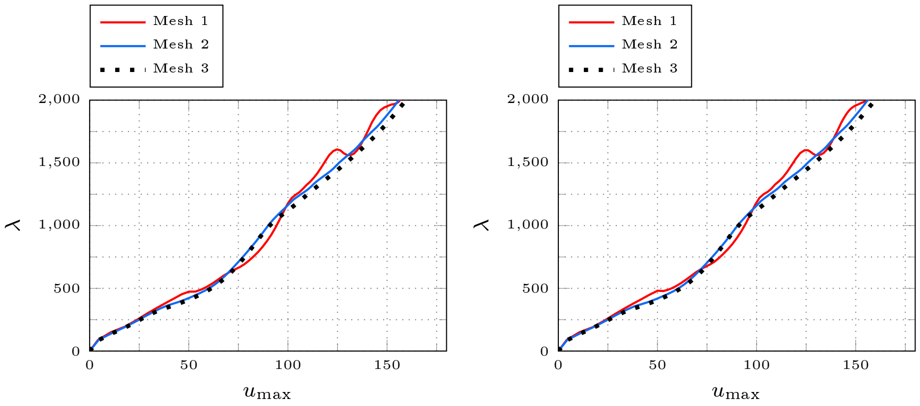

Displacement-based element with EAS Mixed element

Figure 4.18: Semi-cylinder: convergence of the equilibrium path in terms of load factor and maximum displacement component for $\sigma_y = 24$ varying the mesh for displacement-based elements with EAS and mixed elements.

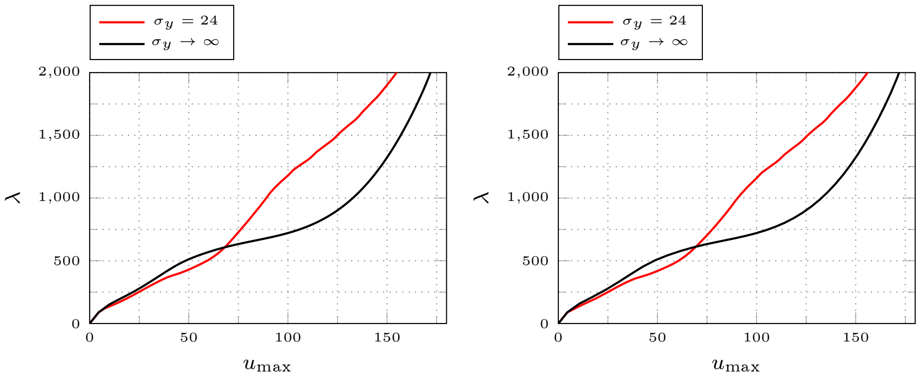

Displacement-based element with EAS Mixed element

Figure 4.19: Semi-cylinder: equilibrium path in terms of load factor and maximum displacement component for $\sigma_y = 24$ and $\sigma_y \to \infty$ using the second mesh with both displacement-based elements with EAS and mixed elements.

4.7 Summary

At each step of a path-following structural analysis, the iterative solution is usually carried out at two different levels. The constitutive law is imposed locally at the integration point or finite element level in order to compute the internal forces. Then, the equilibrium equations are solved at the global level after assembling the finite element contributions. This strategy is well established but it is affected by an increase of the iterative burden in case of large rotations and high membrane/flexural stiffness ratios. This issue was solved in the past for linear elastic materials using mixed finite elements or mixed integration points with the stress considered as an independent variable of the iterative process as well as the displacement. In this Chapter, different approaches were investigated for the path-following finite element analysis of beams and shells in case of geometric and material non-linearities, in order to identify the most efficient strategy in terms of iterative solution of the discrete equations. The numerical investigation shows that for beam/frame structures, the most efficient solution is achieved by mixed (stress-displacement) finite elements, assuming the discrete stress DOFs of the element and the strain at the integration points as independent variables. The element state is not determined at each global iteration but the element equations are solved together with the global equilibrium equations. This approach allows to avoid the iterative issue for large rotations and high stiffness ratios and to reduce the local computational burden. Moreover, when the non-linearity is mainly determined by the material, the mixed elements allow coarser meshes for beams than those necessary in the displacement-based approach, even if they are equivalent for linear elastic materials. On the other hand, the advantage of the mixed formulation in terms of required number of elements is lost in general shell structures, where the displacement-based finite elements improved by the EAS technique provide a similar accuracy and permit a faster evaluation of the element internal forces compared to mixed elements. Concerning the iterative scheme for shells, an efficient and robust option for displacement-based finite elements with EAS is achieved by solving the displacement-strain compatibility together with the global equilibrium equations with the strain at the integration points as independent variables in addition to displacements and EAS parameters. For mixed shell elements, the new scheme in displacements and element strain work-conjugate to the stress DOFs seems the most robust choice for large deformations and non-linear materials.

Conclusions

This thesis discussed different aspects concerning the modeling of shell structures and the numerical procedures for the path-following analysis of geometrical and material non-linearities.
After a brief introduction regarding the path-following solution of the structural problem in Chapter one, a mixed finite element, named MISS-4, for the shell structures undergoing material non-linearities was proposed in the second Chapter. The assumed stresses a-priori satisfy the equilibrium equations and a solid-like behavior was obtained using a layer-wise approach. Assuming reinforced concrete as testing material, a confinement-sensitive plasticity-based yield surface expressed in terms of Cauchy stresses was used to model the concrete behavior, while a uni-axial elastic perfectly plastic behavior was adopted for the reinforcement bars. The comparison with other available FEs proves the capacity of the proposed approach to represent the static non-linear equilibrium path, showing low error on coarse meshes and a quadratic rate of convergence.
In Chapter three, a large deformation isogeometric Kirchhoff-Love model hierarchically enhanced with warping profiles was presented. Particular focus was given to the modeling of alternating stiff/soft stacking sequences, which represent a peculiar example of warping through-the-thickness deformation: transverse shear strains tend to concentrate in the soft interlayers while the stiff layers can be assumed as Kirchhoff-Love shells (with the same rotation of the normal for each stiff layer). Being arbitrary the choice of the warping functions, two models were studied: 1) independent transverse shear deformations of the soft layers and 2) single zigzag, fixing the ratio between the shear sliding of the soft layers. The first warping model proved to be reliable and accurate for any setting of the stacking sequences, compared to the 3D solution assumed as the reference one, but its drawback is that the number of DOFs increases with the number of soft layers. The second warping model has the advantage of a fixed number of unknowns (five) regardless the numbers of layers, but it provides good results only for uniform distribution of the soft layers in terms of thickness and material. This brought also to the conclusion that, when the soft layers differ in mechanical and/or geometrical characteristics, a single zig-zag function is not capable of capturing the complex warping phenomena, which have proven to be also influenced by other characteristics of the structural element.
In Chapter four, different approaches were compared for the path-following finite element analysis of beams and shells in case of geometric and material non-linearities, with the aim to identify the most efficient strategy in terms of iterative solution of the discrete equations. The use of mixed (stress-displacement) finite elements, within a scheme where the element equations are solved together with the global equilibrium equations, has shown to be the best approach for beam/frame structures. The discrete stress DOFs of the element and the strain at the integration points are assumed as independent variables. The use of mixed FE has the double benefit of avoiding the iterative issue for large rotations and high stiffness ratios and of allowing the use of coarser meshes when the non-linearity is mainly determined by the material. This second advantage is generally lost in shell structures, where the displacement-based finite elements improved by the EAS technique provide a similar accuracy and permit a faster evaluation of the element internal forces compared to mixed elements. For this kind of element, a good iterative scheme is obtained by solving the displacement-strain compatibility together with the global equilibrium equations with the strain at the integration points as independent variables in addition to displacements and EAS parameters. Instead, the

new scheme in displacements and element strain work-conjugate to the stress DOFs seems the most robust choice for large deformations and non-linear materials in the case of mixed shell elements.

Bibliography

[1] C. Adam, T.J.R. Hughes, S. Bouabdallah, M. Zarroug, and H. Maitournam. Selective and reduced numerical integrations for NURBS-based isogeometric analysis. *Computer Methods in Applied Mechanics and Engineering*, 284:732–761, 2015.

[2] M.D. Alaydin, M. Behzadinasab, and Y. Bazilevs. Isogeometric analysis of multilayer composite shell structures: Plasticity, damage, delamination and impact modeling. *International Journal of Solids and Structures*, 252:111782, 2022.

[3] S. S. Antman. *The Theory of Rods*, pages 641–703. Springer Berlin Heidelberg, Berlin, Heidelberg, 1973.

[4] F. Auricchio, L. B. da Veiga, F. Brezzi, and C. Lovadina. Mixed finite element methods. *Encyclopedia of Computational Mechanics Second Edition*, pages 1–53, 2017.

[5] E. J. Barbero, A. Madeo, G. Zagari, R. Zinno, and G. Zucco. Imperfection sensitivity analysis of laminated folded plates. *Thin-Walled Structures*, 90:128 – 139, 2015.

[6] K.J. Bathe. *Finite Element Procedures.* Prentice Hall, 2006.

[7] Z.P. Bazant and J. Planas. *Fracture and Size Effect in Concrete and Other Quasibrittle Materials.* New Directions in Civil Engineering. Taylor & Francis, 1997.

[8] Y. Bazilevs, M. S. Pigazzini, A. Ellison, and H. Kim. A new multi-layer approach for progressive damage simulation in composite laminates based on isogeometric analysis and Kirchhoff-Love shells. Part I: basic theory and modeling of delamination and transverse shear. *Computational Mechanics*, 62:563–585, 2018.

[9] P. Betsch and A. Janz. An energy-momentum consistent method for transient simulations with mixed finite elements developed in the framework of geometrically exact shells. *International Journal for Numerical Methods in Engineering*, 108(5):423–455, 2016.

[10] A. Bilotta and R. Casciaro. A high-performance element for the analysis of 2d elastoplastic continua. *Computer Methods in Applied Mechanics and Engineering*, 196(4):818–828, 2007.

[11] A. Bilotta and G. Garcea. A two-level computational approach for the elasto-plastic analysis of framed structures with composite cross-sections. *Composite Structures*, 209:192–205, 2019.

[12] M. Bischoff and E. Ramm. Shear deformable shell elements for large strains and rotations. *International Journal for Numerical Methods in Engineering*, 40(23):4427–4449, 1997.

[13] J. Bleyer and P. De Buhan. A numerical approach to the yield strength of shell structures. *European Journal of Mechanics - A/Solids*, 59:178–194, 2016.

[14] B. Brank, D. Peric, and F. B. Damjanic. On large deformations of thin elasto-plastic shells: Implementation of a finite rotation model for quadrilateral shell element. *International Journal for Numerical Methods in Engineering*, 40(4):689–726, 1997.

[15] E. Carrera. Historical review of Zig-Zag theories for multilayered plates and shells. *Applied Mechanics Reviews*, 56(3):287–308, 05 2003.

[16] J.F. Caseiro, R.A.F. Valente, A. Reali, J. Kiendl, F. Auricchio, and R.J. Alves de Sousa. Assumed natural strain nurbs-based solid-shell element for the analysis of large deformation elasto-plastic thin-shell structures. *Computer Methods in Applied Mechanics and Engineering*, 284:861–880, 2015. Isogeometric Analysis Special Issue.

[17] G. Castellazzi and P. Krysl. Displacement-based finite elements with nodal integration for reissner-mindlin plates. *International Journal for Numerical Methods in Engineering*, 80(2):135–162, 2009.

[18] G. Castellazzi and P. Krysl. A nine-node displacement-based finite element for Reissner-Mindlin plates based on an improved formulation of the NIPE approach. *Finite Elements in Analysis and Design*, 58:31–43, 2012.

[19] S. Cen, X.-R. Fu, and M.-J. Zhou. 8- and 12-node plane hybrid stress-function elements immune to severely distorted mesh containing elements with concave shapes. *Computer Methods in Applied Mechanics and Engineering*, 200(29-32):2321–2336, 2011.

[20] S. Cen, Y. Shang, C.-F. Li, and H.-G. Li. Hybrid displacement function element method: A simple hybrid-trefftz stress element method for analysis of mindlin-reissner plate. *International Journal for Numerical Methods in Engineering*, 98(3):203–234, 2014.

[21] Y.B. Cho and R.C. Averill. First-order zig-zag sublaminate plate theory and finite element model for laminated composite and sandwich panels. *Composite Structures*, 50(1):1–15, 2000.

[22] R. Courant. Variational methods for the solution of problems of equilibrium and vibrations. 1943.

[23] S. de Miranda and F. Ubertini. A simple hybrid stress element for shear deformable plates. *International Journal for Numerical Methods in Engineering*, 65(6):808–833, 2006.

[24] L. Demasi. Refined multilayered plate elements based on murakami zig-zag functions. *Composite Structures*, 70(3):308–316, 2005.

[25] Pedro B. Dinis and Dinar Camotim. Post-buckling behaviour and strength of cold-formed steel lipped channel columns experiencing distortional/global interaction. *Computers and Structures*, 89(3):422–434, 2011.

[26] M. Duan. An efficient hybrid/mixed element for geometrically nonlinear analysis of plate and shell structures. *Computational Mechanics*, 35(1):72–84, 2004.

[27] A. Eijo, E. Onate, and S. Oller. A four-noded quadrilateral element for composite laminated plates/shells using the refined zigzag theory. *International Journal for Numerical Methods in Engineering*, 95(8):631–660, 2013.

[28] C. Escudero, S. Oller, X. Martinez, and A.H. Barbat. A laminated structural finite element for the behavior of large non-linear reinforced concrete structures. *Finite Elements in Analysis and Design*, 119:78–94, 2016.

[29] P Fajfar. A nonlinear analysis method for performance-based seismic design. *Earthquake Spectra*, 16(3):573–592, 2000.

[30] C.A. Felippa and B. Haugen. A unified formulation of small-strain corotational finite elements: I. theory. *Computer Methods in Applied Mechanics and Engineering*, 194(21):2285–2335, 2005.

[31] A.J.M. Ferreira, G.E. Fasshauer, R.C. Batra, and J.D. Rodrigues. Static deformations and vibration analysis of composite and sandwich plates using a layerwise theory and rbf-ps discretizations with optimal shape parameter. *Composite Structures*, 86(4):328–343, 2008.

[32] F. G. Flores. Implementation of the refined zigzag theory in shell elements with large displacements and rotations. *Composite Structures*, 118:560–570, 2014.

[33] L. Friedrich, S. Loosen, K. Liang, M. Ruess, C. Bisagni, and K.-U. Schräder. Stacking sequence influence on imperfection sensitivity of cylindrical composite shells under axial compression. *Composite Structures*, 134:750–761, 2015.

[34] L. Galuppi and G. Royer-Carfagni. Shear coupling effects of the core in curved sandwich beams. *Composites Part B: Engineering*, 76:320–331, 2015.

[35] G. Garcea, A. Madeo, and R. Casciaro. The implicit corotational method and its use in the derivation of nonlinear structural models for beams and plates. *Journal of Mechanics of Materials and Structures*, 7(6):509–538, 2012.

[36] G. Garcea, G. A. Trunfio, and R. Casciaro. Path-following analysis of thin-walled structures and comparison with asymptotic post-critical solutions. *International Journal for Numerical Methods in Engineering*, 55(1):73–100, 2002.

[37] G Garcea, GA Trunfio, and R Casciaro. Mixed formulation and locking in path-following nonlinear analysis. *Computer Methods in Applied Mechanics and Engineering*, 165(1-4):247–272, NOV 2 1998.

[38] A. Garg, H.D. Chalak, M-O. Belarbi, A.M. Zenkour, and R. Sahoo. Estimation of carbon nanotubes and their applications as reinforcing composite materials-an engineering review. *Composite Structures*, 272:114234, 2021.

[39] A.S. Genikomsou and M.A. Polak. 3d finite element investigation of the compressive membrane action effect in reinforced concrete flat slabs. *Engineering Structures*, 136:233–244, 2017.

[40] A. Genoese, A. Genoese, and G. Salerno. Elastic constants of achiral single-wall cnts: Analytical expressions and a focus on size and small scale effects. *Composites Part B: Engineering*, 147:207–226, 2018.

[41] M. Gherlone, A. Tessler, and M. Di Sciuva. C0 beam elements based on the refined zigzag theory for multilayered composite and sandwich laminates. *Composite Structures*, 93(11):2882–2894, 2011.

[42] L. A. Godoy. *Thin Walled Structures with Structural Imperfections: Analysis and Behavior*. Pergamon Press, Oxford, U.K., 1996.

[43] F. Gruttmann and W. Wagner. An advanced shell model for the analysis of geometrical and material nonlinear shells. *Computational Mechanics*, 66(6):1353–1376, 2020.

[44] Y. Guo and M. Ruess. A layerwise isogeometric approach for nurbs-derived laminate composite shells. *Composite Structures*, 124:300–309, 2015.

[45] Hai-Chao Han. A biomechanical model of artery buckling. *Journal of Biomechanics*, 40(16):3672–3678, 2007.

[46] A. Haydar and G. Royer-Carfagni. A Simple Model for Inflexed Multilayered Laminated Glass Beams Based on Refined Zig-Zag Theory. *Journal of Applied Mechanics*, 90(1), 10 2022. 011002.

[47] S. R. Henrichsen, P. M. Weaver, E. Lindgaard, and E. Lund. Post-buckling optimization of composite structures using koiter's method. *International Journal for Numerical Methods in Engineering*, pages n/a–n/a, 2016. nme.5239.

[48] A.J. Herrema, E.J. Johnson, D. Proserpio, M.C.H. Wu, J. Kiendl, and M.C. Hsu. Penalty coupling of non-matching isogeometric Kirchhoff-Love shell patches with application to composite wind turbine blades. *Computer Methods in Applied Mechanics and Engineering*, 346:810–840, 2019.

[49] A. Hrennikoff. Solution of Problems of Elasticity by the Framework Method. *Journal of Applied Mechanics*, 8(4):A169–A175, 1941.

[50] T.J.R. Hughes. *The Finite Element Method: Linear Static and Dynamic Finite Element Analysis.* Dover Civil and Mechanical Engineering. Dover Publications, 2012.

[51] T.J.R. Hughes, J.A. Cottrell, and Y. Bazilevs. Isogeometric analysis: CAD, finite elements, NURBS, exact geometry and mesh refinement. *Computer Methods in Applied Mechanics and Engineering*, 194(39):4135–4195, 2005.

[52] L. Iurlaro, M. Gherlone, M. Di Sciuva, and A. Tessler. Assessment of the refined zigzag theory for bending, vibration, and buckling of sandwich plates: a comparative study of different theories. *Composite Structures*, 106:777–792, 2013.

[53] I. V. Ivanov, D. S. Velchev, N. G. Georgiev, I. D. Ivanov, and T. Sadowski. A plate finite element for modelling of triplex laminated glass and comparison with other computational models. *Meccanica*, 51:341–358, 2016.

[54] Kjetil A. J. Optimal quadrature for univariate and tensor product splines. *Computer Methods in Applied Mechanics and Engineering*, 316:84 – 99, 2017. Special Issue on Isogeometric Analysis: Progress and Challenges.

[55] T.W. Jensen, P.N. Poulsen, and L.C. Hoang. Layer model for finite element limit analysis of concrete slabs with shear reinforcement. *Engineering Structures*, 195:51–61, 2019.

[56] H.-M. Jeon, Y. Lee, P.-S. Lee, and K.-J. Bathe. The mitc3+ shell element in geometric nonlinear analysis. *Computers and Structures*, 146:91–104, 2015.

[57] M. Jirasek and Z.P. Bazant. *Inelastic Analysis of Structures.* Wiley, 2001.

[58] S. Kaewunruen, C. Ngamkhanong, and T. Yang. Large-amplitude vibrations of spider web structures. *Applied Sciences*, 10(17), 2020.

[59] J. Kiendl, K.-U. Bletzinger, J. Linhard, and R. Wuchner. Isogeometric shell analysis with Kirchhoff-Love elements. *Computer Methods in Applied Mechanics and Engineering*, 198(49):3902–3914, 2009.

[60] M.D. Kotsovos. *Finite-Element Modelling of Structural Concrete: Short-Term Static and Dynamic Loading Conditions.* CRC Press, 2015.

[61] Wilfried B. Kratzig and Daniel Jun. Multi-layer multi-director concepts for D-adaptivity in shell theory. *Computers and Structures*, 80(9):719–734, 2002.

[62] A. Kraus, P. Wriggers, N. Viebahn, and J. Schröder. Low-order locking-free mixed finite element formulation with approximation of the minors of the deformation gradient. *International Journal for Numerical Methods in Engineering*, 120(8):1011–1026, 2019.

[63] P. Lenk and H. Lambert. Practical aspects of finite-element analysis in structural glass design. *Proceedings of the Institution of Civil Engineers - Structures and Buildings*, 168(7):527–538, 2015.

[64] L. Leonetti, F. S. Liguori, D. Magisano, and G. Garcea. An efficient isogeometric solid-shell formulation for geometrically nonlinear analysis of elastic shells. *Computer Methods in Applied Mechanics and Engineering*, 331:159–183, 2018.

[65] L. Leonetti, F. S. Liguori, D. Magisano, J Kiendl, A. Reali, and G. Garcea. A robust penalty coupling of non-matching isogeometric Kirchhoff-Love shell patches in large deformations. *Computer Methods in Applied Mechanics and Engineering*, 371:113289, 2020.

[66] L. Leonetti, F.S. Liguori, D. Magisano, and G. Garcea. An efficient isogeometric solid-shell formulation for geometrically nonlinear analysis of elastic shells. *Computer Methods in Applied Mechanics and Engineering*, 331:159 – 183, 2018.

[67] L. Leonetti, D. Magisano, A. Madeo, G. Garcea, J. Kiendl, and A. Reali. A simplified Kirchhoff-Love large deformation model for elastic shells and its effective isogeometric formulation. *Computer Methods in Applied Mechanics and Engineering*, 354:369 – 396, 2019.

[68] Q. Li, Y. Liu, Z. Zhang, and W. Zhong. A new reduced integration solid-shell element based on EAS and ANS with hourglass stabilization. *International Journal for Numerical Methods in Engineering*, pages 1885–1891, 2015.

[69] K. Liang, M. Ruess, and M. Abdalla. Co-rotational finite element formulation used in the koiter-newton method for nonlinear buckling analyses. *Finite Elements in Analysis and Design*, 2016.

[70] Y. Liang and B.A. Izzuddin. Nonlinear analysis of laminated shells with alternating stiff/soft lay-up. *Composite Structures*, 133:1220–1236, 2015.

[71] Y. Liang, F. Lancaster, and B.A. Izzuddin. Effective modelling of structural glass with laminated shell elements. *Composite Structures*, 156:47–62, 2016. 70th Anniversary of Professor J. N. Reddy.

[72] F. S. Liguori and A. Madeo. A corotational mixed flat shell finite element for the efficient geometrically nonlinear analysis of laminated composite structures. *International Journal for Numerical Methods in Engineering*, 122(17):4575–4608, 2021.

[73] Francesco S. Liguori, Giovanni Zucco, Antonio Madeo, Domenico Magisano, Leonardo Leonetti, Giovanni Garcea, and Paul M. Weaver. Postbuckling optimisation of a variable angle tow composite wingbox using a multi-modal koiter approach. *Thin-Walled Structures*, 138:183–198, 2019.

[74] E. Lindgaard and E. Lund. Nonlinear buckling optimization of composite structures. *Computer Methods in Applied Mechanics and Engineering*, 199(37-40):2319–2330, 2010.

[75] J. Lubliner, J. Oliver, S. Oller, and E. Oñate. A plastic-damage model for concrete. *International Journal of Solids and Structures*, 25(3):299–326, 1989.

[76] A. Madeo, F. S. Liguori, G. Zucco, and S. Fiore. An efficient isostatic mixed shell element for coarse mesh solution. *International Journal for Numerical Methods in Engineering*, 122(1):82–121, 2021.

[77] A. Madeo, G. Zagari, and R. Casciaro. An isostatic quadrilateral membrane finite element with drilling rotations and no spurious modes. *Finite Elements in Analysis and Design*, 50:21–32, 2012.

[78] A. Madeo, G. Zagari, R. Casciaro, and S. De Miranda. A mixed 4-node 3d plate element based on self-equilibrated isostatic stresses. *International Journal of Structural Stability and Dynamics*, 15(4), 2015.

[79] D. Magisano and A. Corrado. New robust and efficient global iterations for large deformation finite element analysis of beams and shells with material nonlinearity. *Computer Methods in Applied Mechanics and Engineering*, 406:115900, 2023.

[80] D. Magisano and G. Garcea. Fiber-based shakedown analysis of three-dimensional frames under multiple load combinations: Mixed finite elements and incremental-iterative solution. *International Journal for Numerical Methods in Engineering*, 121(17):3743–3767, 2020.

[81] D. Magisano and G. Garcea. Sensitivity analysis to geometrical imperfections in shell buckling via a mixed generalized path-following method. *Thin-Walled Structures*, 170:108643, 2022.

[82] D. Magisano, L. Leonetti, and G. Garcea. Advantages of the mixed format in geometrically nonlinear analysis of beams and shells using solid finite elements. *International Journal for Numerical Methods in Engineering*, pages n/a–n/a, 2016. nme.5322.

[83] D. Magisano, L. Leonetti, and G Garcea. How to improve efficiency and robustness of the Newton method in geometrically non-linear structural problem discretized via displacement-based finite elements. *Computer Methods in Applied Mechanics and Engineering*, 313:986–1005, 2017.

[84] D. Magisano, L. Leonetti, and G. Garcea. Unconditional stability in large deformation dynamic analysis of elastic structures with arbitrary nonlinear strain measure and multi-body coupling. *Computer Methods in Applied Mechanics and Engineering*, 393:114776, 2022.

[85] D. Magisano, L. Leonetti, A. Madeo, and G. Garcea. A large rotation finite element analysis of 3D beams by incremental rotation vector and exact strain measure with all the desirable features. *Computer Methods in Applied Mechanics and Engineering*, 361:112811, 2020.

[86] D. Magisano, K. Liang, G. Garcea, L. Leonetti, and M. Ruess. An efficient mixed variational reduced-order model formulation for nonlinear analyses of elastic shells. *International Journal for Numerical Methods in Engineering*, 113(4):634–655, 2018.

[87] D. Magisano, F.S. Liguori, L. Leonetti, D. De Gregorio, G. Zuccaro, and G. Garcea. A quasi-static nonlinear analysis for assessing the fire resistance of reinforced concrete 3d frames exploiting time-dependent yield surfaces. *Computers & Structures*, 212:327–342, 2019.

[88] D. Magisano, F.S. Liguori, L. Leonetti, and G. Garcea. Minkowski plasticity in 3d frames: Decoupled construction of the cross-section yield surface and efficient stress update strategy. *International Journal for Numerical Methods in Engineering*, 116(7):435–464, 2018.

[89] G. Maier. Quadratic programming and theory of elastic-perfectly plastic structures. *Meccanica*, 3(4):265–273, Dec 1968.

[90] G. Maier. Shakedown theory in perfect elastoplasticity with associated and nonassociated flow-laws: A finite element, linear programming approach. *Meccanica*, 4(3):250–260, Sep 1969.

[91] A. Makrodimopoulos. A class of strain-displacement elements in upper bound limit analysis. *International Journal for Numerical Methods in Engineering*, n/a(n/a), 2022.

[92] E. Marino. Locking-free isogeometric collocation formulation for three-dimensional geometrically exact shear-deformable beams with arbitrary initial curvature. *Computer Methods in Applied Mechanics and Engineering*, 324:546–572, 2017.

[93] F. Maurin, F. Greco, S. Dedoncker, and W. Desmet. Isogeometric analysis for nonlinear planar Kirchhoff rods: Weighted residual formulation and collocation of the strong form. *Computer Methods in Applied Mechanics and Engineering*, 340:1023–1043, 2018.

[94] G. Meschke, B. Pichler, and J. G. Rots, editors. *Computational modelling of concrete structures.* CRC Press, proceedings of the conference on computational modelling of concrete and concrete structures (euro-c 2018), 26 february – 1 march 2018, bad hofgastein, austria edition, 2018.

[95] T. Michiels and S. Adriaenssens. Identification of key design parameters for earthquake resistance of reinforced concrete shell structures. *Engineering Structures*, 153:411–420, 2017.

[96] Alessandro Nitti, Josef Kiendl, Alessio Gizzi, Alessandro Reali, and Marco D. de Tullio. A curvilinear isogeometric framework for the electromechanical activation of thin muscular tissues. *Computer Methods in Applied Mechanics and Engineering*, 382:113877, 2021.

[97] N. A. Nodargi and P. Bisegna. A novel high-performance mixed membrane finite element for the analysis of inelastic structures. *Computers and Structures*, 182:337–353, 2017.

[98] N. A. Nodargi and P. Bisegna. A mixed finite element for the nonlinear analysis of in-plane loaded masonry walls. *International Journal for Numerical Methods in Engineering*, 120(11):1227–1248, 2019.

[99] N. A. Nodargi and P. Bisegna. A mixed finite element for the nonlinear analysis of in-plane loaded masonry walls. *International Journal for Numerical Methods in Engineering*, 120(11):1227–1248, 2019.

[100] N.A. Nodargi. An overview of mixed finite elements for the analysis of inelastic bidimensional structures. *Arch Computat Methods. Eng.*, 26:1117–1151, 2019.

[101] H. S. Norville, K. W. King, and J. L. Swofford. Behavior and strength of laminated glass. *Journal of Engineering Mechanics*, 124(1):46 – 53, 1998.

[102] B. Oesterle, R. Sachse, E. Ramm, and M. Bischoff. Hierarchic isogeometric large rotation shell elements including linearized transverse shear parametrization. *Computer Methods in Applied Mechanics and Engineering*, 321:383–405, 2017.

[103] V. K. Papanikolaou and A. J. Kappos. Confinement-sensitive plasticity constitutive model for concrete in triaxial compression. *International Journal of Solids and Structures*, 44:7021–7048, 2007.

[104] A. Patton, P. Antolin, J. Dufour, Kiendl J., and A. Reali. Accurate equilibrium-based interlaminar stress recovery for isogeometric laminated composite Kirchhoff plates. *Composite Structures*, 256:112976, 2021.

[105] F. Petrone, F. McKenna, T. Do, and D. McCallen. A versatile numerical model for the nonlinear analysis of squat-to-tall reinforced-concrete shear walls. *Engineering Structures*, 242:112406, 2021.

[106] R. Pfefferkorn, S. Bieber, B. Oesterle, M. Bischoff, and P. Betsch. Improving efficiency and robustness of enhanced assumed strain elements for nonlinear problems. *International Journal for Numerical Methods in Engineering*, 122(8):1911–1939, 2021.

[107] Robin Pfefferkorn and Peter Betsch. Hourglassing- and locking-free mesh distortion insensitive Petrov-Galerkin EAS element for large deformation solid mechanics. *International Journal for Numerical Methods in Engineering*, n/a(n/a).

[108] T. H. H. Pian and C. Wu. *Hybrid and Incompatible Finite Element Methods.* Chapman & All, CRC, New-York, 1969.

[109] M.S. Pigazzini, D. Kamensky, D.A.P. van Iersel, M.D. Alaydin, J.J.C. Remmers, and Y. Bazilevs. Gradient-enhanced damage modeling in Kirchhoff-Love shells: Application to isogeometric analysis of composite laminates. *Computer Methods in Applied Mechanics and Engineering*, 346:152–179, 2019.

[110] Peter M. Pinsky and Kyun O. Kim. A multi-director formulation for nonlinear elastic-viscoelastic layered shells. *Computers and Structures*, 24(6):901–913, 1986.

[111] B. Piscesa, M. M. Attard, and K. Ali Samani. 3d finite element modeling of circular reinforced concrete columns confined with frp using a plasticity based formulation. *Composite Structures*, 194:478–493, 2018.

[112] JN Reddy. On refined theories of composite laminates. *Meccanica*, 25:230–238, 1990.

[113] J.N. Reddy. *Mechanics of Laminated Composite Plates and Shells: Theory and Analysis (2nd ed.)*. CRC Press, 2003.

[114] E. Reissner. On one-dimensional finite-strain beam theory: The plane problem. *Zeitschrift für angewandte Mathematik und Physik ZAMP*, 23(5):795–804, 1972.

[115] E. Riks. An incremental approach to the solution of snapping and buckling problems. *International Journal of Solids and Structures*, 15(7):529–551, 1979.

[116] M. Robinson. A comparison of yield surfaces for thin shells. *International Journal of Mechanical Sciences*, 13(4):345–354, 1971.

[117] F. Rojas, J.C. Anderson, and L.M. Massone. A nonlinear quadrilateral layered membrane element with drilling degrees of freedom for the modeling of reinforced concrete walls. *Engineering Structures*, 124:521–538, 2016.

[118] M. L. Sanchez, P. M. Pimenta, and A. Ibrahimbegovic. A simple geometrically exact finite element for thin shells-Part 1: statics. *Computational Mechanics*, 2023.

[119] J. Schröder, N. Viebahn, D. Balzani, and P. Wriggers. A novel mixed finite element for finite anisotropic elasticity; the SKA-element Simplified Kinematics for Anisotropy. *Computer Methods in Applied Mechanics and Engineering*, 310:475–494, 2016.

[120] M. Schwarze and S. Reese. A reduced integration solid-shell finite element based on the eas and the ans concept-large deformation problems. *International Journal for Numerical Methods in Engineering*, 85(3):289–329, 2011.

[121] S. Sessa, F. Marmo, L. Rosati, L. Leonetti, G. Garcea, and R. Casciaro. Evaluation of the capacity surfaces of reinforced concrete sections: Eurocode versus a plasticity-based approach. *Meccanica*, 53(6):1493–1512, 2018.

[122] A. H. Shihab, A. Eliasy, B. T. Lopes, R. Wu, L. S. White, S. Jones, B Geraghty, A. Joda, A. Elsheikh, and A. Abass. Compressive behaviour of soft contact lenses and its effect on refractive power on the eye and handling off the eye. *PLoS ONE*, 16, 2021.

[123] J. C. Simo and M. S. Rifai. A class of mixed assumed strain methods and the method of incompatible modes. *International Journal for Numerical Methods in Engineering*, 29(8):1595–1638, 1990.

[124] J.C. Simo and D.D. Fox. On a stress resultant geometrically exact shell model. part i: Formulation and optimal parametrization. *Computer Methods in Applied Mechanics and Engineering*, 72(3):267–304, 1989.

[125] J.C. Simo and T.J.R. Hughes. *Computational Inelasticity*. Interdisciplinary Applied Mathematics. Springer New York, 2000.

[126] J.C. Simo, J.G. Kennedy, and R.L. Taylor. Complementary mixed finite element formulations for elastoplasticity. *Computer Methods in Applied Mechanics and Engineering*, 74(2):177–206, 1989.

[127] Dassault Systèmes Simulia. *ABAQUS 6.12/Analysis User's Manual. Volume IV: Elements.* Dassault Systèmes Simulia, USA, 2012.

[128] E. Spacone, F. C. Filippou, and F. F. Taucer. Fibre beam–column model for non–linear analysis of R/C frames: part I. Formulation. *Earthquake Engineering & Structural Dynamics*, 25(7):711–725, 1996.

[129] K. V. Spiliopoulos and G. Ch. Lykidis. An efficient three-dimensional solid finite element dynamic analysis of reinforced concrete structures. *Earthquake Engineering & Structural Dynamics*, 35(2):137–157, 2006.

[130] K.V. Spiliopoulos and T.N. Patsios. An efficient mathematical programming method for the elastoplastic analysis of frames. *Engineering Structures*, 32(5):1199–1214, 2010.

[131] K.Y. Sze, W.K. Chan, and T.H.H. Pian. An eight-node hybrid-stress solid-shell element for geometric non-linear analysis of elastic shells. *International Journal for Numerical Methods in Engineering*, 55(7):853–878, 2002.

[132] R. L. Taylor, F. C. Filippou, A. Saritas, and F. Auricchio. A mixed finite element method for beam and frame problems. *Computational Mechanics*, 31(1):192–203, May 2003.

[133] A. Tessler, M. Di Sciuva, and M. Gherlone. A refined zigzag beam theory for composite and sandwich beams. *Journal of Composite Materials*, 43(9):1051–1081, 2009.

[134] Chien H. Thai, A.J.M. Ferreira, E. Carrera, and H. Nguyen-Xuan. Isogeometric analysis of laminated composite and sandwich plates using a layerwise deformation theory. *Composite Structures*, 104:196–214, 2013.

[135] John H. Thomsen and John W. Wallace. Displacement-Based Design of Slender Reinforced Concrete Structural Walls. *Journal of Structural Engineering*, 130(4):618–630, 2004.

[136] Thanh Ngoc Tran, G. R. Liu, H. Nguyen-Xuan, and T. Nguyen-Thoi. An edge-based smoothed finite element method for primal-dual shakedown analysis of structures. *Int. J. Numer. Methods Eng.*, 82(7):917–938, MAY 14 2010.

[137] P.-A. Ubach and E. Onate. New rotation-free finite element shell triangle accurately using geometrical data. *Computer Methods in Applied Mechanics and Engineering*, 199(5-8):383–391, 2010.

[138] N. Valoroso, F. Marmo, and S. Sessa. Limit state analysis of reinforced shear walls. *Engineering Structures*, 61:127–139, 2014.

[139] L. Vu-Quoc and X. Tan. Efficient Hybrid-EAS solid element for accurate stress prediction in thick laminated beams, plates, and shells. *Computer Methods in Applied Mechanics and Engineering*, 253:337–355, 2013.

[140] L. Vu-Quoc and X. G. Tan. Optimal solid shells for non-linear analyses of multilayer composites. I Statics. *Computer Methods in Applied Mechanics and Engineering*, 192(9-10):975–1016, 2003.

[141] W. Wagner and F. Gruttmann. A robust non-linear mixed hybrid quadrilateral shell element. *International Journal for Numerical Methods in Engineering*, 64(5):635–666, 2005.

[142] Q. Xie, K.Y. Sze, and Y.X. Zhou. Drape simulation using solid-shell elements and adaptive mesh subdivision. *Finite Elements in Analysis and Design*, 106:85–102, 2015.

[143] G. Zucco, R.M.J. Groh, A. Madeo, and P.M. Weaver. Mixed shell element for static and buckling analysis of variable angle tow composite plates. *Composite Structures*, 152(Supplement C):324 – 338, 2016.